GEORG-AUGUST-UNIVERSITÄT
GÖTTINGEN

Fakultät für
Physik

Master's Thesis

Suche nach BSM H→ $\tau\tau$ im voll-hadronischen Zerfallskanal mit ATLAS

Search for BSM H→ $\tau\tau$ in the fully hadronic decay channel with ATLAS

prepared by

Lino Gerlach

from Kreuztal

at the II. Physikalischen Institut

Thesis number:	II.Physik-UniGö-MSc-2017/06
Thesis period:	5th October 2016 until 4th October 2017
First referee:	Prof. Dr. Stan Lai
Second referee:	Prof. Dr. Ariane Frey

Abstract

A search for heavy neutral Higgs bosons, A/H, as predicted by the MSSM is performed using a 36.1 fb^{-1} data set recorded at the ATLAS detector in 2015 and 2016 at a centre-of-mass energy of $\sqrt{s} = 13$ TeV. The particle is assumed to decay into a pair of τ leptons and the all-hadronic final state is considered for this search. The results are interpreted in different benchmark scenarios, such as the hMSSM. Special emphasis is put on the techniques used to estimate the background emerging from falsely identified jets to improve the already existing analysis. The signal acceptance as a function of the A/H mass is also investigated using Monte Carlo generated signals with assumed masses ranging from 200 GeV to 2.5 TeV. No excess over the Standard Model background was observed.

iv

Contents

1 Introduction

The Standard Model of particle physics (SM) is a quantum field theory describing the known fundamental constituents of nature and their interactions. It has been tested at many different experiments and so far, every measurement made is consistent with its predictions. There are, however, observations that cannot be understood in the context of the SM. Therefore, physics *beyond the Standard Model* (BSM) must exist.

Supersymmetry (SUSY) is one of the most promising extensions to the SM, possibly resolving major issues such as the hierarchy problem and predicting a promising constituent of Dark Matter. If SUSY occurs in nature, it would result in an extended Higgs sector with at least two Higgs doublets, implying the existence of additional heavy Higgs bosons besides the scalar particle with a mass of 125 GeV that was found at the LHC in 2012 [1][2]. So far, all results point to this particle being consistent with the SM Higgs boson. The coupling of heavy Higgs bosons to other particles would depend on the particles' mass, as in the case for the SM Higgs boson whose decay into a pair of τ leptons is its only observed coupling to leptons until today [3]. Furthermore, the mixing of different Higgs fields (parametrised by $\tan \beta$) could enhance the coupling to down-type fermions, which makes the decay channel with two τ leptons very promising.

In this thesis, data taken in 2015 and 2016 by the ATLAS detector at a centre-of-mass energy of $\sqrt{s} = 13$ TeV corresponding to an integrated luminosity of 36.1 fb^{-1} will be used for the search for heavy Higgs bosons decaying into a pair of hadronically decaying τ leptons. To do so, methods of an already existing analysis are revisited and improved. An observation of such a particle would be a direct indication of BSM physics.

An outline for the theoretical background follows. In Chapter 2, the SM is explained briefly. Afterwards, problems with the SM and how SUSY addresses these problems are elaborated upon in Chapter 3. In Chapter 4, the experimental apparatus, namely LHC and the ATLAS detector, are discussed (including Monte Carlo generators and detector simulation) before the focus is laid on the existing search for $H \to \tau\tau$ in Chapter 5.

Since a hadronically decaying τ lepton causes a signature in the detector that is similar to that of a jet initiated by a quark or a gluon, a significant amount of the background that passes the selection criteria of the analysis emerges from those jets being falsely identified

as a hadronically decaying τ lepton. Therefore, the background estimate makes use of dedicated methods to estimate the amount of fake τ leptons which are investigated and improved in the Chapters 6 and 7.

In Chapter 8, Monte Carlo generated events containing heavy Higgs bosons for different assumed scenarios are investigated to understand the efficiency and acceptance of the event slection criteria. A conclusion is drawn in Chapter 9.

2 The Standard Model

The Standard Model (SM) of particle physics describes a set of elementary particles that interact through three of the four known fundamental forces: the strong interaction, the weak interaction and the electromagnetic interaction [4] [5] [6].These particles and interactions are described using quantum fields, where all relevant information about a physical system is contained in the so-called *Lagrange density*, $\mathcal{L}$. Furthermore, the SM is a *local gauge theory*. This means that the system has mathematical degrees of freedom that do not correspond to any changes in the actual physical state. To be precise, the gauge group of the SM is $SU(3)_C \times SU(2)_L \times U(1)_Y$, where the indices denote the colour charge, the weak isospin, and the hypercharge, respectively. Each generator of the symmetry transformations corresponds to a spin-1 vector boson field (8 gluons from $SU(3)_C$ and $W^{1,2,3}$ and B^0 from $SU(2)_L \times U(1)_Y$). The latter four fields mix, creating mass eigenstates that are detected as particles. These are the photon γ, the $W^{\pm}$ bosons, and the Z^0 boson. In addition to these, the SM is comprised of three families of spin-1/2 chiral fields. Each of them contains an up-type quark, a down-type quark, a neutrino and a charged lepton. Quarks are the only fermions (spin-1/2 particles) that carry a colour charge, implying they take part in the strong interaction. Neutrinos carry no charge at all, which means they can only participate in the weak interaction. The Higgs boson is the only scalar (spin-0) particle predicted by the SM. The complete set of particles of the SM can be seen in Figure 2.1 (left). In Fig. 2.2, a summary of several SM production cross sections with the corresponding theoretical predictions is displayed. It shows how well expected and observed values agree over a large energy range.

2.1 Higgs mechanism

If the electroweak symmetry of the SM was unbroken, the gauge fields of the electroweak force, $W^{1,2,3}$ and B^0, would be in a one-to-one correspondence with massless particles. Since $m_{W^{\pm}} = 80.385 \pm 0.015$ GeV and $m_{Z^0} = 91.1876 \pm 0.0021$ GeV [8], we know that the electroweak symmetry must be broken. Introducing explicit mass terms to the Lagrange density would, however, spoil the local gauge invariance of the SM. This problem can be
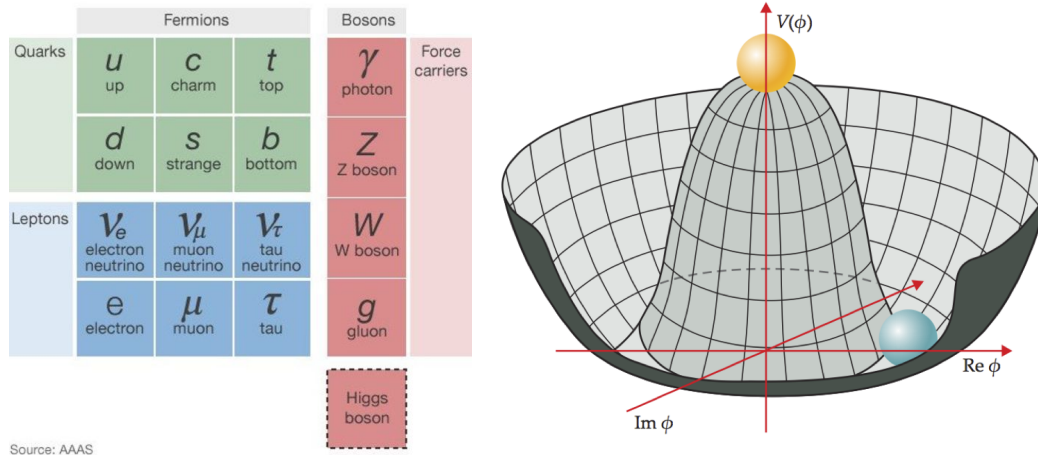
Figure 2.1: Particle content and Higgs potential of the Standard Model.
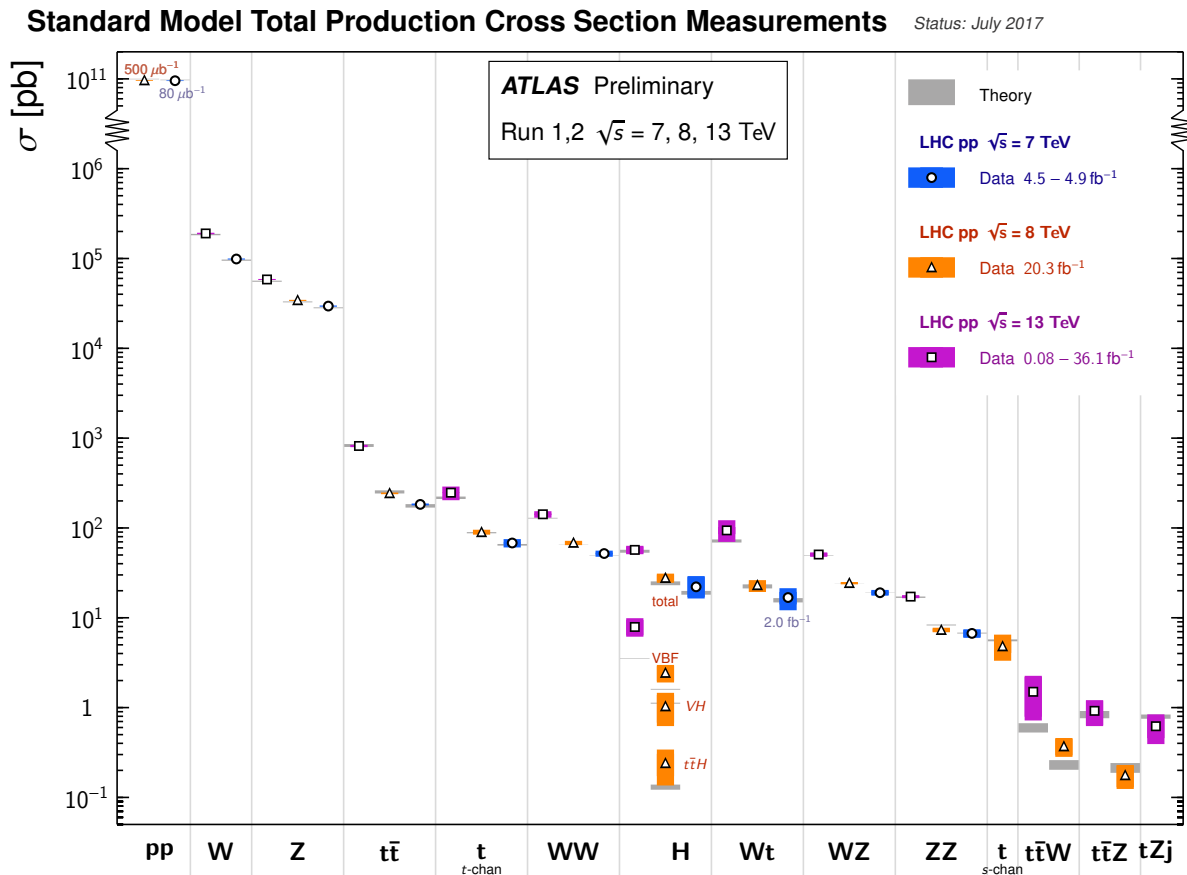
Figure 2.2: Summary of several Standard Model total production cross section measurements, corrected for leptonic branching fractions, compared to the corresponding theoretical expectations. All theoretical expectations were calculated at NLO or higher. The luminosity used for each measurement is indicated close to the data point [7].

solved by introducing a new complex scalar doublet field, ϕ, to $\mathcal{L}$. Its potential is then given by

$$V(\phi) = \mu^2 \phi^\dagger \phi + \lambda(\phi^\dagger \phi)^2, \qquad \mu^2 < 0, \ \lambda > 0. \tag{2.1}$$

Its shape is schematically displayed in Figure 2.1 (right). The global minimum, which corresponds to the ground state with the lowest energy, lies in a circle of diameter v around zero. v is known as the *vacuum expectation value* (vev). Since the Higgs field is rotationally symmetric around the zero but not around the vacuum expectation value, the symmetry is *spontaneously broken* or simply hidden at common energy scales. When expanding the field around the vacuum expectation value, new mass terms for W and Z bosons emerge in the Lagrange density, which is known as the Higgs mechanism [9].

The fermions also acquire their mass via coupling to the Higgs field (Yukawa coupling). Here, the coupling strength for vertices involving one Higgs boson and two fermions is proportional to the mass of the fermion.

In 2012, a scalar particle with a mass of $125.09 \pm 0.21(stat.) \pm 0.11(syst.)$ was found at the LHC [1][2]. It was identified as the Higgs boson predicted by Higgs mechanism and precision measurements continue to be carried out to fully determine its properties. Since the Higgs boson was the last undiscovered particle predicted by the SM, this was seen as the most important discovery in particle physics for the last years and awarded the Nobel Prize in 2013 [10].

2.2 τ leptons

Since τ leptons are the heaviest of all leptons in the SM with a mass of 1776.82 ± 0.16 MeV [8], they are expected to have the strongest coupling to the Higgs boson, which should also hold for a potential heavy Higgs boson. Furthermore, certain properties of a potential heavy Higgs could further enhance its coupling to down-type fermions like the τ lepton. Therefore, τ leptons are of special interest in searches for heavy Higgs bosons.

Since they are the only leptons that are heavier than the lightest quarks, they are also the only ones that can decay to hadrons. On average, it takes $(290.3 \pm 0.5) \times 10^{-15}$ s for a τ lepton to decay [8]. The possible decay modes and their corresponding branching ratios are listed in Table 2.1. For the hadronic decays, a distinction is made between decays with one or three charged particles ("prongs") in the final state. One-prong decays account for roughly three times as many hadronic τ decays as three-prong decays. In principle, a τ lepton can also decay to a final state with five charged particles such as $3\pi^- 2\pi^+ \nu_\tau$, but

τ^- Decay Mode	Branching Ratio [%]	Classification of Decay Channel
$e^- \bar{\nu}_\mu \nu_\tau$	17.82 ± 0.04	leptonic
$\mu^- \bar{\nu}_\mu \nu_\tau$	17.39 ± 0.04	
$h^- \nu_\tau \geq 0$ neutrals	49.03 ± 0.1	hadronic, one-prong
$h^- h^- h^+ \nu_\tau \geq 0$ neutrals	15.21 ± 0.06	hadronic, three-prong
Other decay modes	0.55 ± 0.13	

Table 2.1: τ decay modes and corresponding branching ratios. $h^\pm$ can be $\pi^\pm$ or $K^\pm$ mesons [8].

these occur in such low numbers that they will be neglected in the following. When a τ lepton decays hadronically, its decay products can be grouped together in a cone which can then be identified as a jet. Jets produced by these decays usually have a smaller radius than QCD jets and the leading particles within the cone have a disposition to carry a larger fraction of the momentum of the mother particle, which is graphically displayed in Fig. 2.3. Because of its short lifetime, a τ lepton produced at the bunch crossing will decay before reaching the innermost part of the detector. However, the trajectories of the final state particles will meet at a point displaced from the actual bunch crossing. This is called a secondary vertex. These mentioned properties of hadronic τ lepton decays can help distinguishing them from ordinary QCD jets.
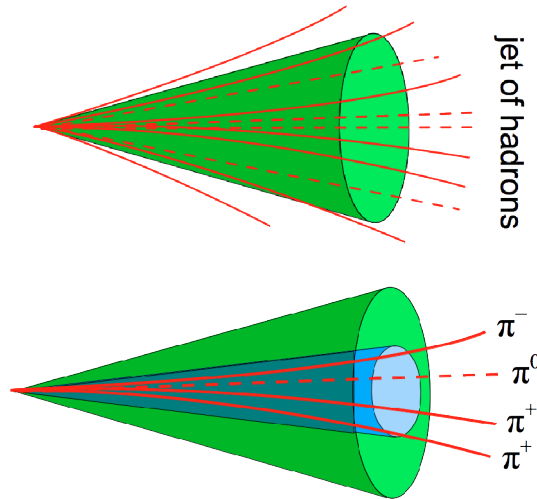

Figure 2.3: A jet from QCD processes (top) and a jet caused by a hadronically decaying τ lepton, which is narrower (bottom).

3 Problems with the Standard Model and Supersymmetry

The SM has been tested experimentally using many different measurements in different experiments, and no collider physics measurement result contradicts it. However, there are observations that are not understood in the context of the SM. Therefore, the need exists for physics *beyond the Standard Model* (BSM). A very promising BSM theory is *Supersymmetry* (SUSY). It predicts (so far) undiscovered supersymmetric partners for the particles of the SM.

3.1 Dark Matter

One of the things that cannot yet be explained within the SM is known as *Dark Matter*. When investigating rotational velocity of galaxies as a function of distance to the centre (galaxy rotation curves), one finds that the observed distribution is not compatible with predictions from general relativity [11].

Different scenarios concerning how the matter is distributed within the galaxy can be assumed to predict the corresponding galaxy rotation curve. However, none of these scenarios matches the observed behaviour. This lead to the proposal that stars, gas clouds, black holes and all other known objects are not the only contributors to the galaxy's mass. Thus, there must be some sort of object called Dark Matter that predominantly interacts gravitationally. From cosmological observations, one can estimate the fraction of energy in our universe that originates from ordinary matter from the SM to be most likely around 4% [12]. If R-parity is conserved (see Section 3.4), the lightest supersymmetric particle would be a good candidate to explain of what Dark Matter is made.

3.2 Quantum Gravity and the Planck Scale

A big problem of the SM is the incompatibility between gravity and quantum mechanics. This problem becomes prominent when investigating particles on a length scale that is

close to the particle's Schwarzschild radius, $r = \frac{2Gm}{c^2}$ [13]. To estimate where this scale lies, consider the Heisenberg uncertainty principle in the form

$$\Delta x \cdot \Delta p \geq \frac{\hbar}{2}. \tag{3.1}$$

Restricting the particle's position increases its momentum and with it the corresponding energy and mass. For a sufficiently small Δx, the particle's mass will be high enough to form a black hole. The value of Δx, where the local restriction of a particle is equal to its Schwarzschild radius is known as Planck length:

$$l_{Pl} := \sqrt{\frac{G\hbar}{c^3}} \approx 1.6 \cdot 10^{-35} \text{ m}. \tag{3.2}$$

The Planck energy, $E_{Pl} \approx 10^{19}$ GeV, is defined as the corresponding energy uncertainty. Simply put, the SM does not hold for processes at energies above 10^{19} GeV since a quantum mechanical treatment of gravity would be needed in that case.

3.3 Hierarchy Problem

Another issue into which the SM provides no insight is the so-called *hierarchy* problem. It refers to the fact that the value of the Higgs boson mass is not at a natural scale. During its calculation, fermionic loop corrections on the Higgs mass need to be taken into account up to the highest energy scale for which the theory holds (cut-off scale or ultraviolet limit), which, in the case of the SM, is the Planck Energy, E_{Pl} (see Section 3.2).

$$\int^{E_{Pl}} d^4 f(k, \text{external momenta}). \tag{3.3}$$

The observed mass of roughly 125 GeV can only be obtained by fine tuning the squared mass by a value Δm_H^2 which depends quadratically on the cut-off scale:

$$\Delta m_H^2 = \frac{\lambda_f^2}{16\pi^2} [-2E_{Pl}^2 + ...] \propto E_{Pl}^2 \approx 10^{38} \text{ GeV}^2. \tag{3.4}$$

This leads to fine tuning that is of a much larger order than the observed mass. Analogous phenomena often indicate a deeper physical meaning. Without antiparticles, for example, humongous fine tuning would also be necessary when calculating the mass of the electron as well.

In the case of the hierarchy problem, SUSY would lead to bosonic fields that contribute
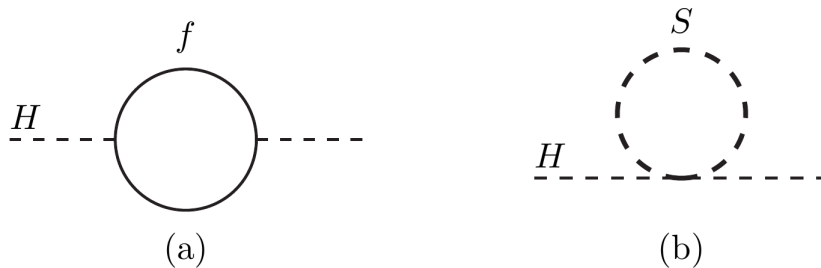
Figure 3.1: One-loop quantum corrections to the Higgs squared mass parameter m_H^2, due to (a) a Dirac fermion f , and (b) a scalar S [14].

to the loop corrections with the same absolute value but the opposite sign so that their effects cancel out and only minor fine tuning is needed (see Fig. 3.1). In this case, the theory already delivers a prediction on m_H and does not have to be fine-tuned to match the experimental observations.

3.4 Supersymmetry

Supersymmetry (SUSY) is a symmetry between bosonic and fermionic fields. Its generators, which will be denoted as Q and $Q^\dagger$ in the following, must therefore turn fermionic states into bosonic ones and vice versa:

$$Q|Boson> = |Fermion> \qquad Q|Fermion> = |Boson>.$$

Since they change the spin of particles by half-integer values, they must act as fermionic operators and anti-commute. The Haag-Łopuszański-Sohnius-Theorem [15] states that SUSY is the only nontrivial extension to the symmetry group of space-time translations, the Poincaré group. Other interesting implications of this theorem concern the SUSY generators themselves. They must act as spin-1/2 objects (e.g. spin-3/2 is ruled out) and fulfill the following schematic algebra [14]:

$$\{Q, Q^\dagger\} = P^\mu$$
$$\{Q, Q\} = \{Q^\dagger, Q^\dagger\} = 0$$
$$[P^\mu, Q] = [P^\mu, Q^\dagger] = 0.$$

Note that SUSY is not just one of many possibilities to combine an internal symmtery with the Poincaré group in a nontrivial way, but much more than that: it is the only possibility, which can be seen as further motivation for this model.

Names		spin 0	spin 1/2
squarks, quarks	Q	$(\widetilde{u}_L \quad \widetilde{d}_L)$	$(u_L \quad d_L)$
($\times 3$ families)	$\overline{u}$	$\widetilde{u}_R^*$	$u_R^\dagger$
	$\overline{d}$	$\widetilde{d}_R^*$	$d_R^\dagger$
sleptons, leptons	L	$(\widetilde{\nu} \quad \widetilde{e}_L)$	$(\nu \quad e_L)$
($\times 3$ families)	$\overline{e}$	$\widetilde{e}_R^*$	$e_R^\dagger$
Higgs, higgsinos	H_u	$(H_u^+ \quad H_u^0)$	$(\widetilde{H}_u^+ \quad \widetilde{H}_u^0)$
	H_d	$(H_d^0 \quad H_d^-)$	$(\widetilde{H}_d^0 \quad \widetilde{H}_d^-)$

Names	spin 1/2	spin 1
gluino, gluon	$\widetilde{g}$	g
winos, W bosons	$\widetilde{W}^\pm \quad \widetilde{W}^0$	$W^\pm \quad W^0$
bino, B boson	$\widetilde{B}^0$	B^0

Figure 3.2: Field content of the MSSM [14].

The irreducible representations of the SUSY algebra are called *supermultiplets*. Bosonic and fermionic fields that are related to each other by Q and $Q^\dagger$ are known as *superpartners*. Since Q and $Q^\dagger$ commute with any other generator of gauge transformation, they leave the corresponding quantum numbers untouched. Therefore, superpartners must have the same electric charge, weak isospin and color degrees of freedom. In particular, $[P^\mu, Q] = [P^\mu, Q^\dagger] = 0$ leads to $[P^2, Q] = [P^2, Q^\dagger] = 0$, which implicates that superpartners must have the same mass if SUSY was unbroken. One can show that for any supermultiplet, there must be an equal number of bosonic and fermionic degrees of freedom.

3.5 Minimal Supersymmetric Standard Model

In any supersymmetric extension of the SM, each fundamental particle is in either a chiral or a gauge supermultiplet and each fundamental particle must have a superpartner with spin differing by 1/2 unit. The *Minimal Supersymmteric Standard Model* (MSSM) is the supersymmetric theory which predicts the fewest additional particles to the SM. It assumes two Higgs doublets (the reason for this will be explained later) and one superpartner for each particle in the SM. The resulting field content can be seen in Fig. 3.2. Since the Higgs is a scalar boson (spin 0), it must reside in a chiral supermultiplet. One chiral supermultiplet would, however, lead to the electroweak gauge symmetry suffering

from a gauge anomaly. To prevent the anomaly from occuring, the so called *anomaly trace* must satisfy $\text{Tr}[T_3^2 Y] = \text{Tr}[Y^3] = 0$. This is fulfilled in the SM by the usual quarks and leptons. In the MSSM, however, one Higgs supermultiplet would spoil this condition. Furthermore, the super potential, whose derivatives occur in the Lagrange density, must be a holomorphic function of the included fields in any supersymmetric theory [1]. Therefore, terms like $H_u^* H_u$ or $H_d^* H_d$ analogous to the Higgs mass term in the Lagrange density of the SM are forbidden. Instead,

$$\mu H_u H_d \tag{3.5}$$

appears in the MSSM Lagrangian as a mass term. For the same reason, Yukawa coupling terms in the MSSM Lagrangian like $\bar{u} Q H_u$ cannot be replaced by something such as $\bar{u} Q H_d *$. Therefore, only a $Y = +1/2$ Higgs field (H_u) can Yukawa couple to up-type quarks, and only a $Y = -1/2$ Higgs field (H_d) can couple to down-type quarks and charged leptons. This is why there must be two Higgs supermultiplets in the MSSM.

3.5.1 SUSY Breaking and the MSSM Higgs Sector

If SUSY was unbroken, superpartners must have the same mass and sparticles would have been found already. Therefore, SUSY must be a broken symmetry, most likely spontaneously broken such as the electroweak symmetry. This means that $\mathcal{L}$ is invariant, but the vacuum state is not, hiding the symmetry at low energies. This symmetry breaking can be achieved by extending the theory by new particles and interactions at very high mass scales. However, there is no consensus on how this should be done exactly and a variety of different mechanisms were proposed (e.g. GMSB, MSUGRA [14]).
Like in the SM, the symmetry breaking leads to splitting and mixing between gauge and mass eigenstates. As mentioned above, the Higgs scalar fields consist of two complex $SU(2)_L$ doublets, which lead to eight real degrees of freedom. Electroweak symmetry breaking creates three Goldstone bosons $G^0, G^\pm$, which become the longitudinal modes of Z^0 and $W^\pm$. The remaining five Higgs mass eigenstates are:

- Two CP-even neutral scalars h^0, H^0

- One CP-odd neutral scalar A^0

- One charged scalar H^+ and its conjugate H^-.

---

[1] A function $f(z, z^*) : U \to \mathbb{C}$ is holomorphic if and only if it is differentiable and $\frac{\partial f}{\partial z^*} = 0$ holds.

3.5.2 R-parity

In the MSSM, the Lagrange density can be extended by additional gauge invariant terms. These will, however, violate either Baryon number (B) or Lepton number (L) conservation, which would lead to proton decay. Since this has not been experimentally observed yet, an additional mechanism is needed to explain this behaviour. In the SM, Lepton and Baryon number conservation is not introduced as a fundamental principle, but rather follows from the properties of the interactions. To keep the MSSM consistent with experiment, a new conserved quantum number, R-parity, is introduced according to

$$P_R = (-1)^{3(B-L)+2s}. \tag{3.6}$$

Particles of the SM will have $P_R = 1$, whereas their superpartners, the sparticles, will have $P_R = -1$. This does not only explain B and L conservation but also makes the lightest supersymmetric particle (LSP) stable, which is crucial when seeing it as a candidate for Dark Matter.

3.5.3 MSSM parameter space

The most general form of the MSSM has 120 additional free parameters compared to the SM. This makes it nearly impossible to exclude or verify the theory in general. However, many of these parameters could lead to effects such as flavour changing neutral currents or new sources of CP violation. Since none of these effects have ever been observed, many parameters of the MSSM can be fixed. Additional assumptions (such as assuming the lightest supersymmetric particle to be a neutralino) can narrow down the free parameter space, where only two non-SM parameters are left to describe the MSSM Higgs sector at tree level, which are chosen to be

- m_A, the mass of the CP-odd neutral scalar

- $\tan \beta = \frac{<H_u^0>}{<H_d^0>}$, the ratio of the two Higgs vacuum expectation values.

Beyond tree level, there are additional parameters that affect the Higgs sector. Depending on the choice of these, different MSSM benchmark scenarios are defined. Most of these scenarios identify the lighter of the two CP even neutral Higgs scalars, h^0, as the scalar particle with a mass of 125 GeV that was found at the LHC in 2012 [1][2]. However, this can be achieved in different ways. In the $m_h^{\max}$ scenario, for example, the benchmark parameters are chosen such that the mass of the of the light CP-even scalar, h^0, is maximised for fixed $\tan \beta$ and m_A to make it match the observed value [16]. Another
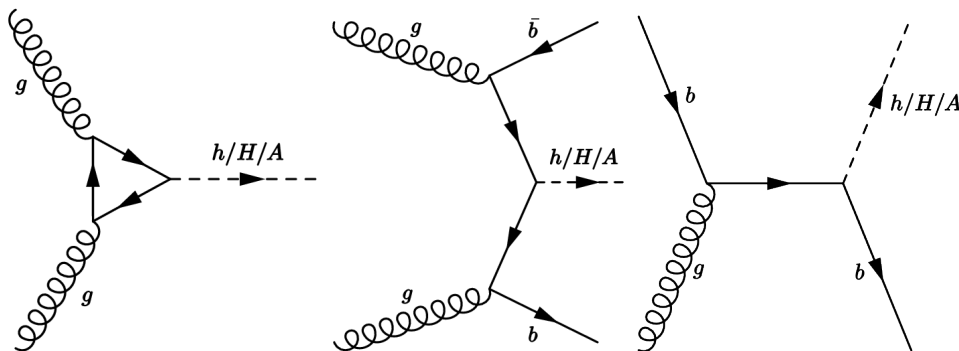
Figure 3.3: Strong Higgs production via gluon-gluon-fusion and *b*-associated production with and without and incoming *b*-quark (f.l.t.r.)[19].

approach is the $m_h^{\text{mod+}}$ scenario. Here, the mixing of the stop fields (the supersymmetric partners of the top quark fields) is chosen in a way to maximise the region in $\tan\beta$ that is compatible with the observed Higgs mass value [17]. The soft SUSY-breaking mass scale is usually chosen to be $M_{\text{SUSY}} = 1$ TeV in both of these scenarios.

Another approach is known as the hMSSM scenario, where the value of m_h is used to predict the other masses and coupling parameters without referencing the soft SUSY-breaking parameters [18].

In any case, for investigating the MSSM Higgs sector, the $m_A - \tan\beta$ plane is an appropriate parameter space to create exclusion limits in. Large values of $\tan\beta$ would also lead to an enhanced coupling of the neutral Higgs scalars, H^0 and A^0, to down-type fermions, resulting in increased branching fractions to τ leptons and b quarks. This has inspired many searches for a scalar boson in $\tau\tau$ and bb final states.

During the course of this thesis, exclusion limits in the $\tan\beta - m_A$ plane on the $m_h^{\text{mod+}}$ and hMSSM scenario will be presented.

3.5.4 Production of Heavy Higgs Bosons

In principle, H^0 and A^0 can be produced in a similar fashion like the SM Higgs particle, h^0. At the LHC, focus lays on the strong production since it has by far the highest cross section of all production processes. One can distinguish between gluon-gluon-fusion and b-associated production, where the Higgs particle is produced along with b quarks. Corresponding Feynman diagrams can be seen in Fig. 3.3.

As a measure for how probable an event is where a (heavy) Higgs particle is produced via one of the processes mentioned above and this particle then decays into two τ leptons, the product of cross section and branching ratio in dependence of the assumed mass the Higgs particle is investigated. Later, exclusion limits on this property will be shown.
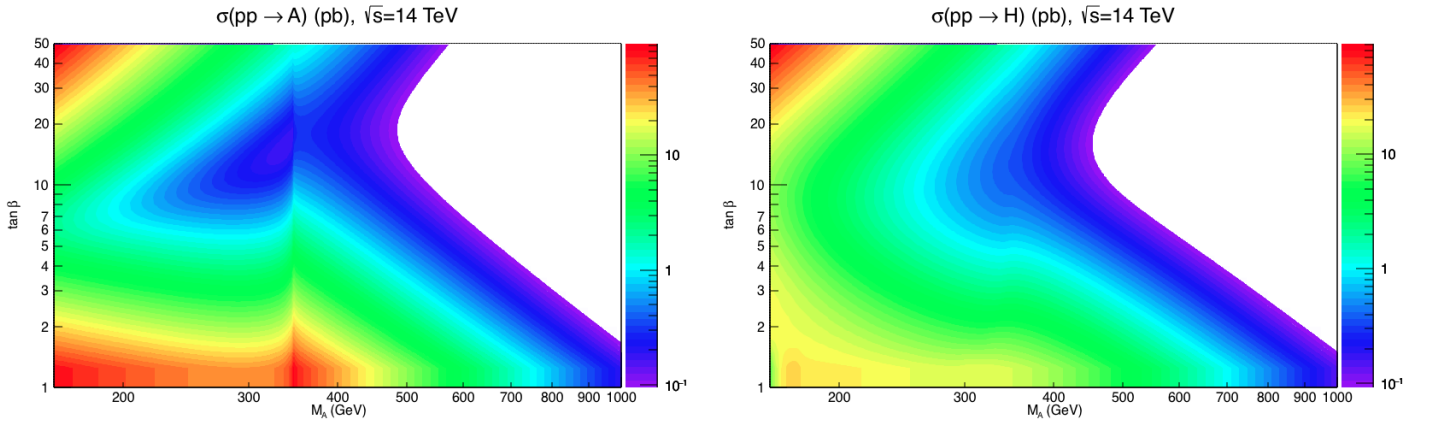
Figure 3.4: Production cross section of the heavy Higgs bosons A (left) and H (right) for proton-proton collisions at $\sqrt{s} = 14$ TeV in the $\tan\beta - m_A$ plane. Gluon-gluon-fusion and b-associated production have been considered [20].

In Fig. 3.4, the predicted production cross section for heavy Higgs bosons at the LHC is shown for the hMSSM scenario.

4 The LHC and the ATLAS Experiment

The *Large Hadron Collider* (LHC) is the biggest and most powerful particle collider in the world. It is located at CERN, the *European Organisation for Nuclear Research*, near Geneva, Switzerland. To protect it from cosmic radiation and other influences like vibrations, it lies in a 27 km long circular tunnel roughly 100 m underground. It was designed to collide protons at a centre of mass energy of $\sqrt{s} = 14$ TeV with a luminosity of about 10^{34} cm^{-2}s^{-1} [22]. The protons orbit in 2808 bunches consisting of up to 10^{11} particles, each. Bunch crossings occur every 25 ns. To force the particles on the circular trajectory of the LHC, superconducting magnets, cooled to a temperature of 1.9 K with the help of liquid Helium, create an 8.33 T strong magnetic field.

To produce the protons, Hydrogen is ionized at *LINAC II*. Before being injected into the actual LHC, they pass through several other accelerators. The last accelerator before the LHC main ring, the *Super Proton Synchrotron* (SPS), takes the particles to an energy of 450 GeV. In Fig. 4.1, the complete accelerator complex is schematically displayed.

There are various experiments located around the LHC. The four most important ones, ATLAS, CMS, LHCb, and ALICE, are each located at a crossing point, where bunches of protons propagating in opposite directions collide. ALICE was constructed to examine quark-gluon-plasma, which is a ferociously hot and dense state, similar to what existed shortly after the big bang. At LHCb, decays of hadrons containing bottom or charm quarks are observed to further investigate CP violation. Research at the heaviest detector, CMS, and the biggest detector, ATLAS, is focused on the properties of the Higgs boson, the top quark and theories beyond the SM, such as SUSY, among other things.

From 2010 to 2013, the LHC was run with a centre of mass energy of 7 to 8 TeV (Run 1, 28.26 fb^{-1}). Afterwards, in a two year break from collisions, hardware upgrades were being implemented to prepare the collider for higher energies and luminosities. In 2015, Run 2 started with a centre of mass energy of $\sqrt{s} = 13$ TeV. During both runs, the collider was able to constantly increase the luminosity, reaching the value it was originally designed for in 2016 and currently exceeding it by over 40 % [21], reaching a maximum instantaneous
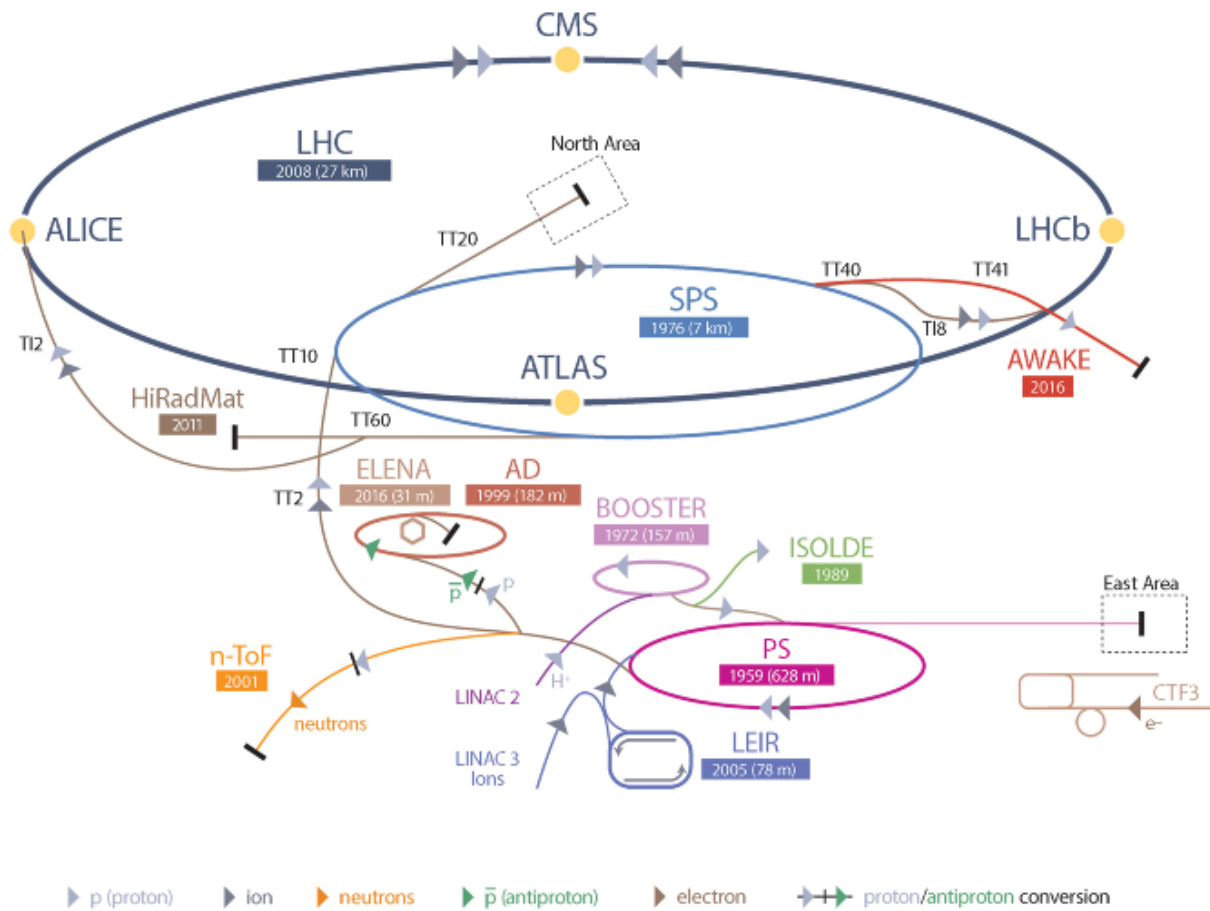
Figure 4.1: Schematic overview of the accelerator complex at CERN [21].

luminosity of $1.74 \cdot 10^{34}$ cm^{-2}s^{-1} [23]. In Fig. 4.2, the integrated luminosities of the LHC for five different years are displayed.

4.1 The ATLAS detector

The ATLAS detector (*A Toroidal LHC ApparatuS* [24]) is the biggest detector at the LHC and at CERN, in general. It is 25 m high and 44 m long, weighing approximately 7000 tonnes. Its layout is symmetric around the beam axis and consists of various layers of detectors. From inner to outer layer, these are: tracking detectors, calorimeters, and muon chambers. Between tracking detector and calorimeters, there is a thin, superconducting solenoid. More magnets are mounted azimuthally to the calorimeters. Together they
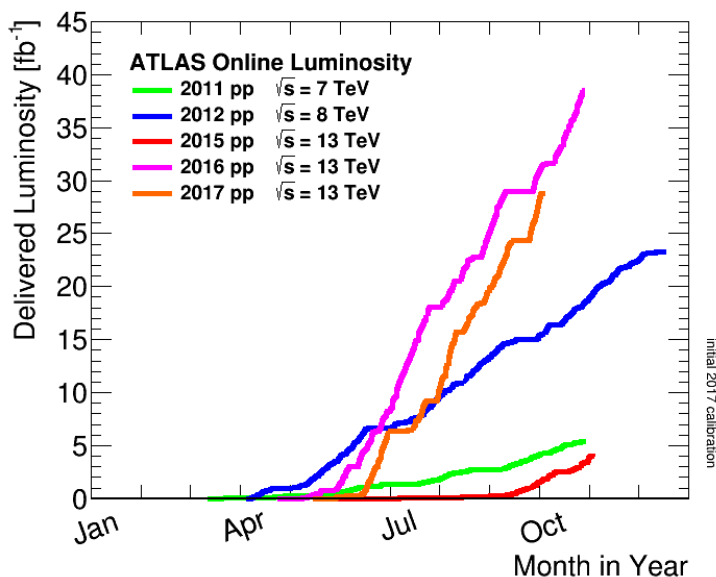
Figure 4.2: Integrated luminosity recorded by ATLAS for each year [23].

induce a 2 T magnetic field in the inner detector. In Fig. 4.4, the complete layout of the ATLAS detector is displayed schematically. Before describing the different sub detectors in more detail, some conventions regarding the coordinate system will be explained, as they are important throughout the rest of this thesis.

Because of its cylindrical structure, ATLAS uses a (right-handed) coordinate system where the beam direction defines the z-axis and the x-axis points towards the centre of the LHC. The angle ϕ lies in the plane perpendicular to the z- and x-axis. Variables such as the *transverse momentum*, p_T, or the *transverse energy*, E_T, refer to the projection onto this plane. The polar angle θ is measured from the beam-axis. Instead of θ, however, the rapidity $y \equiv \frac{1}{2} \ln \left(\frac{E - p_L}{E + p_L} \right)$ is often used, since intervals in y are invariant under Lorentz boosts along the z-axis. Here, p_L is the longitudinal momentum, so the projection of $\vec{p}$ on the z-axis. In the ultra-relativistic limit, y is equal to the pseudo-rapidity, defined as $\eta \equiv - \ln \left(\tan \frac{\theta}{2} \right)$. Angular distances are measured in units of $\Delta R \equiv \sqrt{(\Delta \eta)^2 + (\Delta \phi)^2}$. The coordinate system is schematically displayed in Fig. 4.3.

4.1.1 Inner Detector

The Inner (or Tracking) Detector contains tracking systems using three different techniques. It is surrounded by a 2 T magnetic field, allowing for a precise determination of the transverse momentum and a good separation of charges. Every tracking detector utilises the fact that charged particles ionize material, producing charge differences which
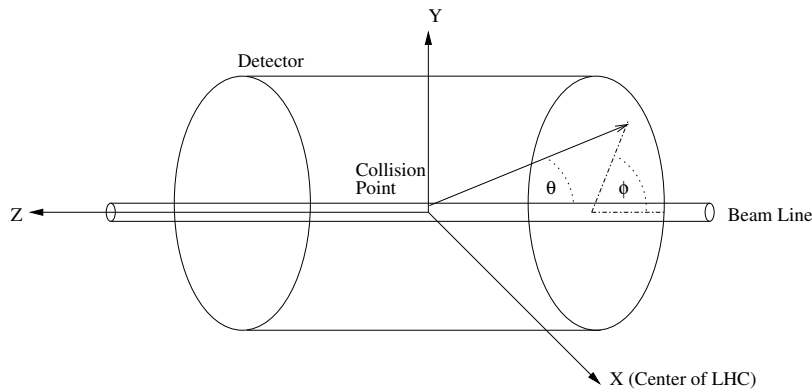
Figure 4.3: Coordinate system of the ATLAS detector [25].

are read out as a signal.

The *Silicon Pixel Detector* is closest to the interaction point ($R \geq 4.55$ cm). There are three layers in barrel and endcap discs, each, making up 80.3 million readout channels with a combined accuracy of 10×115 μm^2 ($R/\phi \times z$ for the barrel, $R/\phi \times R$ for the end-cap discs).

The *Silicon Microstrip Tracker* (SCT) surrounds the Silicon Pixel Detector. It uses silicon strips that are aligned in a way that each strip covers an angle of 40 mrad. With 6.3 million readout channels in barrel and end-cap, it reaches a resolution of 17×580 μm^2.

The outermost part of the Inner Detector is the *Transition Radiation Tracker* (TRT). Using straw tubes that cover the kinematic region with $|\eta| < 2.0$, it only delivers information on R/ϕ with roughly 351,000 readout channels, resulting in an accuracy of 130 μm per straw. Inside the straw, a mixture of $Xe/CO_2/O_2$ leads to transition radiation in the case that a charged particle passes through. The intensity of this transition radiation depends on the type of particle that caused it and its relativistic γ factor of the particle. Combined with the information on the transverse momentum from the other parts of the Inner Detector, this allows for a good mass resolution [26].

The combination of all three systems in the Inner Detector covers an area of $|\eta| < 2.5$ with a momentum resolution of $\sigma_{p_T}/p_T = 0.05\% \cdot p_T$ [GeV] $\oplus 1\%$ [24].

During a long shut down in 2016, a new innermost layer was added to the Silicon Pixel Detector, the *Insertable B-Layer* (IBL) [27]. It was designed to be very radiation hard in order to be able to cope with the rising instantaneous luminosity. Furthermore, it reduces the distance from the bunch crossing to the innermost layer of detectors to roughly 32 mm, allowing for a better localisation of displaced vertices (caused e.g. by *b*-jets).
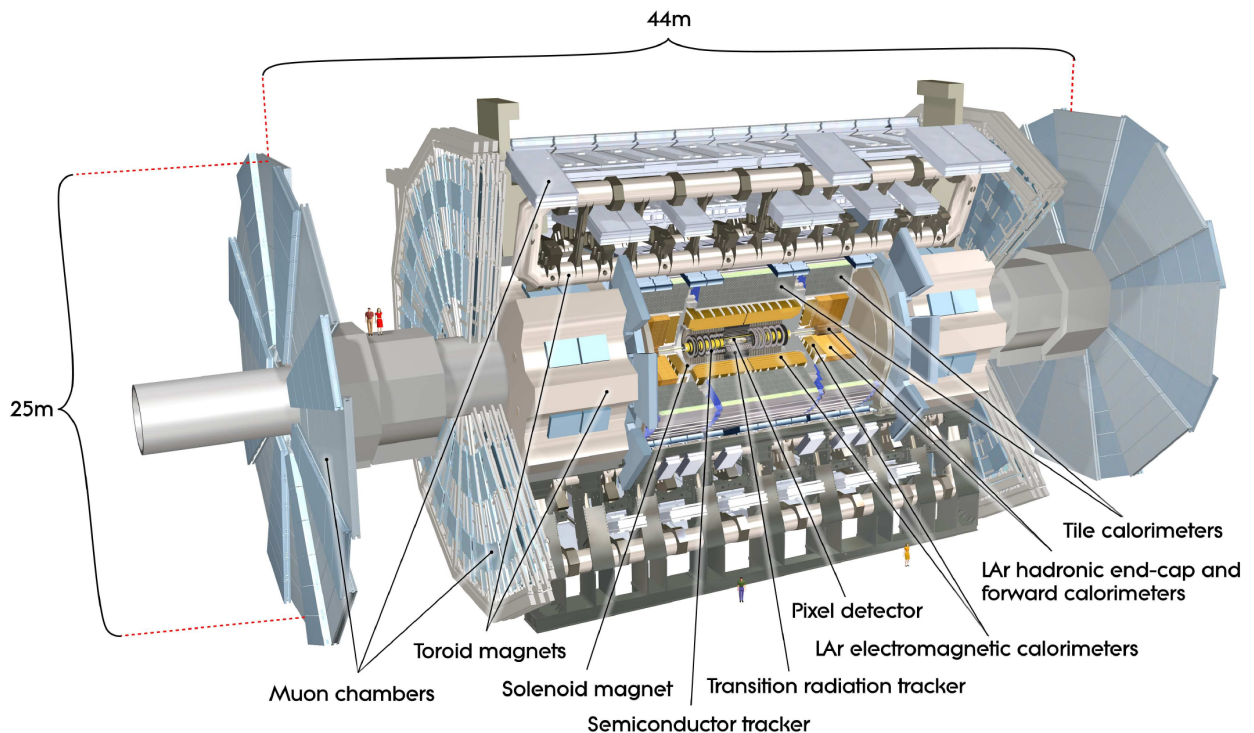
Figure 4.4: Cut-away view of the ATLAS detector [24].

4.1.2 Calorimeters

The calorimeters measure the energy of a particle by inducing electromagnetic and hadronic showers. For a good resolution, all products of a shower must be contained in the system. The size of such a shower depends on the radiation length of the material in the calorimeter, X_0, and the energy and mass of the incoming particle.

For the ATLAS calorimeter system, a combination of active material for the readout and a passive material to induce showering is used. It can be divided into the *Electromagnetic Calorimeter* (ECal) and the *Hadronic Calorimeter* (HCal) around it. Almost all incoming electrons and photons are stopped by the ECal. The HCal is needed to also stop hadronically showering particles. As photons leave no track in the Inner Detector, their detection in the calorimeters is particularly crucial. Therefore, the ECal was designed with a very high granularity, especially in the innermost layer. It uses liquid Argon as active material and Lead as well as stainless steel to induce the showering. The ECal covers $|\eta| < 1.475$ with its barrel and $1.375 < |\eta| < 3.2$ with the two end-caps. Using about 180,000 readout channels, the granularity varies between 0.025×0.025 and 0.1×0.1 in terms of $\Delta\eta \times \Delta\phi$, depending on $|\eta|$ [24].

In contrast to the ECal, the HCal uses different material in the barrel and the end-cap

Name of Calorimeter	relative Energy Resolution σ_E/E
ECal	$10\%/\sqrt{E \ [\text{GeV}]} \oplus 0.7\%$
HCal	$50\%/\sqrt{E \ [\text{GeV}]} \oplus 3\%$
FCal	$100\%/\sqrt{E \ [\text{GeV}]} \oplus 10\%$

Table 4.1: Relative energy resolutions of the different calorimeter systems.

part. In the barrel, steel is used as passive material and scintillating tiles are used as active material. The barrel part covers $|\eta| < 1.7$. The part of the HCal that lies in the end-caps uses a combination of liquid Argon and Copper. It extends the covered region to $|\eta| < 3.2$.

The very forward region of the ATLAS detector ($3.1 < |\eta| < 4.9$) is covered by the *Forward Calorimeter* (FCal) which uses liquid Argon as an active material and Copper (tungsten) as a passive material for the electromagnetic (hadronic) detection. A summary of the resolutions of the different calorimeter systems is listed in Table 4.1.

4.1.3 Muon Chambers

The probability of a particle interacting with the electromagnetic calorimeter decreases quickly with its mass (e.g. Bremsstrahlung: $\Delta E \propto \frac{1}{m^4}$). This makes it very unlikely for muons to interact with it. Therefore, a dedicated muon spectrometer is installed. It is also split into a barrel- end-cap part, located at the outermost layer, so that no other detectable particles will reach it. Two strong end-cap magnets provide bending power for muon tracks, which - in combination with the three layers of high precision tracking chambers - lead to an excellent muon momentum resolution. The muon spectrometer uses different techniques to reconstruct trajectories of muons. For precision tracking, *Monitored drift tubes* are used in the end-caps ($1.6 < |\eta| < 2.7$) and the barrel ($|\eta| < 1.4$). In the end-caps, there are additional *Cathode Strip Chambers*. These have a high granularity in the region $2.0 < |\eta| < 2.7$. *Resistive plate chambers* in the barrel and *Thin-gap chambers* in the end-caps are used for triggering (see Section 5.1), since they provide a very fast readout. All in all, the muon spectrometer consists of about one million readout channels and has a relative transverse momentum resolution of $\sigma_{p_T}/p_T = 10\%$ at $\sqrt{s} = 1$ TeV [24].

4.1.4 Trigger System

The event rate at the ATLAS detector is about 40 MHz. This is way too high to save information on every event. Therefore, the *Trigger and Data Acquisition* (TDAQ) [28] system filters out only interesting collisions, reducing the event rate to about 1 kHz [29]

saved for further off line analysis. This is achieved with a hardware based *Level-1 Trigger* (L1) and a software based *High Level Trigger* (HLT).

At first, the L1 trigger defines so-called *Regions-of-Interest* (RoI) within the detector. To do so, custom electronics use coarse granularity information from the muon chamber and the calorimeters, reducing the event rate to roughly 100 kHz [30]. For each accepted event, the L1 trigger takes a maximum of 2.5 μs. These RoIs are then transmitted to the HLT which further reduces the event rate to about 1 kHz. To do so, roughly 30000 processing units readout the full granularity detector information and apply sophisticated selection algorithms.

Typical objects that "fire" a trigger are (among others) jets, electrons, photons, tau leptons, or muons with a high transverse momentum. But also other interesting signatures like a high missing transverse energy are considered.

4.2 Monte Carlo Generators, Parton Showering Models, and Detector Simulation

In order to compare Monte Carlo generated samples to data samples that were recorded by the ATLAS detector, three steps have to be undertaken. At first, the hard process that corresponds to a Feynman diagram is simulated using Matrix element calculations. Then, the hadronisation of the resulting particles is simulated using *parton showering models*. The results are then processed by a detector simulation. After this step, the Monte Carlo generated events are processed in the same way as data taken by the ATLAS detector (triggers, object reconstruction, final selection criteria).

The Monte Carlo generated samples that are used by this analysis are produced with the ATLAS simulation infrastructure [41]. Every sample was generated during the 2015 production campaign (*mc15c*). A detailed list of all samples that are used is displayed in A.3.

W+jets samples are modelled with SHERPA 2.2 generator [42] and showered with the included showering mechanism. Z+jets, $t\bar{t}$, and single top samples are modelled with POWHEG [43], where PYTHIA 8 was used for showering for the Z+jets samples. For all other samples that were generated using POWHEG, PYTHIA 6 was used for showering [44]. The diboson samples are generated and showered with SHERPA [45].

The Monte Carlo generated signal samples have been produced using POWHEG and MAD-GRAPH5_AMC@NLO 2.1.2 [46][47] for the gluon-gluon fusion and b-associated production, respectively. In both cases, PYTHIA 8.2 [48] was used for showering. Due to many events with a negative weight that were generated by MADGRAPH5_AMC@NLO

Process	Monte Carlo Generator	Parton Showering Model
W+jets	SHERPA 2.2	SHERPA 2.2
Z+jets	POWHEG	PYTHIA 8
$t\bar{t}$	POWHEG	PYTHIA 6
single top	POWHEG	PYTHIA 6
diboson	SHERPA	SHERPA
ggH	POWHEG	PYTHIA 8.2
bbH	MADGRAPH5_AMC@NLO 2.1.2	PYTHIA 8.2

Table 4.2: Summary of Monte Carlo generators und parton showering models used in the analysis.

2.1.2, a relatively large amount of signal events from the b-associated production have to be generated in order to grant comparable statistical uncertainties. To save time, a fast simulation, ATLFAST-II [49], is used in this case. For all other samples, the full simulation is used. A summary of the Monte Carlo generators and the parton showering models used in this analysis is listed in Table 4.2.

In order to compare Monte Carlo generated events to data, GEANT4 [41][50] is used to simulate what signatures the generated samples would cause in the ATLAS detector.

5 Overview of the Existing Analysis

The analysis is driven by the search for BSM Higgs bosons decaying to two τ leptons which themselves both decay hadronically. In this case, the BSM Higgs bosons can be identified as neutral scalars H^0 and A^0 mentioned in Section 3.5.1. In September 2017, the analysis published their results based on a 36.1 fb^{-1} dataset from run 2 with a centre of mass energy of $\sqrt{s} = 13$ TeV [31]. As a final result, exclusion limits in the $m_A - \tan\beta$ plane were derived. These can be seen for the m_h^{mod+} and hMSSM scenario in Fig. 5.1, separately. Here, the results of the $\tau_{\text{lep}}\tau_{\text{had}}$ decay channel are also included which considers the case of one τ lepton decaying leptonically, while the other one decays hadronically.

This Chapter covers the major aspects of the analysis' strategy. At first, the object reconstruction and identification are explained. Then, the event selection in the signal region is discussed. Here, focus lies on how the analysis becomes sensitive for high masses, and how it is distinguished between heavy Higgs particles produced in gluon-gluon-fusion and those originating from b-associated production.

The background estimate is discussed in 5.3. Among others, the analysis considers three control regions for the background estimate that are important throughout the course of this thesis. These regions are defined by a set of selection criteria, each, which are summarised in Section 5.4.

For completeness, the version of the analysis considering one leptonically and one hadronically decaying τ lepton (lephad channel) will is also described at the end of this chapter in Section 5.5.

5.1 Object Reconstruction and Identification

In the following, it will be briefly explained how physical objects (particles) are reconstructed using the information retrieved from the various parts of the ATLAS detector. For a signal to be classified as an electron candidate, there must be an energy deposit in the electromagnetic calorimeter associated with a charged particle track found in the inner detector. These candidates are required to pass a "loose" likelihood-based identification [32]. Additionally, their transverse energy must be $E_{\text{T}} > 15$ GeV and they must
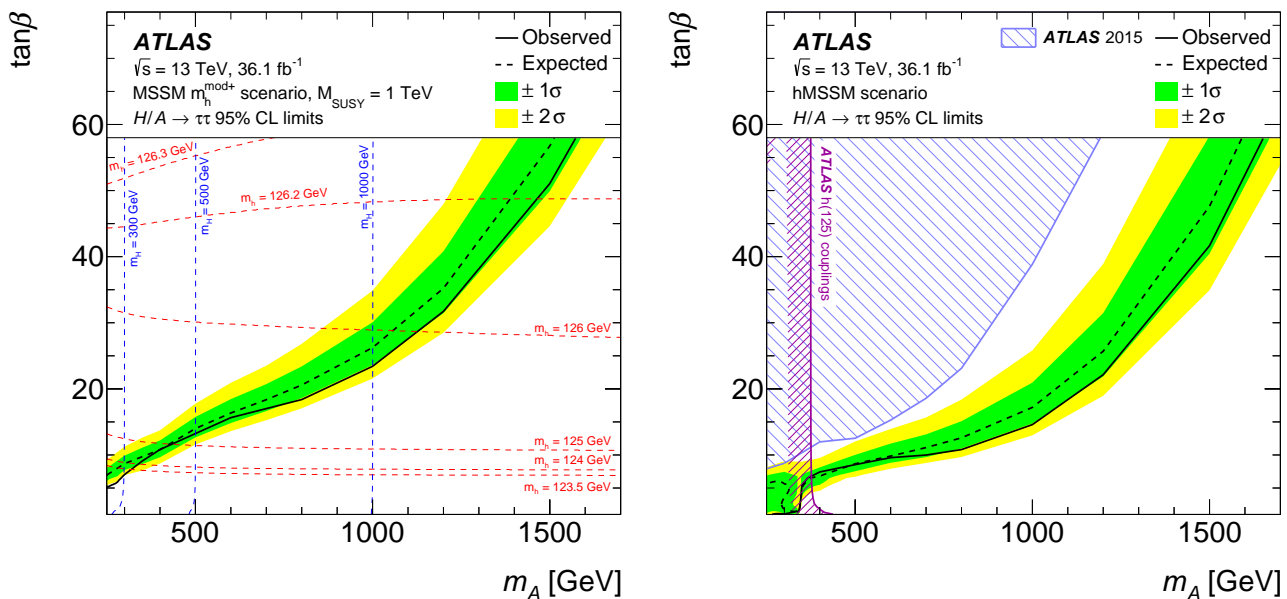
Figure 5.1: The observed and expected 95% CL upper limits on $\tan\beta$ as a function of m_A for the combination of $\tau_{\text{lep}}\tau_{\text{had}}$ and $\tau_{\text{had}}\tau_{\text{had}}$ channels in the m_h^{mod+} and hMSSM scenarios [31]. Every combination of m_A and $\tan\beta$ in the parameter space above the black line can be excluded with a probability of at least 95%. A significant deviation of the observed exclusion limits from the expected (SM background only) would hint at BSM.

be in the fiducial volume of the inner detector, $|\eta| < 2.47$.

Muon candidates that are registered in the muon chambers must match with tracks measured in the inner detector within $|\eta| < 2.5$ and pass a "loose" identification [33]. Their trajectories are reconstructed using information from the inner detector tracks and the muon chambers. Furthermore, their transverse momentum must fulfill $p_{\text{T}} > 15$ GeV.

The jet reconstruction is based on topological clusters in the calorimeter [34]. It uses the anti-k_t algorithm with a radius parameter of $R = 0.4$ [35]. A jet vertex tagger is used to reduce the effect of pile-up according to common recommendations [36][37]. Here, a multivariate technique is used to determine the likelihood that a jet originates from pile-up [37]. Another multivariate algorithm, known as MV2c10, is used to identify jets originating from b quarks, also known as b-jets [38]. Only jets with $p_{\text{T}} > 25$ GeV and $|\eta| < 2.4$ are considered. The working point is chosen to have an efficiency of 70% for b-jets in simulated $t\bar{t}$ events. At this working point, jets initiated by light quarks or gluons, τ-jets, and c-jets have 0.26%, 1.8%, and 8% probability to be misidentified as a b-jet, respectively, according to simulated $t\bar{t}$ events.

As mentioned in Section 2.2, hadronic τ decays are characterised by the presence of one

or three tracks with a neutrino and several neutral mesons (mostly π^0). The first step of the reconstruction of hadronic τ decays is forming candidates out of the visible decay products, which are referred to as $\tau_{\text{had-vis}}$ candidates. Only jets with $p_{\text{T}} > 10$ GeV are considered. There must be energy deposits in the calorimeters within $|\eta| < 2.5$ (the transition region between the barrel and end-cap calorimeters, $1.37 < |\eta| < 1.52$, also known as crack region, is excluded). Furthermore, the $\tau_{\text{had-vis}}$ candidate must have $p_{\text{T}} > 20$ GeV and an electric charge of $+1$ or -1. To obtain large background rejection, a multivariate Boosted Decision Tree (BDT) identification is used on the $\tau_{\text{had-vis}}$ candidates. It is based on several properties of this candidate such as its charge multiplicity and the shower shape in the calorimeter. Based on the same BDT, two identification criteria are defined: ”loose“ and ”medium“. These have efficiencies of about 60% (50%) and 55% (40%) for 1-prong (3-prong), respectively [39].

Geometrically overlapping objects are removed according to the following priorities:

- Jets within a $\Delta R = 0.2$ cone around a selected $\tau_{\text{had-vis}}$ candidate are excluded.

- Jets within a $\Delta R = 0.4$ cone around an electron or muon are excluded.

- Any $\tau_{\text{had-vis}}$ candidate within a $\Delta R = 0.2$ cone around a muon is excluded.

- Electrons within a $\Delta R = 0.2$ cone around a muon are excluded.

Since neutrinos do not interact with any part of the detector, physical events with neutrinos in the detector produce some momentum or energy in the transverse plane that is not detected. The magnitude of this missing transverse momentum, $E_{\text{T}}^{\text{miss}}$, is reconstructed by adding up the transverse momenta of all physical objects of that event and taking the magnitude of the resulting vector [40]. This procedure also takes inner-detector tracks into account that are not associated to reconstructed objects.

5.2 Event selection

In the $\tau_{\text{had}}\tau_{\text{had}}$ channel, events are required to fire a single τ trigger. Over time, this trigger changed as the LHC instantaneous luminosity rose over time to keep pile up low. Which trigger was used at a data taking period and the corresponding amount of collected data are listed in Table 5.1.

The $\tau_{\text{had-vis}}$ candidate that geometrically matches the object that triggered the event is defined as the *leading* $\tau_{\text{had-vis}}$ and must fulfill $p_{\text{T}} > 110$ GeV in case the event was recorded in 2015 or $p_{\text{T}} > 140$ GeV for the other two triggers. The sub-leading $\tau_{\text{had-vis}}$ candidate must pass $p_{\text{T}} > 55$ GeV. Additionally, the leading (sub-leading) $\tau_{\text{had-vis}}$ candidate has to

Name of trigger	data taking period	fraction of collected data
HLT_tau80_medium1_tracktwo_L1TAU60	2015	15%
HLT_tau125_medium1_tracktwo	early 2016	26%
HLT_tau160_medium1_tracktwo	rest of 2016	59%

Table 5.1: Single τ trigger required to be fired with corresponding data taking period and fraction of collected data.

satisfy the "medium" ("loose") τ identification criterion. In order to reduce electroweak background and to grant orthogonality with the $\tau_{\mathrm{lep}}\tau_{\mathrm{had}}$ channel, events with electrons or muons are vetoed. These are identified with the help of the algorithms described in Section 5.1.

The two $\tau_{\mathrm{had\text{-}vis}}$ candidates are required to be back-to-back ($\Delta\phi(\tau_{\mathrm{had\text{-}vis},1}, \tau_{\mathrm{had\text{-}vis},2}) > 2.7$) and of opposite sign.

The signal region (SR) is split into a b-veto and a b-tag category. These are specified to detect Higgs produced by gluon-gluon-fusion or b-associated production, respectively. However, in the case of the b-tag category, the cut on the sub-leading $\tau_{\mathrm{had\text{-}vis}}$ candidate is increased to $p_{\mathrm{T}} > 65$ GeV. The signal efficiency varies between 3.2% at $m_A = 300$ GeV and 16% at $m_A = 1.2$ TeV in the b-veto category and between 0.9% and 6.7% in the b-tag category for the respective production process. Cutflow tables for background processes and hypothetical signals in the b-veto and b-tag signal region are shown in the Appendix in Tables A.6, A.7, and A.8.

5.2.1 Di-τ mass reconstruction

Since some BSM H decays only are differentiated from their SM analogue by the mother particle's mass, a good di-τ mass reconstruction is crucial to separate signal from background. The neutrinos that are present in any τ decay final state, make a full reconstruction very difficult. Therefore, the variable of choice is the so-called *total transverse mass*. It can be expressed as

$$m_{\mathrm{T}}^{\mathrm{tot}} = \sqrt{m_{\mathrm{T}}^2(E_{\mathrm{T}}^{\mathrm{miss}}, \tau_1) + m_{\mathrm{T}}^2(E_{\mathrm{T}}^{\mathrm{miss}}, \tau_2) + m_{\mathrm{T}}^2(\tau_1, \tau_2)}, \tag{5.1}$$

where the transverse mass of two particles, a and b, is defined as

$$m_{\mathrm{T}}(a, b) = \sqrt{2p_{\mathrm{T}}(a)p_{\mathrm{T}}(b)[1 - \cos\Delta\phi(a, b)]}. \tag{5.2}$$

Here, $\tau_{1/2}$ refers to the visible decay products of a τ lepton. In a leptonic decay, these are the charged leptons, and in a hadronic decay, $\tau_{1/2}$ is equal to $\tau_{\mathrm{had\text{-}vis}}$. The distribution of

m_T^{tot} for a signal produced by a heavy Higgs with a mass of $m_{A/H}$ would be a rising slope up to $m_T^{\text{tot}} \approx m_{A/H}$ followed by a abrupt drop. This characteristic shape can be seen as a motivation to use m_T^{tot} as the final discriminant of the analysis.

In Fig. 5.2, the distribution of the total transverse mass is shown for the b-veto signal region.

5.3 Background estimation

The background yields can be split into three different types that are each estimated in a different way:

- Irreducible background from $Z \to \tau\tau$

- Fake τ leptons from QCD multijet processes

- Fake τ leptons from any other process

The first one is estimated by applying the full selection criteria to Monte Carlo generated events. The background emerging from QCD multijet processes is estimated with the help of a fake factor method. For all other backgrounds, a fake rate method is used. The latter two will be explained in Sections 5.3.1 and 5.3.2, respectively.

In Fig. 5.2, the distribution of the total transverse mass in the b-veto signal region is displayed. The corresponding background yields can be seen in Table 5.2 (also for the b-tag signal region). Here, background yields estimated with the help of the fake factor method are coloured in light blue, while the ones estimated with the fake rate technique are coloured in light red. A full cutflow table for all background processes and data is displayed in Table A.6.

Process	b-veto		b-tag	
	yield	% of sum	yield	% of sum
Multijet	3040 ± 17	78.3	106 ± 3	59.4
$Z \to \tau\tau$	613 ± 8	15.8	7.5 ± 1	4.2
$W \to \tau\nu$	178 ± 7	4.6	4.0 ± 0.4	2.2
top	26.2 ± 2.2	0.7	60 ± 3	33.6
Others	24.7 ± 1.9	0.6	1 ± 0.7	0.6

Table 5.2: Background yields in the b-veto and the b-tag signal region. The processes shaded in light blue (red) are estimated using the fake factor (rate) technique. A full cutflow table for all background processes and data is displayed in Table A.6.
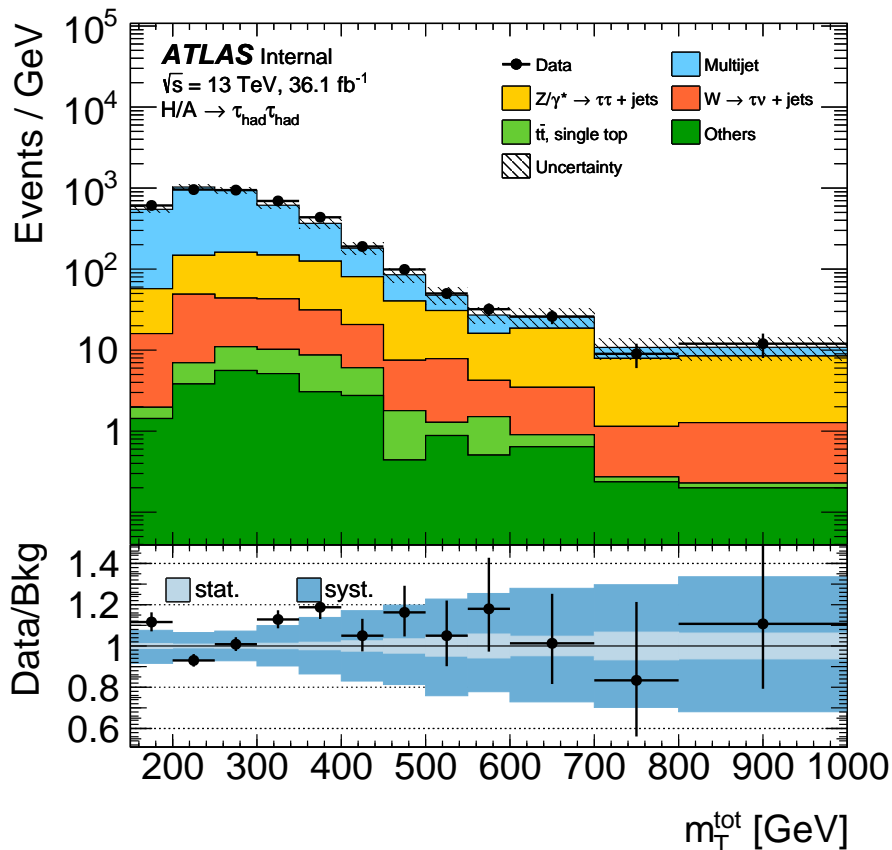
Figure 5.2: Total transverse mass in the *b*-veto signal region.

5.3.1 Multijet background

The biggest background contribution in the signal region comes from multijet processes. Despite the fact that there are no real τ leptons in multijet processes, many of these events pass the selection criteria in the signal region. This is because of jets that are misidentified as $\tau_{\text{had-vis}}$ candidates. To estimate the amount of multijet background, a data driven *fake factor* technique is used. Here, the fake factor is defined as the number of jets that pass the "loose" BDT identification, $N^{\text{pass }\tau-\text{ID}}$, divided by the number of jets

Region	Event yield				
	Data	$Z \to \tau\tau$	$W \to \tau\nu$+jets	top	Others
dijet region	29165	9	111	75	21
anti-ID	142070	458	1528	403	124

Table 5.3: Event yields of data and Monte Carlo generated background in *b*-inclusive dijet and anti-ID region.
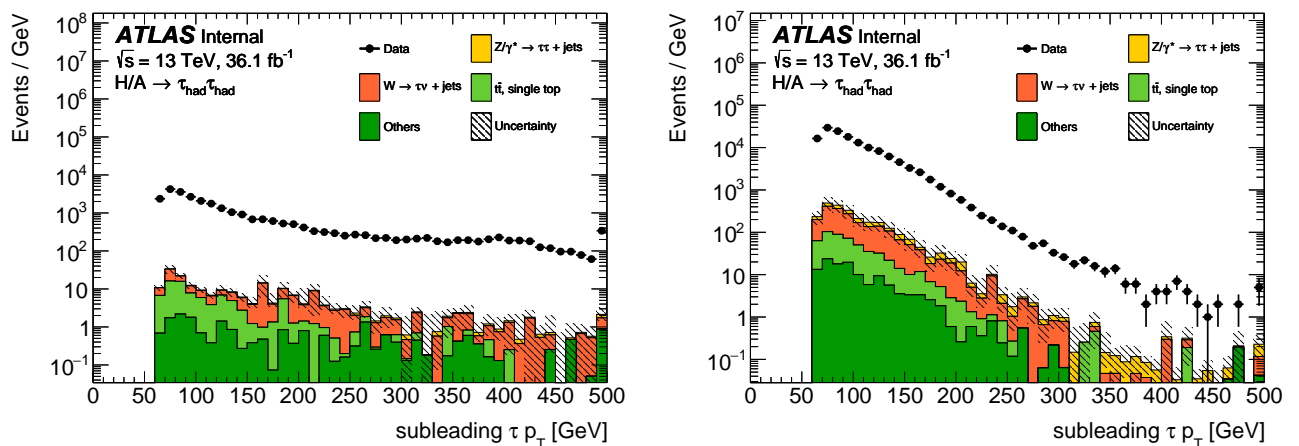
Figure 5.3: Transverse momentum of the subleading $\tau_{\text{had-vis}}$ candidate in the *b*-inclusive dijet region (left) and the anti-ID region (right). The corresponding event yields are listed in Table 5.3.

that fail it, $N^{\text{fail } \tau-\text{ID}}$:

$$F(p_T, N_{\text{track}}) = \frac{N^{\text{pass } \tau-\text{ID}}(p_T, N_{\text{track}})}{N^{\text{fail } \tau-\text{ID}}(p_T, N_{\text{track}})}. \tag{5.3}$$

It is evaluated in a region dominated by dijet events and then applied to events in the signal region.

Since the region in which the fake factors are measured is dominated by dijet events, it will be referred to as *dijet region* in the following. It is designed to be as close to the signal region as possible, while avoiding contamination from real τ leptons. Like the signal region, each event is required to have two $\tau_{\text{had-vis}}$ candidates, of which the leading one must have a transverse momentum that is greater than 85 GeV. Additionally, one of the following single jet triggers must be fired: HLT_j460, HLT_j440, HLT_j420, HLT_j400, HLT_j380, HLT_j360, HLT_j320, HLT_j300, HLT_j260, HLT_j200, HLT_j175, HLT_j150, HLT_j110, HLT_j85, HLT_j60.

The fake factors are then derived in a tag-and-probe method, where the leading $\tau_{\text{had-vis}}$ candidate is defined as the tag and the subleading $\tau_{\text{had-vis}}$ candidate is defined as the probe jet. The tag and probe jets are required to be back-to-back ($\Delta\phi > 2.7$), and the transverse momentum of the probe jet must be at least 30% of that of the tag jet. A comprehensive comparison between signal and dijet region can be found in Table 5.4.

As indicated in Eq. 5.3, the fake factor is binned in the transverse momentum and the number of prongs of the probe jet and applied to corresponding events in the so-called anti-ID region, which is like the signal region, where the leading candidate passes the
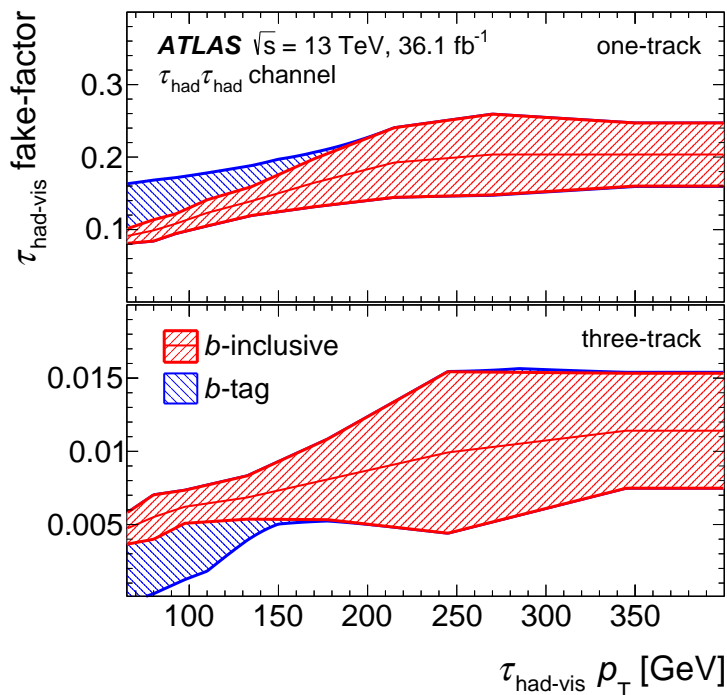
Figure 5.4: The fake factor as a function of the p_T of the τ candidate for one- (top) and three-prong (bottom) [31].

$\tau_{\text{had-vis}}$ identification requirement, while the sub-leading $\tau_{\text{had-vis}}$ candidate fails the "loose" identification (the anti-ID region is the signal region with an inverted ID requirement on the sub-leading $\tau_{\text{had-vis}}$).

Since the fake factors are used to estimate the pure multijet background, Monte Carlo generated events from $Z \to \tau\tau$, $W \to \tau\nu$, $t\bar{t}$, and single top processes (the last two together are referred to as the top background) are subtracted from data in the dijet region before evaluating the fake factors and in the anti-ID region before applying the fake factors. In Fig. 5.3, the distribution of the transverse momentum of the subleading $\tau_{\text{had-vis}}$ candidate is shown for the b-inclusive dijet (left) and anti-ID region (right). Apart from data, the Monte Carlo generated background processes, that are subtracted before evaluating and applying the fake factors, are shown. The corresponding event yields are listed in Table 5.3. In Fig. 5.4, the fake factors can be seen as a function of the p_T of the τ candidate for one- (top) and three-prong (bottom), separately.

5.3.2 Other backgrounds

All other backgrounds that do not emerge from QCD multijet processes are estimated using Monte Carlo simulation. Here, the main sources of background are $Z \to \tau\tau$ (irre-

ducible), $W \to \tau\nu$+jets, and top processes. Apart from the real τ leptons in $Z \to \tau\tau$ events, the main contribution emerges from jets that are misidentified as hadronically decaying τ leptons. To estimate the background contribution from these falsely identified jets, a *fake rate* technique is used. The fake rate is defined as the number of leading $\tau_{\text{had-vis}}$ candidates that pass the BDT identification, $N^{\text{pass }\tau-\text{ID}}$, divided by the number of leading $\tau_{\text{had-vis}}$ candidates, N^{all}. Like the fake factor, the fake rate is binned in p_T and the number of tracks:

$$FR(p_T, N_{\text{track}}) = \frac{N^{\text{pass }\tau-\text{ID}}(p_T, N_{\text{track}})}{N^{\text{all}}(p_T, N_{\text{track}})} \tag{5.4}$$

and measured on data in a separate control region, known as the W+jets region. Here, a single muon trigger with $p_T > 55$ GeV must be fired. The leading $\tau_{\text{had-vis}}$ candidate must fulfill $p_T > 50$ GeV and there is a loosened back-to-back requirement, $\Delta\phi(\tau_1, \tau_2) > 2.4$. Depending on the BDT identification criterion used in Eq. 5.4, fake rates can be evaluated for the "loose" or the "medium" working point. Due to the selection criteria in the signal region, the "medium" fake rates are applied to all leading $\tau_{\text{had-vis}}$ candidates on Monte Carlo generated events in the signal region (without any ID) that are not geometrically matched to a true τ lepton. Analogous, the "loose" fake rates are applied to the sub-leading $\tau_{\text{had-vis}}$ candidates, so that every Monte Carlo generated event is weighted with two fake rates for the background estimation. Of course, for each $\tau_{\text{had-vis}}$ candidate, the fake rate in the corresponding bin in transverse momentum and number of prongs is applied. Furthermore, the fake rate control region is split into a b-veto (dominated by $W \to \mu\nu$jets events, 92%) and a b-tag region (dominated by top events, 82%). The fake rates measured in the b-tag category are applied to the $t\bar{t}$ and single top background in the signal region, whereas the fake rates from the b-veto control region are applied to all other Monte Carlo backgrounds.

5.4 Summary of Sets of Selection Criteria

During the course of this thesis, the complete background estimate was revisited. Because of this, there are two regions that are of major importance apart from the signal region. The dijet region is where the fake factors are measured. The W+jets region is where the fake rates are measured. Later, it will also be used as an alternative region to measure the fake factors. Merging the signal and the anti-ID region results in the signal region without the ID on the subleading τ candidate, which will be referred to as signal and control region (SCR). In Table 5.4, a list with all selection criteria for each region is shown.

In general, control regions are desired to be similar to the signal region with the exception of supressing the signal and enhancing a distinct type of process, instead. For the dijet region, this is achieved by requiring a jet instead of a τ trigger to be fired. Furthermore, the ID requirement on the leading τ candidate is removed.

In the W+jets region, $W(\to \mu\nu)$+jets events are enhanced by a μ trigger that was fired and by requiring a μ lepton instead of vetoing it. To supress contributions from $Z \to \tau_{\text{lep}}\tau_{\text{had}}$, the missing transverse mass has to exceed 40 GeV.

Dijet region	SCR	W+jets region
each $p_T(\tau_{\text{had-vis}}) > 50$ GeV		
e veto		
every jet $p_T > 20$ GeV		
>2 $\tau_{\text{had-vis}}$ candidates		1 $\tau_{\text{had-vis}}$, 1 $\tau_{\text{lep-vis}}$ candidate
μ veto		μ tag
$\Delta\phi > 2.7$		$\Delta\phi > 2.4$
single jet trigger is fired	single τ trigger is fired	single μ trigger is fired
	leading τ trigger matched	μ trigger matched
leading τ $p_T > 100$ GeV	leading τ $p_T > 85$ GeV	leading leptonic τ $p_T > 55$ GeV
	subleading τ $p_T > 65$ GeV	leading hadronic τ $p_T > 50$ GeV
subleading τ p_T / leading $\tau p_T > 0.3$	leading τ passes "medium" ID	missing $E_T > 40$ GeV

Table 5.4: Selection criteria that define the three regions that are most important throughout this thesis.

5.5 Lephad Channel

The analysis also considers the case that one τ lepton decays leptonically and the other one decays hadronically, known as the *lephad* channel. Since this decay channel is of minor importance for the rest of this thesis, it will only be discussed very briefly.

Only events are considered where a single muon or a single electron trigger is fired with lower p_T thresholds ranging from 20 to 140 GeV [31]. Like in the fully hadronic case, the signal region is split into a b-veto and a b-tag category. Depending on the trigger that fired, the decay channel is further split into $\tau_e\tau_{\text{had}}$ and $\tau_\mu\tau_{\text{had}}$ and corresponding isolation criteria are applied to the lepton. Any event is required to contain at least one $\tau_{\text{had-vis}}$ candidate that passes the "medium" BDT identification and exactly one isolated lepton that is matched to the respective trigger that fired. The isolated lepton and the $\tau_{\text{had-vis}}$ candidate must be back-to-back $\Delta\phi > 2.4$ and have opposite charges. The transverse mass between the isolated lepton and E_T^{miss} is required to be lower than 40 GeV to reduce background from W+jets processes. In the $\tau_e\tau_{\text{had}}$ channel, events where the isolated lep-
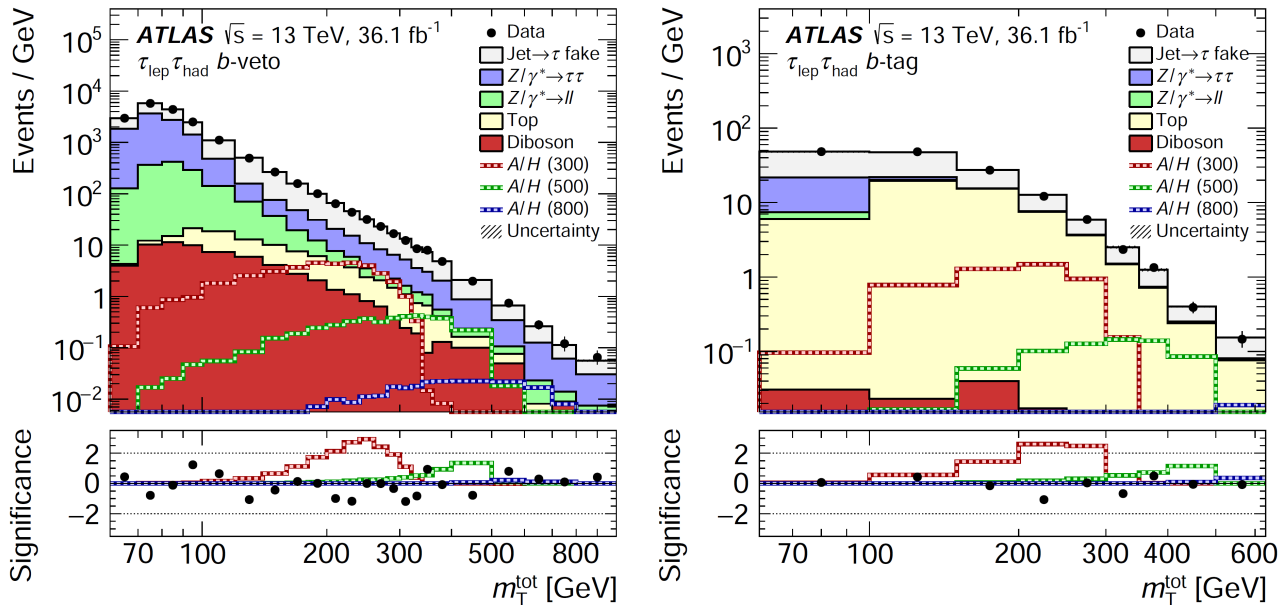
Figure 5.5: Total transverse mass in the lephad decay channel for the b-veto (left) and b-tag category (right) [31]

ton the $\tau_{\text{had-vis}}$ candidate have an invariant mass between 80 and 110 GeV are rejected to reduce background from $Z \to ee$ processes. Depending on the assumed mass of the heavy Higgs boson, the signal efficiency times acceptance lies between 1% and 7% and peaks around 0.8 TeV [31], making this decay channel best suited for the detection of slightly less heavy Higgs bosons than the fully hadronic decay channel.

The biggest background yield emerges from processes where a quark or gluon initiated jet is falsely identified as the $\tau_{\text{had-vis}}$ candidate. These are further split into the case where the isolated lepton is correctly identified and those where it is not. Both contributions are estimated with a data driven fake factor method which slightly deviates from the one used in the fully hadronic decay channel. Events where the isolated lepton and the $\tau_{\text{had-vis}}$ candidate arise from electrons (or muons) mainly emerge from $Z \to \tau\tau$ processes and are estimated using Monte Carlo simulation.

Like in the fully hadronic case, the total transverse mass is used as the final discriminant. In Fig. 5.5, it is shown for data, background and three different signal hypotheses, assuming and $m_A = 300$ GeV, $m_A = 500$ GeV, and $m_A = 800$ GeV, respectively. For every of those signals, $\tan\beta = 10$ was assumed.

5 Overview of the Existing Analysis

6 Improvement of the Fake Rate Technique

The first task of this master's thesis was to investigate and improve the fake rate method for the analysis with the full dataset of 36 fb^{-1}. The following details these investigations that lead to a more robust background estimate.

6.1 Influence of $\Delta\phi$ Cuts in Signal and Control Regions

As a first step, the influence of the $\Delta\phi$ cuts was investigated. In the signal region, there is a cut of $\Delta\phi(\tau_{\text{had-vis,1}}, \tau_{\text{had-vis,2}}) > 2.7$, whereas in the W+jets fake rate control region, this quantity is only required to be greater than 2.4. However, consistency between signal and control region is ideal to avoid unwanted biases in the background estimate. In [51], the $\Delta\phi$ cut in the fake rate region is justified by the suppression of multijet background. To verify if this is also the case for the Signal Region, the p_T distribution of the leading $\tau_{\text{had-vis}}$ candidate is shown in Fig. 6.1 with $\Delta\phi > 2.7$ and the orthogonal cut, $\Delta\phi < 2.7$, respectively. The corresponding yields are given in Table 6.1. In fact, with $\Delta\phi > 2.7$, roughly 81% of the background is caused by multijet processes, whereas the orthogonal cut, $\Delta\phi < 2.7$, only allows roughly 63% multijet background.

Similar investigations were conducted for the $\Delta\phi$ cut in the W+jets fake rate control region. Here, the background is modelled using $W \to \mu\nu$, $W \to \tau\nu$, $Z \to \tau\tau$, $t\bar{t}$, and

	$\Delta\phi(\tau_1, \tau_2) > 2.7$		$\Delta\phi(\tau_1, \tau_2) < 2.7$	
Process	Event Yield	percentage of sum	Event Yield	percentage of sum
Others	16.8	0.59	15.3	1.3
$t\bar{t}$, single top	16.0	0.56	10.0	0.86
$W \to \tau\nu$+jets	125.0	4.4	64.8	5.6
$Z/\gamma \to \tau\tau$ +jets	398	14.0	351	30.2
Multijet	2294	80.5	720.56	62.0

Table 6.1: Background yields with orthogonal $\Delta\phi$ cuts in the b-veto signal region.

Figure 6.1: Leading τ $p_{\rm T}$ distribution in the b-veto signal region with $\Delta\phi > 2.7$ (left) and $\Delta\phi < 2.7$ (right).

	$\Delta\phi(\tau_1, \tau_2) > 2.4$		no $\Delta\phi(\tau_1, \tau_2)$ cut	
Process	Event Yield	percentage of Data	Event Yield	percentage of Data
Data	116606		159386	
$Z \to \tau\tau$	595	0.51	808	0.50
$t\bar{t}$	2744	2.4	5440	3.4
$W \to \mu(\tau)\nu$	97540	83.6	137377	86.2
Data$-$Sum (QCD)	15727	13.5	15761	9.9

Table 6.2: Yields in the b-veto, 1-prong W+jets fake rate control region with and without $\Delta\phi$ cut.

single top Monte Carlo samples. The difference between the Monte Carlo background and the events in data is then assumed to originate from QCD processes. This comparison can be seen in Table 6.2. Again, the cut enhances multijet background instead of suppressing it.

Although the multijet background is not suppressed by the $\Delta\phi$ cuts that are applied in the signal region and in the fake rate control region, they might still be useful. For example, the modelling in the signal region seems to be improved with $\Delta\phi > 2.7$ compared to the orthogonal cut, as it can be seen in Fig. 6.2. Additionally, a heavy Higgs boson would cause the trajectories of its decay products to be more back-to-back. Therefore, the $\Delta\phi > 2.7$ cut could improve the sensitivity in the SR.

In the $\tau_{\rm lep}\tau_{\rm had}$ channel, a $\Delta\phi > 2.4$ cut is imposed in the SR. Since the μ tag is applied in the region for fake rate calculation is also used by the $\tau_{\rm lep}\tau_{\rm had}$ channel, this can be seen
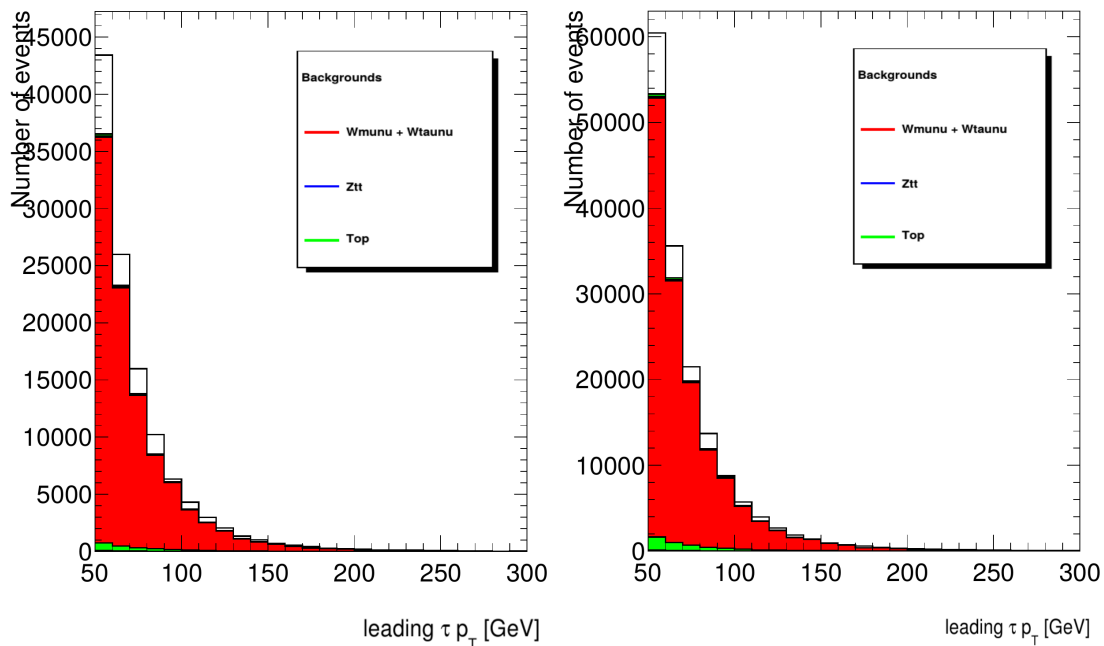
Figure 6.2: Leading τ p_{T} distribution in the b-veto, 1-prong W+jets fake rate control region with (left) and without $\Delta\phi(\tau_1, \tau_2) > 2.4$ cut (right).

as a motivation for this cut.

After these investigations, the decision was made to leave the $\Delta\phi$ cuts untouched.

6.2 Real τ background and Influence of the MC Generator

As mentioned in Section 5.3.2, all background contributions apart from multijet processes are estimated using fake rates, which are measured on data in the W+jet region. As a cross check, the analysis framework also provides the possibility of calculating the fake rates on Monte Carlo samples in addition to those on data. For the b-veto and the b-tag category, $W \to \mu\nu$ and top samples are used, respectively. In Fig. 6.3, comparisons between fake rates calculated on data and Sherpa $W \to \mu\nu$ Monte Carlo samples in the b-veto category can be seen. They are displayed separately for one-prong (left) and three-prong (right) as well as opposite-sign (top) and same-sign (bottom), resulting in four different plots. Although apparent in every category, especially in the 1-prong opposite-sign case, there is a large discrepancy between the fake rates measured in data and those measured in $W \to \mu\nu$ Monte Carlo samples. This hints at a possible contamination of real τ leptons in the dataset that distort the fake rate measurement. Since real τ leptons are very likely
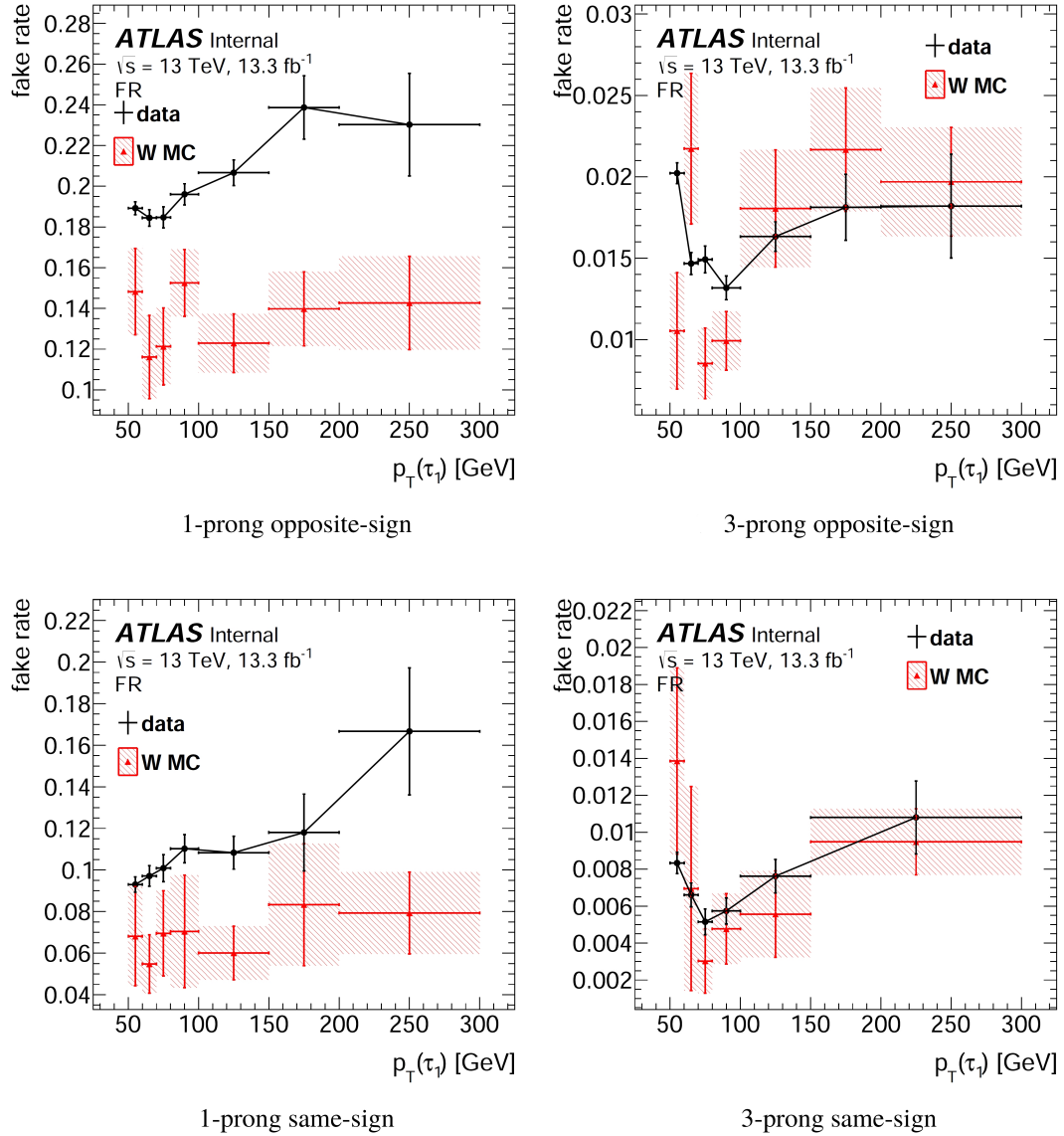
Figure 6.3: Fake rates calculated by the original framework for the "loose" identification working point in the W+jets control region measured on data and $W \to \mu\nu$+jets Monte Carlo. The plots are split into opposite-sign (top) and same-sign (bottom), as well as 1-prong (left) and 3-prong (right).
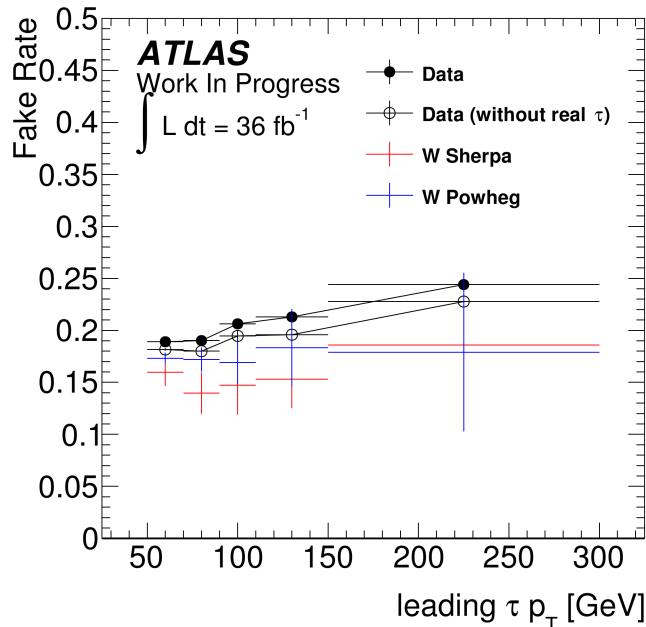
Figure 6.4: Fake rates in the b-veto category measured in data and Monte Carlo samples from two different generators as a function of the p_T of the leading τ candidate.

to pass the BDT based identification criteria, they will make the fake rate appear higher than it actually is. This problem does of course not exist in Monte Carlo samples, since only jets that are not geometrically matched to a true τ lepton are considered in the fake rate calculations.

To solve this problem, $\tau_{\text{had-vis}}$ candidates from Monte Carlo generated events that are geometrically matched to a true τ lepton in the fake rate control region are subtracted from the dataset before the actual fake rate evaluation takes place. For this, truth matched $\tau_{\text{had-vis}}$ candidates emerging from Monte Carlo generated $Z \rightarrow \tau\tau$, $W \rightarrow \tau\nu$, and top processes are considered. The resulting fake rates can be seen in Fig. 6.4 as a function of the p_T of the leading τ candidate. Apparently, subtracting real τ leptons as background lowers the fake rates as expected and improves the consistency between data and MC fake rates. Therefore, it has been used in the background estimation for the analysis using 36.1 fb^{-1} of data [31].

However, the discrepancy between the fake rates measured on data and those measured on Monte Carlo generated samples is not completely resolved by subtracting truth matched τ candidates. To understand what causes the difference between the data and the Monte Carlo fake rates after the subtraction of real τ leptons, the latter will be evaluated using an alternative Monte Carlo generator in the following.

From prior studies it is known that fake rates are not badly modelled as such in Monte Carlo generated events. For these studies, $Z \rightarrow ee$ Monte Carlo samples generated by Powheg were used [52]. To check if fake rates depend on the choice of the generator, they were also evaluated on $W \rightarrow \mu\nu$ Powheg Monte Carlo samples. They are significantly closer to those measured on data, which are within the statistical uncertainties of the prediction as it is also shown in Fig. 6.4. By subtracting real τ background and using Sherpa instead of Powheg as the Monte Carlo generator, the discrepancy between data and Monte Carlo fake rates could be resolved. However, it is still interesting why the fake rates in Sherpa and Powheg samples differ. One of the properties of a sample that was found to have a significant impact on the fake rate is the ratio of quark initiated to gluon initiated jets [52] which is investigated in the next section.

6.3 Quark/Gluon Fraction

Jets from QCD processes can be initiated by a quark or a gluon. Since quark initiated and gluon initiated jets have different properties, they have different probabilities to be misidentified as a hadronically decaying τ lepton [52]. Most notably, quark initiated jets are narrower than gluon initiated jets, which makes them more likely to be misidentified as a hadronically decaying τ lepton (see Fig 2.3). Therefore, the ratio of quark to gluon initiated jets has an impact on the fake rate of a sample.

In order to compare fake rates that were measured in different samples, the different quark/gluon fractions of the samples have to be taken into consideration, which is why this fraction plays an important role for understanding the discrepancy between the fake rates that can be seen in Fig. 6.4.

For Monte Carlo generated samples, the quark/gluon fraction can easily be calculated using the truth information of each event in the detector. On data, however, it is not that simple. Here, a so-called template fit is applied, which uses pure quark and gluon templates of a particular kinematic variable from Monte Carlo generated samples as input in order to determine the quark/gluon fraction. The fitting algorithm takes statistical uncertainties of the templates and of the data sample into account and tries to find a linear combination of the templates that maximises the likelihood to the data sample using Poisson statistics [53]. Obviously, the sum of the templates and data must be normalised to the same integral before this procedure takes place.

In order for the fraction to have an impact on the shape of the result, quark and gluon initiated jets must have a distinct distribution from each other when plotted in dependence of the kinematic variable of choice. The more distinct these distributions are from each

other, the better the *separation* of this variable.

Since quark initiated jets are narrower than gluon initiated jets, the jet width, j, is expected to be a well separating variable and would be the default choice to perform a template fit. It is defined as the weighted average ΔR of all objects within the jet, where the weights are given by the transverse momenta, p_T^i, of the objects [52]:

$$j = \frac{\sum_i \Delta R^i p_T^i}{\sum_i p_T^i} \qquad (6.1)$$

As an alternative, the variable $N_{\text{track}}^{\text{wide}}$ could also be used to conduct the template fits. It is defined as the number of tracks with $0.2 < R < 0.4$ in the $\tau_{\text{had-vis}}$ candidate. Therefore, it is also sensitive to the lateral extent of a jet.

In order to find out, which kinematic variable of the two is suited best for a template fit, their separation performance is compared in the next section.

6.3.1 Separation Performance

To find out, how large of a separation a variable has, the so-called Gini index between the quark and gluon templates can be evaluated. This variable depends on the choice of a cut to distinguish between signal and background (quark and gluon initiated jets in this case), and is defined as

$$G = p \cdot (1 - p), \qquad (6.2)$$

where p is the purity of the signal below the cut. In Fig. 6.5, a schematic depiction of the gini index and its dependence on the purity can be seen. A perfect separation corresponds to a value of $G = 0$, no separation at all corresponds to $G = 0.25$. Note that the Gini index makes no statement on the absolute number of events that are left after the cut.

An alternative and more simple measure on how well two distributions separate is the index T, defined as

$$T = \frac{|\bar{x}_Q - \bar{x}_G|}{\sqrt{RMS_Q^2 + RMS_G^2}}. \qquad (6.3)$$

As soon as the jet width was implemented as a variable, its separating performance was compared to that of $N_{\text{track}}^{\text{wide}}$. In Fig. 6.6, the normalised distributions of quark and gluon initiated jets in dependence of the jet width and $N_{\text{track}}^{\text{wide}}$ of the leading τ candidate can be seen. For each bin, the Gini index is shown, assuming that bin is the last one considered in the integration for the calculation of the purity (the cut value is at the right edge of
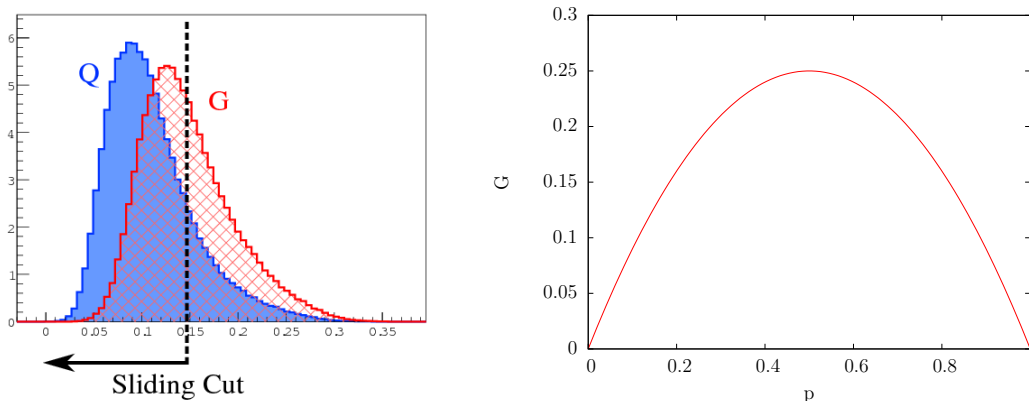
Figure 6.5: Schematic depiction of the Gini index and its dependence on the purity.

that bin). The value of T from Eq. 6.3 is also shown for each distribution. Knowing that the goal is a low Gini index and a high value of T, it is apparent that the jet width is better separating than $N_{\text{track}}^{\text{wide}}$ for Sherpa and Powheg samples. Therefore, the template fits are conducted using the jet width as the kinematic variable, which is discussed in the next section.

6.3.2 Template Fit Using the Jet Width

The template fit is conducted, using the jet width as the kinematic variable, which was found to have a better separation performance than $N_{\text{track}}^{\text{wide}}$. In a Monte Carlo generated sample, the information whether a jet was initiated by a quark or a gluon is extracted from the underlying truth particle that caused the jet [54]. Unfortunately, there are some jets that are not truth matched to a particle, at all. These unmatched candidates seem to have similar properties to gluon initiated jets [52]. Therefore, they are added to the gluon templates and the template fit is repeated. The difference between the results with and without the unmatched candidates is treated as a systematic uncertainty, where the result without the unmatched candidates is defined as the default value. The fit is conducted with quark and gluon templates that were extracted from $W \rightarrow \tau\nu$ Monte Carlo samples generated by Sherpa and Powheg, respectively. The results are summarised in Table 6.3 and the corresponding graphs are displayed in Fig. 6.7.

The higher fraction of gluon initiated jets within the Sherpa sample that was calculated using the truth information on what particle caused the jet and equivalently the lower fraction of quark initiated jets explains why the fake rates measured on Powheg samples are higher than those evaluated on Sherpa samples.

The quark fraction in the data sample is estimated as the mean value of the two fit results
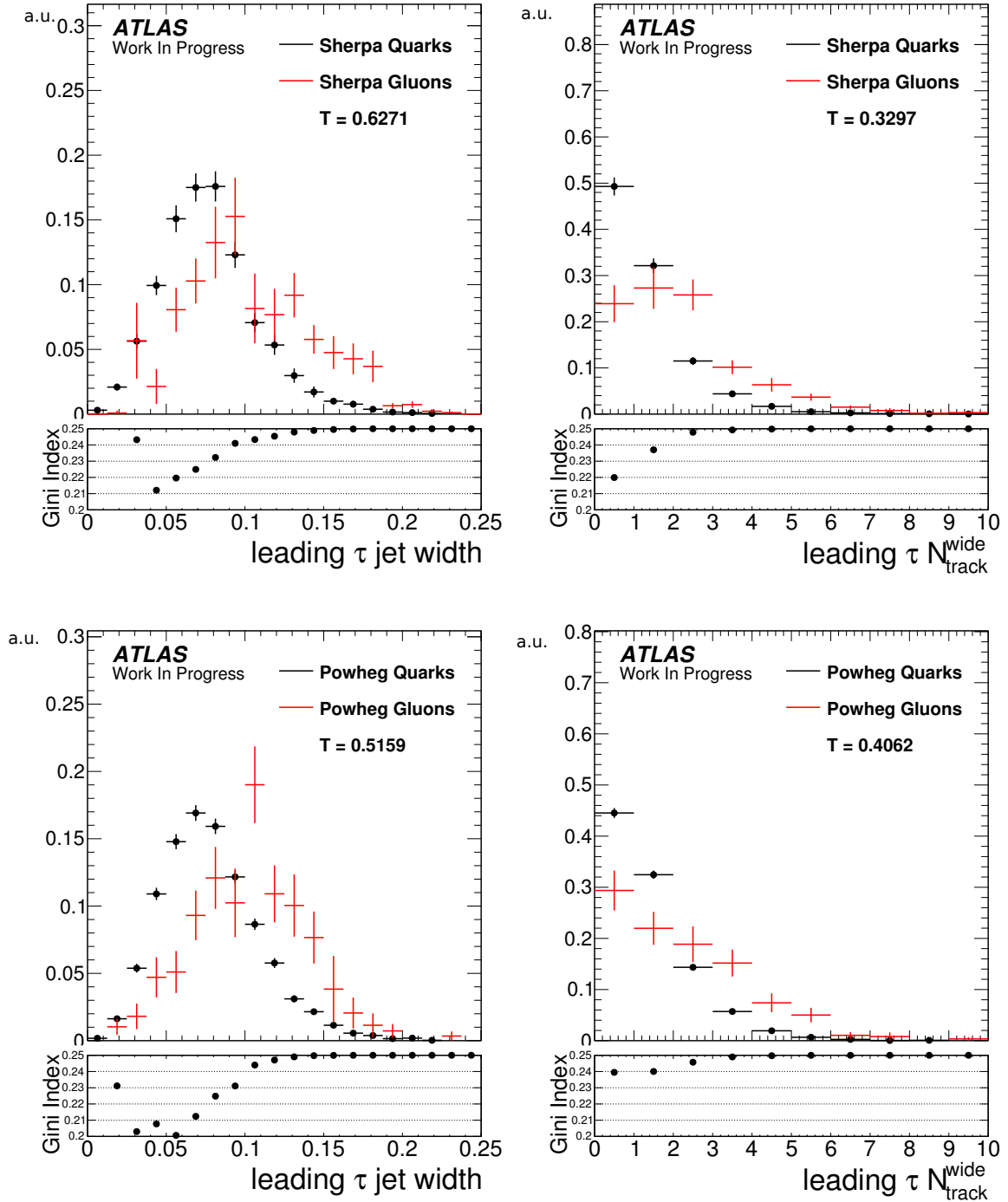
Figure 6.6: Normalised distributions of quark and gluon initiated jets in dependence of the leading τ jet width (left) and leading τ $N_{\text{track}}^{\text{wide}}$ (right) and corresponding Gini indices for Sherpa (top) and Powheg samples (bottom).
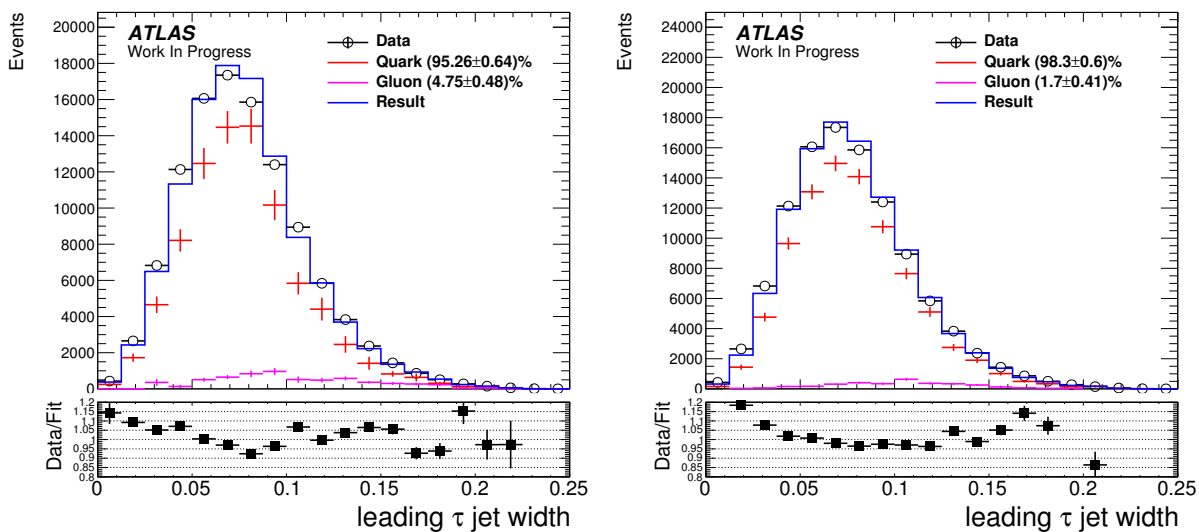
Figure 6.7: Template fits in the W+jets region using the jet width for Sherpa (left) and Powheg samples (right).

Generator	Sherpa	Powheg
% of gluons in MC sample from truth information	7.12 ± 0.54(stat)	3.66 ± 0.26(stat)
% of gluons in data estimated via template fit	4.75 ± 0.48(stat) ± 0.06(sys)	1.7 ± 0.41(stat) ± 0.74(sys)
Combined result in data	3.225 ± 0.32(stat)± 1.57(syst)	

Table 6.3: Results of the template fits using the jet width.

and the difference between the two is taken as an additional systematic uncertainty. All in all, the descending order of quark fractions (data, Powheg MC, Sherpa MC) matches the descending order of the fake rates. The discrepancy between the fake rates of the different samples is understood and traced down to the quark/gluon fraction. Now that it has been shown that the quark/gluon ratio of a sample can have a significant impact on the fake rates measured on that sample, the next step is to make sure that a difference in the quark/gluon ratios between the W+jet region (where the fake rates are measured on data) and the signal region (where the fake rates are applied to Monte Carlo generated samples, see Section 5.3.2) does not introduce a bias to the background estimate.

6.4 Fake Rates in the Signal Region

As explained in Section 5.3, the fake rates are measured in a W+jet control region but applied in the signal region. To make sure that transferring the fake rates from the control
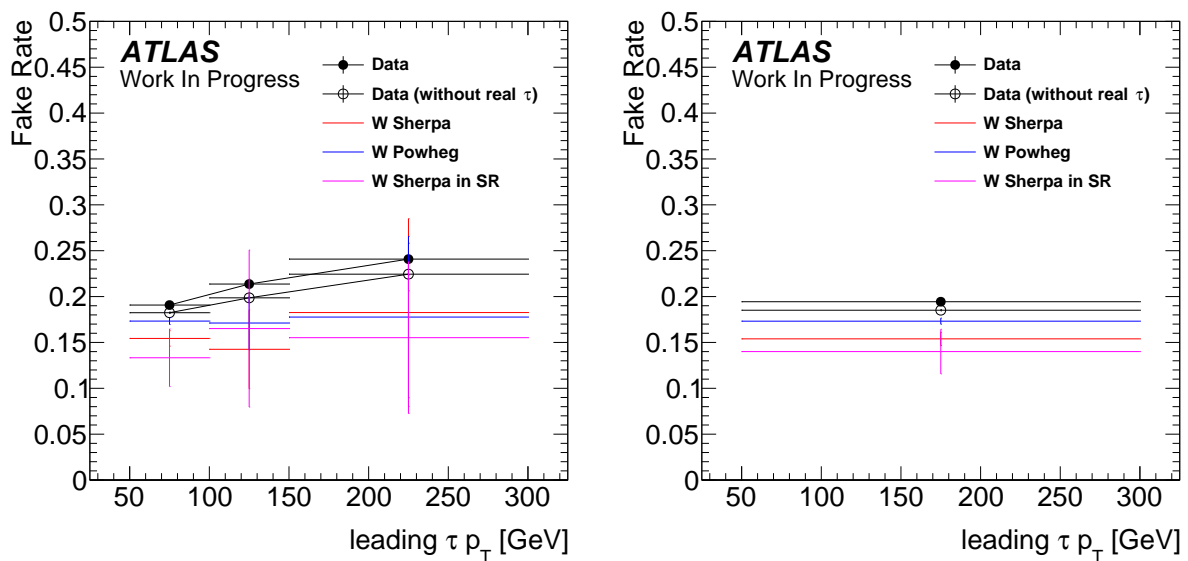
Figure 6.8: Fake rates in the *b*-veto category measured in data and Monte Carlo samples from two different generators and fake rates measured on *W* Sherpa samples in the signal region.

to the signal region does not introduce an unknown bias, the fake rates were also evaluated on the corresponding *W* samples in the signal region (calculating them on data would not be possible due to a potential signal contamination). The result can be seen Fig. 6.8. The gluon fraction within the sample in the signal region is $(8.88 \pm 1.9)\%$ which is compatible with the fake rates being slightly lower than in the control region. However, the uncertainties cover the difference of the fake rates between signal and W+jets region. A possible improvement to the background estimation would be to scale down the fake rates measured on data in the control region by r, the ratio of the fake rates measured on Monte Carlo samples, before applying them in the signal region as the final fake rate, FR_{final}:

$$FR_{\text{final}} = r \cdot FR(\text{Data}, CR), \tag{6.4}$$

with

$$r = \frac{FR(W\text{Sherpa}, SR)}{FR(W\text{Sherpa}, CR)}. \tag{6.5}$$

Since the uncertainties on fake rates in the W+jet control and the signal region overlap, the scaling down of the fake rates according to Eq. 6.5 has not been implemented into the existing analysis framework. However, the subtraction of true τ leptons in the W+jet

control region before measuring the fake rates (see Section 6.2) has been implemented. As shown in Table 5.2, only about 5% of the total background yields in the b-veto category are estimated using the fake rate technique. This and the fact that the uncertainties of the fake rates evaluated on Monte Carlo generated events in signal and W+jet control regions cover each other lead to the conclusion that enough effort had been put into the fake rate technique. Instead, the fake factor method used to estimate roughly 78% of the background yield in the b-veto category is investigated more thoroughly in the following.

7 Improvement of the Fake Factor Method

In this Chapter, the fake factor method used to estimate the background emerging from QCD jets, will be revisited. Like fake rates, fake factors depend on the quark/gluon ratio of the sample in which they are measured. Ideally, the regions where the fake factor is measured and where it is applied should have a compatible quark/gluon ratio. If this is not the case, then corrections to the fake factor must be applied.

The fake factor in a sample of jets can be calculated from the corresponding quark/gluon ratio if the pure quark and gluon fake factors are known. It can also be interpolated between two regions with known fake factors and quark/gluon ratios, which will be discussed in the following. To reduce uncertainties, the two regions should have a big splay in terms of their quark/gluon ratios. Since the dijet region is dominated by gluon initiated jets and the W+jet region is dominated by quark initiated jets, these two were chosen as regions between which the fake factor in the signal region will be interpolated.

Before this interpolation is discussed in detail, the techniques used to estimate the quark/gluon ratio in a data sample, are discussed. Like in Section 6.3, template fits will be conducted.

7.1 Quark/Gluon Template Fits

For three-prong candidates, the fits were conducted in three p_T bins: $50 - 70$ GeV, $70 - 90$ GeV, and $90 - 130$ GeV. In the one-prong case, there were not enough Monte Carlo generated events in the quark and gluon templates to use the same bins. This is because the processes that fake τ candidates tend to produce more three-prong than one-prong candidates. Therefore, only one p_T bin ($50 - 130$ GeV) was used, here. Since quark and gluon initiated jets are believed to have the same correlation between the jet width and p_T for any given production process, quark and gluon templates were extracted from the three following MC processes in the dijet and the signal region:

- $W \rightarrow \tau\nu$
- top (single top and $t\bar{t}$
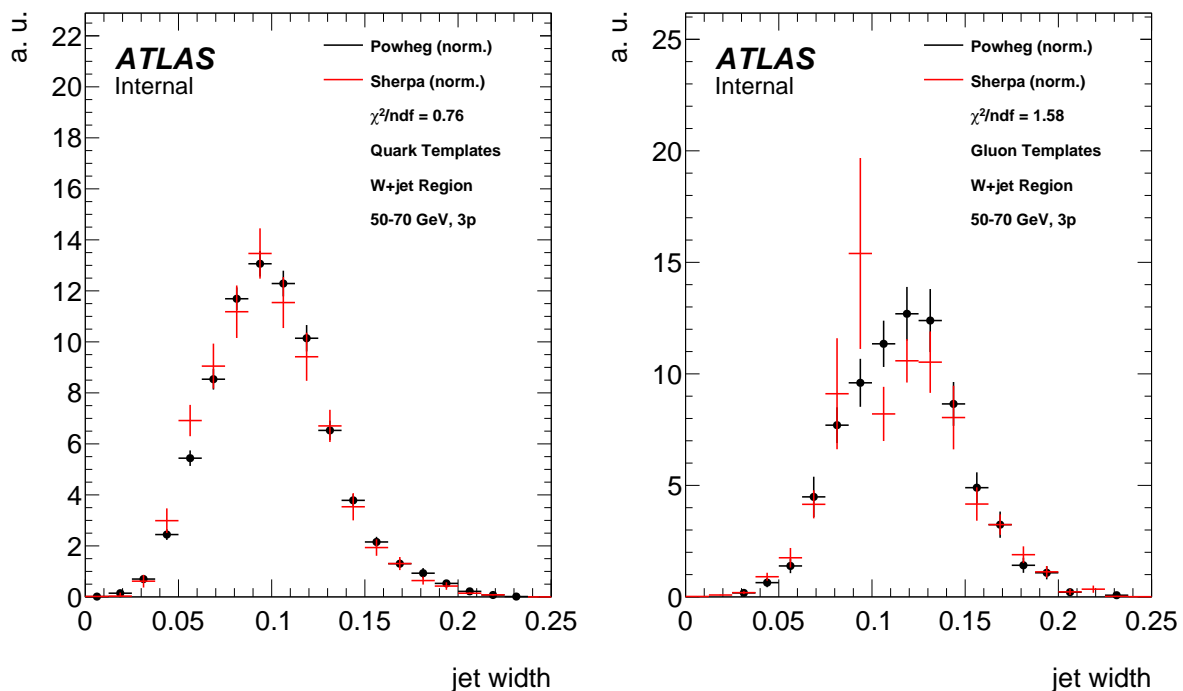
Figure 7.1: Normalised quark (left) and gluon (right) templates extracted from $W \to \mu\nu$ Powheg and Sherpa Monte Carlo in the W+jet, $50-70$ GeV, 3-prong category. A χ^2 test has been conducted to make sure the templates are compatible.

- $Z \to \tau\tau$

Like in the original analysis, the fake factors are derived in a tag-and-probe method. Here, a single jet trigger must be fired and two τ are required. The fake factor is then evaluated on the subleading τ candidate according to Eq. 5.3. Therefore, the template fits were conducted using the jet width of the subleading τ candidate in data and in Monte Carlo for the extraction of the quark and gluon templates.

Like before, $W \to \mu\nu$ Monte Carlo samples are used to extract quark and gluon templates in the W+jet region. This time, however, the templates from the Sherpa and Powheg generators are added together to reduce statistical uncertainties. The templates generated by Sherpa and Powheg have to be compatible. Otherwise, adding them would introduce a bias to the result of the template fit later on. To test their compatibility, the normalised distributions are compared and a χ^2 test is conducted. The templates were found to be compatible. As an example, this comparison for the $50-70$ GeV, 3-prong category can be seen in Fig. 7.1.

7.1.1 Background subtraction

The biggest contribution apart from QCD jets arises from $W \to \tau\nu$, top, and $Z \to \tau\tau$ processes in the dijet region and in SCR. As in the original analysis (see Section 5.3.1), Monte Carlo generated events from these processes that pass the corresponding cut criteria of a region are subtracted from the events in data before the fits are conducted and the fake factors are calculated. This is done to make sure that the measured quark/gluon ratios and especially the fake factors correspond to pure QCD jets.

In the W+jet region, only truth matched τ leptons are subtracted from data as it is described in Section 6.2.

7.1.2 p_T Reweighting of the Templates

For each template fit, the jet width distribution in data and that of the templates have the same p_T cuts applied. However, this does not guarantee compatible p_T distributions within each p_T bin. This can be visualised in Fig. 7.2. On the left hand side, the normalised p_T distribution of the data in the 3-prong, dijet Region is displayed along with the p_T distributions of the corresponding quark and gluon templates that were taken from top processes (the p_T spectra of the other processes were also compared to data, however the effect is strongest for top, which is why it is shown here as an example). In data, the slope is less steep. For any interval, a steeper falling slope in p_T will result in a lower average p_T value. Therefore, the average p_T of the quark and gluon templates in any bin is lower than the corresponding value in data. This would distort the results of the template fits later on. To compensate for this effect, the quark and gluon templates are reweighted to make their p_T distribution match that in data. To do so, every event is weighted by the ratio between the content of the corresponding p_T bin in data and that of the respective quark or gluon template:

$$w_{p_T} = \frac{p_{T_{\text{data}}}}{p_{T_{\text{MC}}}}. \tag{7.1}$$

To minimise the statistical fluctuations of the weights, the bins used for the calculation of the weights get larger with p_T. In Fig. 7.2 (right), the normalised p_T distributions can be seen after reweighting. As can be seen, the quark template, gluon template and data now have consistent p_T distributions. In Fig. 7.3, the effects of the p_T reweighting on the distribution of the jet width can be seen in two different p_T bins. As mentioned above, the p_T reweighting increases the average p_T of the quark and gluon templates. Since jets tend to become more narrow with increasing p_T, the reweighted jet width templates are
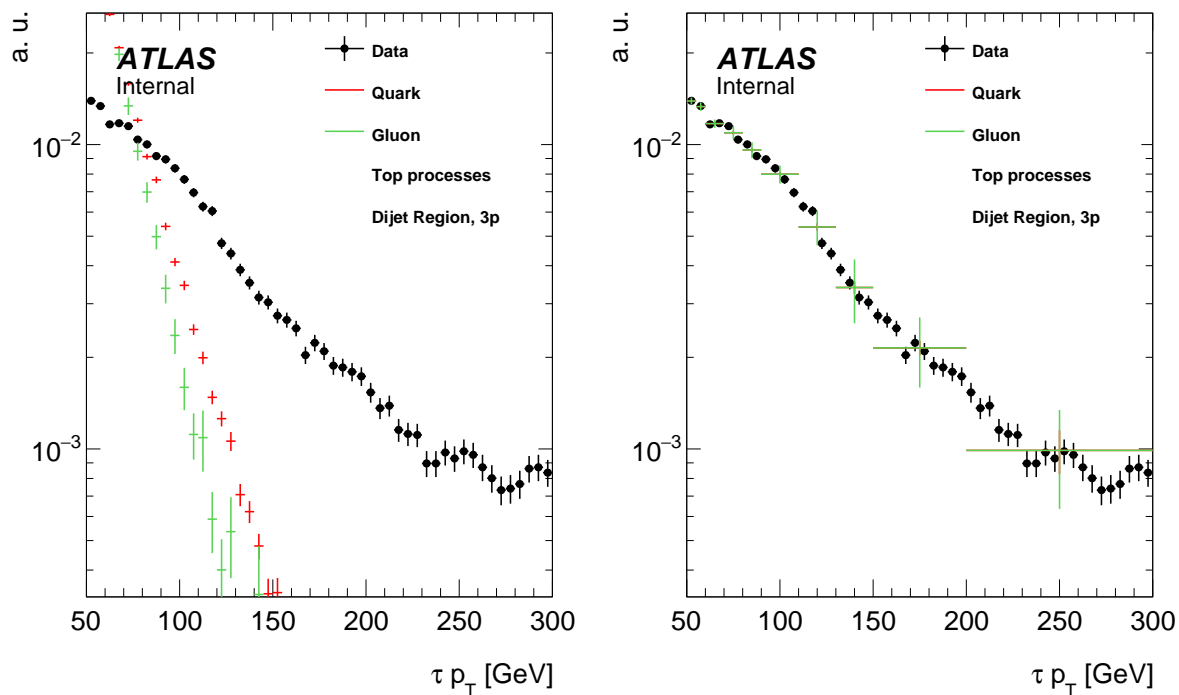
Figure 7.2: Normalised p_T spectrum of the quark and gluon templates from top processes before and after reweighting in the 3-prong dijet Region.

expected to be slightly shifted towards lower values of the jet width. This effect can be seen in Fig. 7.3. Another effect worth mentioning is that the p_T discrepancy between data and the quark and gluon templates becomes more prominent at higher values of p_T. For this reason, the shift of the jet width template is stronger in the $90 - 130$ GeV bin than in $50 - 70$ GeV bin.

7.1.3 Statistical Weighting of Jet Width Templates

As mentioned in Section 7.1, quark and gluon templates are extracted from Monte Carlo simulations for different production processes. The resulting templates are then added up to form universal quark and gluon templates with a higher total amount of generated events, resulting in lower statistical uncertainties. In Fig. 7.4 (left), the extracted quark templates in the dijet region for the $50 - 70$ GeV, 3-prong category can be seen. Here, pileup weight and Monte Carlo weights have been applied, as well as the previously discussed p_T reweighting. One can see that on average, the templates originating from $W \rightarrow \tau \nu$ processes have higher statistical uncertainties. In order to minimise the relative statistical uncertainties, the templates are each multiplied by a weight, so that the absolute error integrated over all bins is the same for every production process. The effect of this
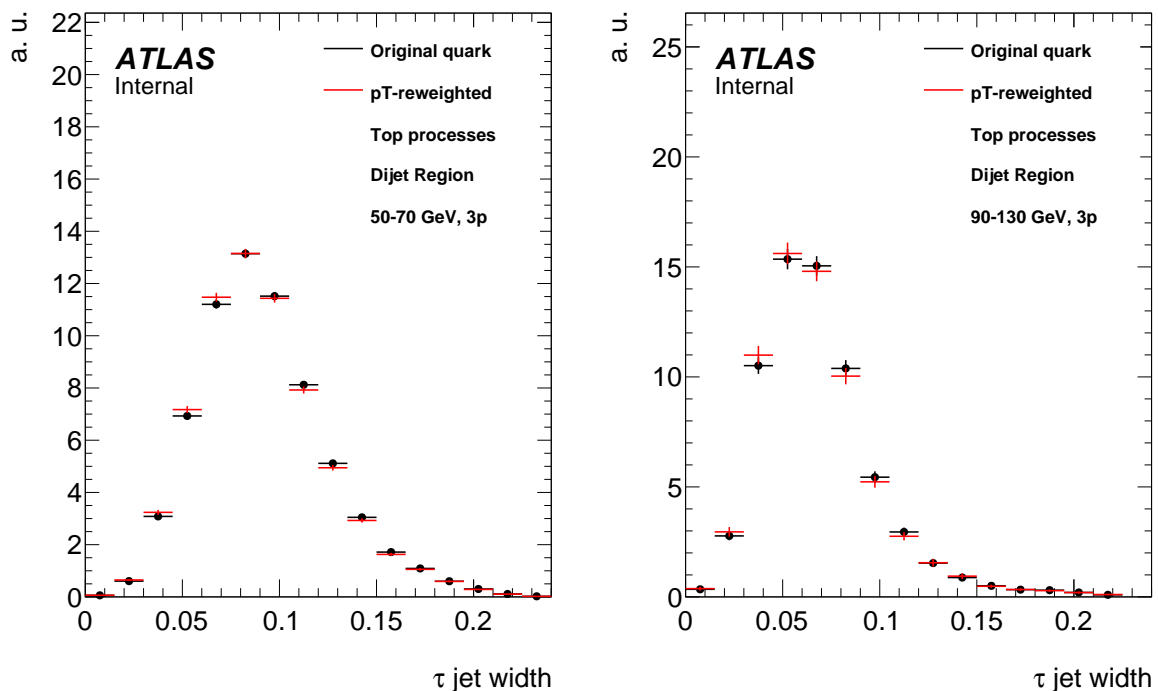
Figure 7.3: Normalised jet width distribution before and after p_T reweighting in the 3-prong dijet region for the $50 - 70$ GeV (left) and the $90 - 130$ GeV bin (right).

procedure is graphically displayed in Fig. 7.4 (right). The resulting templates are then added up to form a universal template with low relative statistical uncertainties. For the summation of templates from different processes not to introduce a bias, the templates must have compatible shapes. To check this, the normalised distributions are compared and a χ^2 test is conducted. As an example for this, Fig. 7.5 shows the comparison between the $W \to \tau\nu$ and $Z \to \tau\tau$ quark and gluon templates, separately. A full list with the results of all χ^2 tests can be seen in Table A.1. As an example, the template fits in the $50 - 70$ GeV, three-prong, opposite-sign category in the dijet region and in SCR are graphically displayed in Fig. 7.6. One can see that for the same p_T, sign, and prong bin, the quark fraction of the regions increases in the following order: dijet region, signal region, SCR.

7.1.4 Systematic uncertainties on the quark/gluon ratios

Smoothing of the Templates

In order to minimise the statistical uncertainties of the quark and gluon templates used for the template fits, a smoothing algorithm is applied to them [55]. It varies the content
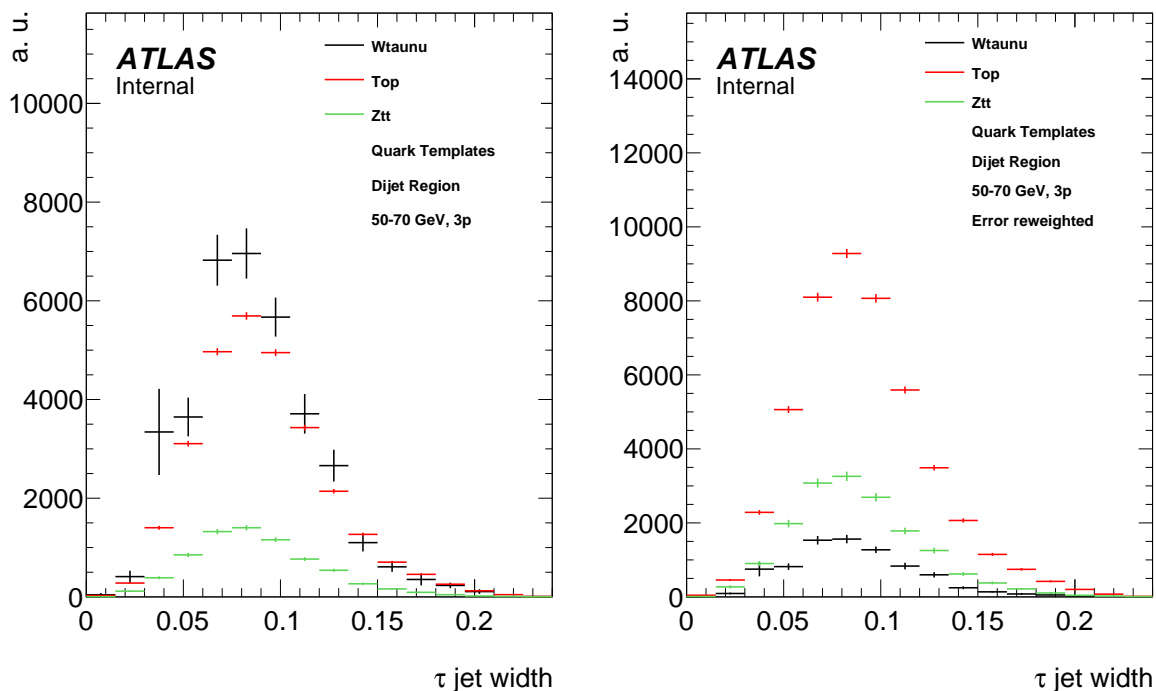
Figure 7.4: Quark templates in the dijet, 50-70 GeV, 3-prong category from different processes. On the left hand side, all previously mentioned weights are applied. On the right hand side, the templates were additionally statistically weighted.

of each bin within the statistical uncertainties to achieve a smoother distribution. To visualise this effect, a template with high relative statistical uncertainties (the one-prong gluon template for τ candidates with a transverse momentum between 90 and 130 GeV) is displayed in Fig. 7.7 (left) before and after applying the smoothing algorithm. The smoothing will not only affect statistical fluctuations in each bin, but also broaden the shape of the distribution. This effect can be seen in Fig. 7.7 (right). Here, the effects of the smoothing algorithm on a quark template for both one and three prong candidates over the entire p_T spectrum can be seen. This template with a lower statistical uncertainty was chosen to estimate the effects of the smoothing algorithm on the shape of jet width distribution. These effects will, however, introduce a systematic uncertainty to the template fits using any smoothened templates.

To estimate the systematic uncertainty on the template fit results caused by smoothing the templates, fits were conducted in regions with very low statistical uncertainties (prong and p_T inclusive) before and after smoothing the quark and gluon templates. The results can be seen in Table 7.1. The estimated quark fractions differ by 1.74 % in the opposite-sign case, and by 2.14 % in the same-sign case. So, the overall systematic uncertainty
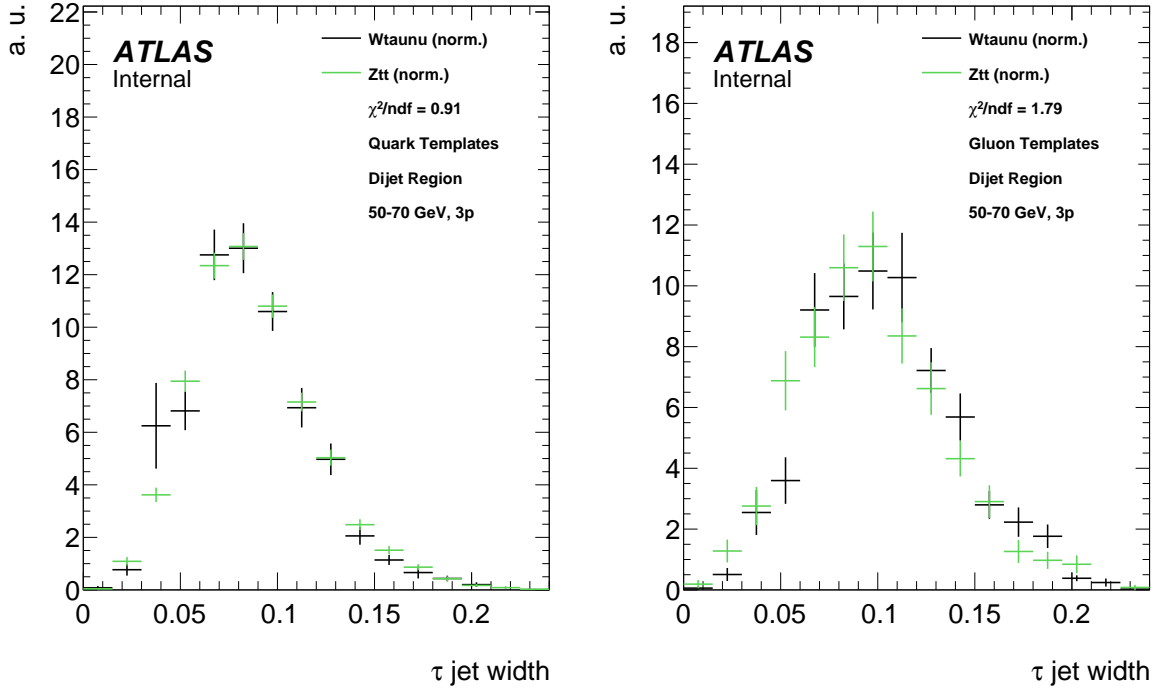
Figure 7.5: Normalised quark (left) and gluon (right) templates extracted from $W \to \tau\nu$ and $Z \to \tau\tau$ Monte Carlo in the dijet $50 - 70$ GeV, 3-prong category after p_T reweighting.
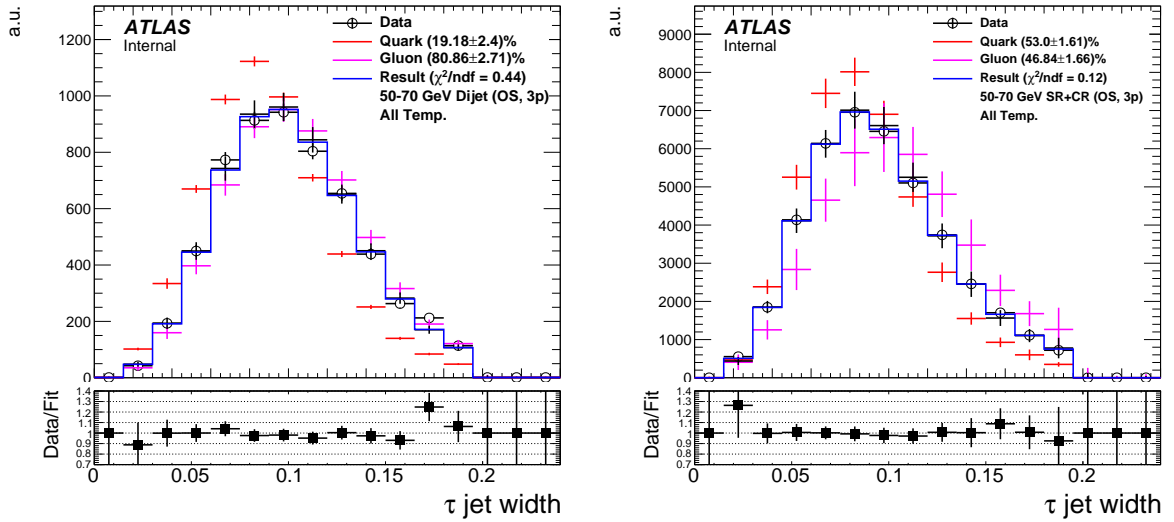
Figure 7.6: Results of the template fits in the dijet region (left) and SCR (right) for the $50 - 70$ GeV, opposite-sign, 3-prong category. In the ratio plot, statistical uncertainties as well as the uncertainty on the fractions are taken into account. The first and the last three bins were excluded before conducting the fit due to modelling issues.
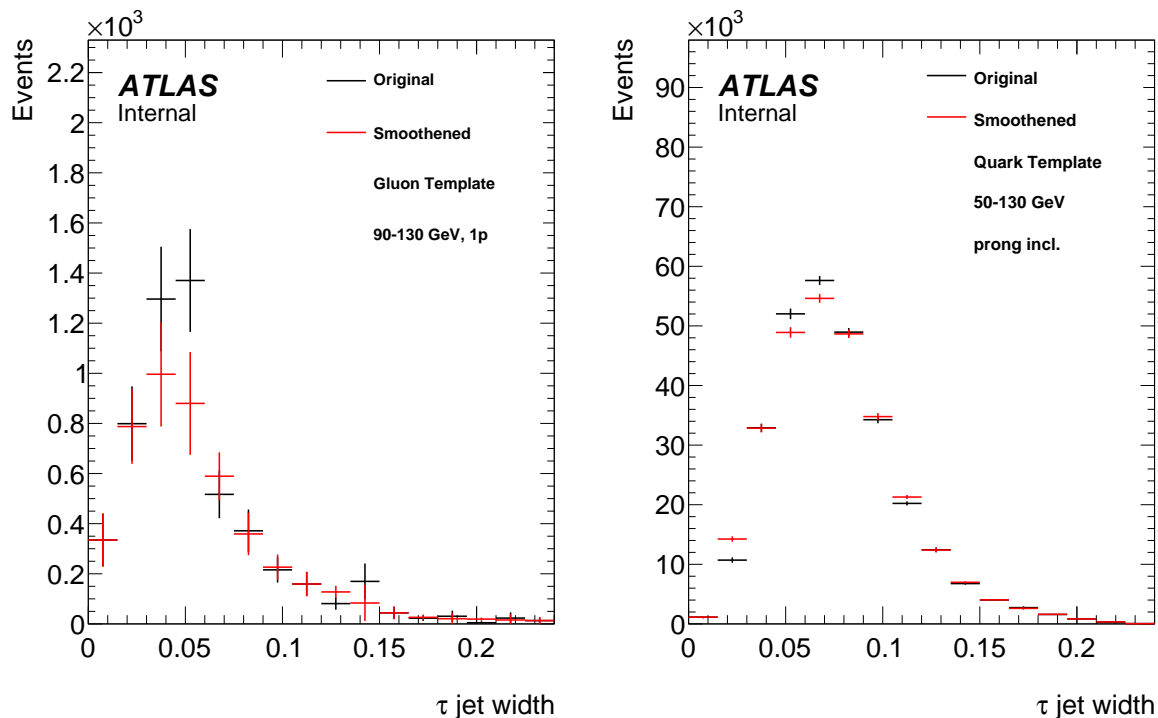
Figure 7.7: Effect of the smoothing algorithm on the $90 - 130$ GeV, 1p gluon template and a p_T and prong inclusive quark template.

on the results of the template fit caused by smoothing the quark and gluon templates is estimated to be

$$u_{\text{smooth}} = \frac{(1.74 + 2.14)\%}{2} = 1.94\%. \tag{7.2}$$

Effects of p_T reweighting

As mentioned in Section 7.1.2, every MC generated event in the jet width templates used for the template fits is multiplied by a weight, w_{p_T}, to make the p_T distribution of the

Category	Quarks [%]	Gluons [%]
Dijet+SCR, OS, 50-130 GeV, prong incl.	54.77 ± 0.62	45.21 ± 0.62
without smoothing	53.03 ± 0.53	46.95 ± 0.53
Dijet+SCR, SS, 50-130 GeV, prong incl.	47.7 ± 0.57	52.28 ± 0.57
without smoothing	45.56 ± 0.63	54.41 ± 0.64

Table 7.1: Results of 50-130 GeV, prong-inclusive fits used to estimate the effect of the smoothing algorithm on the results of the template fits.

MC templates and that in data compatible:

$$w_{p_T} = \frac{p_{T_{\text{data}}}}{p_{T_{\text{MC}}}}, \qquad (7.3)$$

where $p_{T_{\text{data}}}$ $(p_{T_{\text{MC}}})$ is the data (MC) yield of the bin in which the event lies. Of course, the error of the fits caused by the statistical uncertainties of the templates is covered. However, the p_T reweighting procedure introduces a new source of systematic uncertainty. According to Gaussian error propagation, the error of the p_T reweighting factor is

$$\sigma_{w_{p_T}} = \sqrt{\left(\frac{\partial w_{p_T}}{\partial p_{T_{\text{data}}}}\sigma_{p_{T_{\text{data}}}}\right)^2 + \left(\frac{w_{p_T}}{\partial p_{T_{\text{MC}}}}\sigma_{p_{T_{\text{MC}}}}\right)^2}$$

$$= \sqrt{\left(\frac{\sigma_{p_{T_{\text{data}}}}}{p_{T_{\text{MC}}}}\right)^2 + \left(\frac{p_{T_{\text{data}}}\sigma_{p_{T_{\text{MC}}}}}{p_{T_{\text{MC}}}^2}\right)^2}, \qquad (7.4)$$

where $\sigma_{p_{T_{\text{data}}}}$ $(\sigma_{p_{T_{\text{data}}}})$ is the uncertainty on the content of the corresponding bin. To evaluate the effect of this uncertainty on the template fits, upper (lower) limits on the quark and gluon templates are generated by varying w_{p_T} up (down) by $\sigma_{w_{p_T}}$ in each bin. The template fits are then repeated using the varied templates. The results of this procedure can be seen in Tables A.2, A.3, and A.4. This is, however, a very simplified method of estimating this uncertainty. Strictly speaking, a set of quark and gluon templates have to be Monte Carlo generated by randomly varying w_{p_T} within its uncertainties. For every combination of varied templates, the template fits should be repeated. The uncertainty on the quark and gluon fraction can then be estimated as the one sigma deviation from the mean value of the results of all the template fits.

Choice of Binning

Since the default binning [50,70,90,130] had been chosen more or less arbitrarily with the goal of having comparable statistical uncertainties in each bin, it must be ensured that the results do not depend strongly on the choice of the binning. Therefore, all template fits and fake factor calculations have been repeated with an alternative binning [50,65,80,130]. In Fig. 7.8, the quark fraction of each three-prong region is plotted vs p_T for the default and the alternative binning. Additionally, a linear function was fitted to the data points of each region in the alternative binning, respectively. To estimate the effect of the choice of the binning on the measured quark/gluon fraction, the distance between the data point of the default binning and the value of the corresponding linear fit at the same p_T are determined and can be seen in Table 7.2. For each region, the average value of that

Category	Δ(data, Fit)(60)	Δ(data, Fit)(80)	Δ(data, Fit)(110)	Δ(data, Fit)
Dijet, SS, 3p	6.56	1.32	5.37	4.41
SCR, SS, 3p	3.65	9.95	7.89	7.16
W+jet, SS, 3p	3.06	2.25	5.75	3.69
Dijet, OS, 3p	1.73	1.96	1.33	1.67
SCR, OS, 3p	0.19	2.53	3.24	1.99
W+jet, OS, 3p	2.24	2.61	4.08	2.98

Table 7.2: Distances between quark fractions of default binning and linear fit through quark fractions of alternative binning in absolute %. For each region, the average of these distances is assumed as a systematic uncertainty on the quark fraction.

distance is taken as a systematic uncertainty on the quark fraction.

Now that the template fits in every transverse momentum and number of tracks bin are conducted and the corresponding uncertainties are estimated, the correlation between the fake factor and the corresponding quark/gluon fraction of a sample is investigated in the next section.

7.2 Fake Factor Interpolation

The goal of this section is to determine the dependence of the fake factor on the quark/gluon fraction in a sample and use this relation to interpolate the fake factor in the signal region. To do so, both properties are measured in two separate regions with two different quark/gluon fractions. These are the dijet region which is dominated by gluons and the
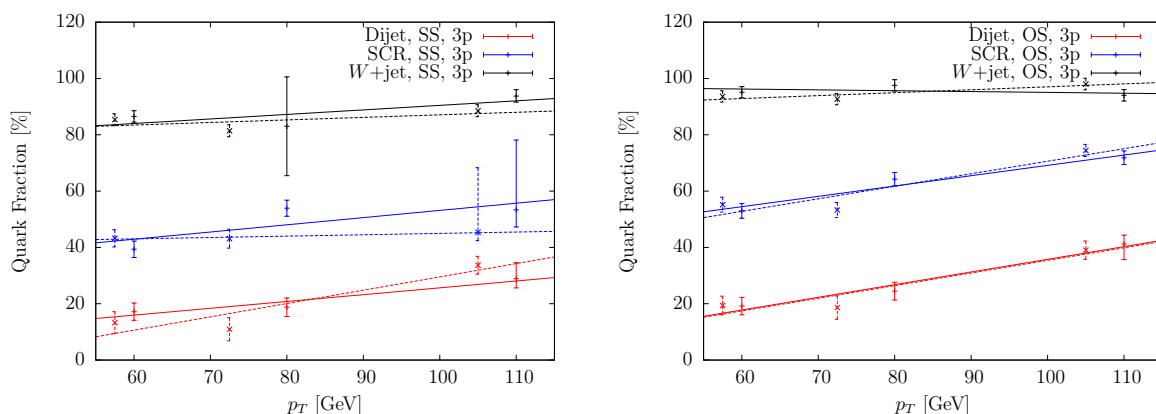
Figure 7.8: Quark fractions estimated via template fits versus p_T. The p_T value of each point in the graph corresponds to the mean value of the bin that the fit was conducted in. The results for the default and for the alternative binning can be seen as well as a linear fit through the data points of the alternative binning for each region.
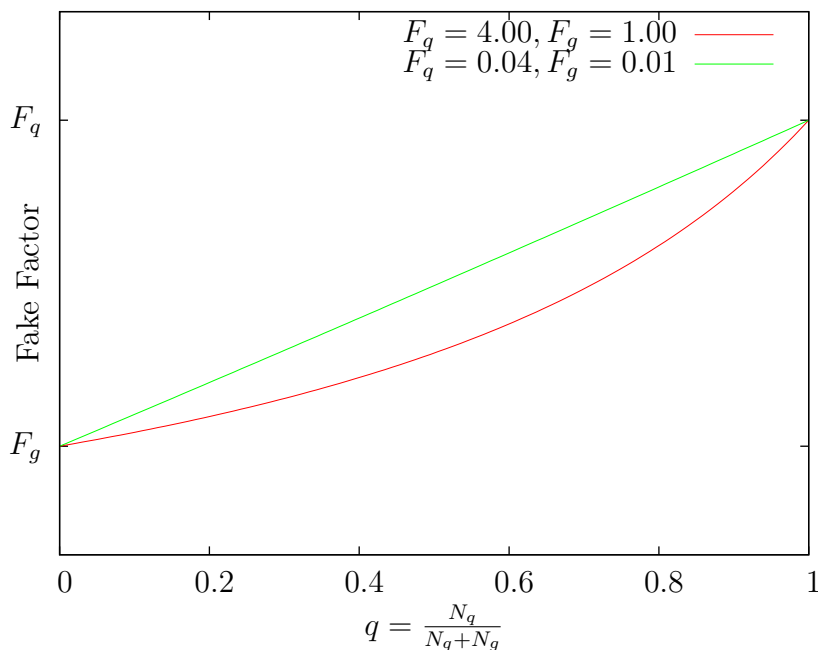
Figure 7.9: Fake factor's dependence on the fraction of quarks for two different assumed scenarios. The distributions shown have been derived analytically.

$W+$ jet region which is dominated by quarks. Before results are presented, some theoretical considerations must be taken into account.

Let p_q (p_g) be the probability of a quark (gluon) to pass the BDT-identification for τ leptons. Assuming the sample only consists of N_q quarks and N_g gluons with no other particles contributing ($N = N_q + N_g$), the fake factor, F, can be expressed as

$$F = \frac{\#(\text{quarks passing}) + \#(\text{gluons passing})}{\#(\text{quarks failing}) + \#(\text{gluons failing})} = \frac{N_q p_q + N_g p_g}{N_q(1 - p_1) + N_g(1 - p_g)}. \qquad (7.5)$$

Defining $q = \frac{N_q}{N_q + N_g}$ to be the fraction of quarks in the sample and using the fake factor for pure quarks $F_q = \frac{p_q}{1 - p_q} \Leftrightarrow p_q = \frac{F_q}{1 + F_q}$ (analogous for gluons), Eq. 7.5 can be expressed as

$$F = \frac{q(F_q - F_g) + F_g + F_q F_g}{q(F_g - F_q) + 1 + F_q}. \qquad (7.6)$$

The dependence of the overall fake factor on the quark fraction described by Eq. 7.6 is graphically displayed in Fig. 7.9 for two different scenarios.

In our case, the pure quark and gluon fake factors F_q and F_g are not known. Instead, the distribution displayed in Fig. 7.9 is reconstructed using two measured data points it passes through. Let $F_{1(2)}$ be the fake factor measured in the first (second) region and $q_{1(2)}$

the corresponding quark fraction. Inserting these values into Eq. 7.6 leads to a system with two equations. Solving this for F, one finds an expression for the Fake Factor F_3 in any region with a quark fraction q_3:

$$F_3(q_1, q_2, q_3, F_1, F_2) = \frac{q_3(F_1 - F_2) + q_1(F_1 F_2 + F_2) - q_2(F_1 F_2 + F_1)}{q_3(F_2 - F_1) + q_1(F_1 + 1) - q_2(F_2 + 1)}. \tag{7.7}$$

A more detailed version of the derivation of Eq. 7.7 can be found in the Appendix in Section A.1.1.

The uncertainty of the interpolated fake factor in Eq. 7.7 can be calculated using the Gaussian error propagation. After some lengthy calculations, one finds

$$\begin{aligned}
\sigma_{F_3} = &\{q_3(F_2 - F_1) + q_1(F_1 + 1) - q_2(F_2 + 1)\}^{-1} \\
&\times \{(F_1 + 1)^2(F_2 + 1)^2(F_2 - F_1)^2[(q_3 - q_2)^2\sigma_{q_1}^2 + (q_3 - q_1)^2\sigma_{q_2}^2 + (q_2 - q_1)^2\sigma_{q_3}^2] \\
&+ [q_1 - q_2]^2[(F_2 + 1)^4(q_3 - q_2)^2\sigma_{F_1}^2 + (F_1 + 1)^4(q_3 - q_1)^2\sigma_{F_2}^2]\}^{1/2}.
\end{aligned} \tag{7.8}$$

Since the quark fractions have asymmetric errors, some more considerations are needed. Under the assumption that $q_1 < q_2$ and $F_1 < F_2$ (which holds for any category), an upward mis-measurement of $q_{1,2}$ would result in a downward mis-measurement of F_3. The opposite counts for q_3 and $F_{1,2}$. Therefore, the downward mis-measurements of $q_{1,2}$ and the upward mis-measurements of q_3 and $F_{1,2}$ are used to calculate the upward mis-measurement of F_3 and vice versa.

The measured fake factors in the dijet and the W+jet region are graphically displayed in Fig. 7.10 for the three-prong case and in Fig. 7.11 for the one-prong case for same- and opposite-sign, separately. Alongside the measured fake factors, also the interpolated fake factors in the SCR can be seen, here. The same results can also be found in Table A.5.

To verify if the interpolated fake factors in the SCR are sensible, the fake factors are also calculated on data in this region. However, to prevent a potential signal contamination, this cross check is only done in the same-sign category. In Fig. 7.12, the interpolated fake factors and those calculated on data are shown in the same plot. It is displayed for the three- and one-prong case, separately. The measured and interpolated fake factors are compatible within uncertainties, which can be seen as a proof that interpolating the fake factors according to the quark/gluon ratios of the respective regions is a valid method. However, the measured fake factors in SCR are also compatible with the measured fake factors in the dijet region (same-sign) which qualifies this statement. As it can be seen in Fig. 7.10 (left), a big difference between the fake factors in the dijet region and those in SCR is not expected for the same-sign case which makes it difficult to verify this method.
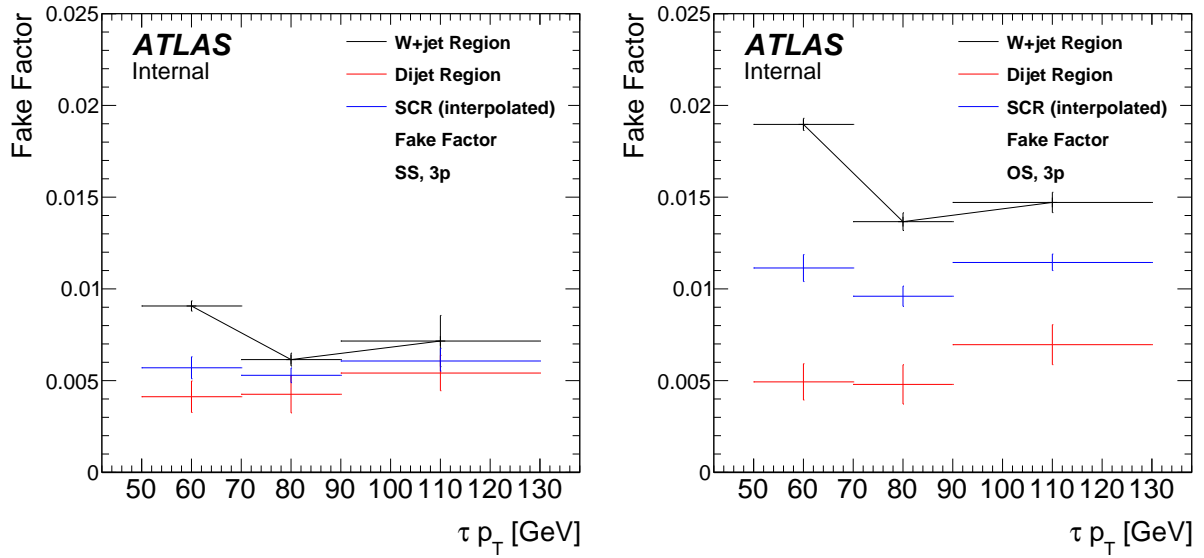
Figure 7.10: Fake factors in the W+jet Region and the dijet Region (3-prong) for same-(left) and opposite-sign (right) with all statistical and systematic uncertainties.
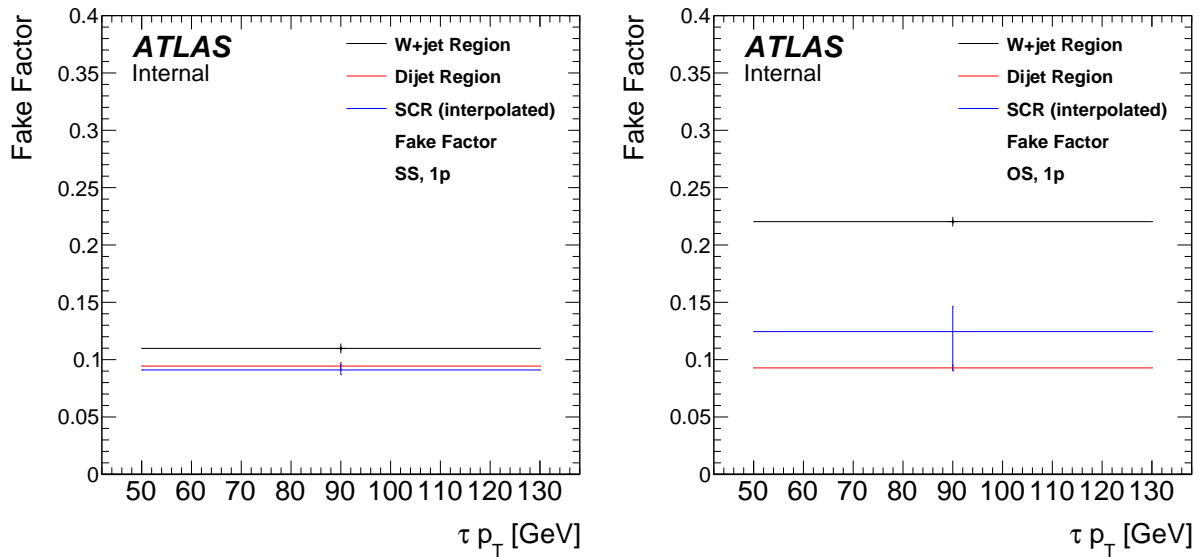
Figure 7.11: Fake factors in the W+jet Region and the dijet Region (1-prong) with all statistical and systematic uncertainties.
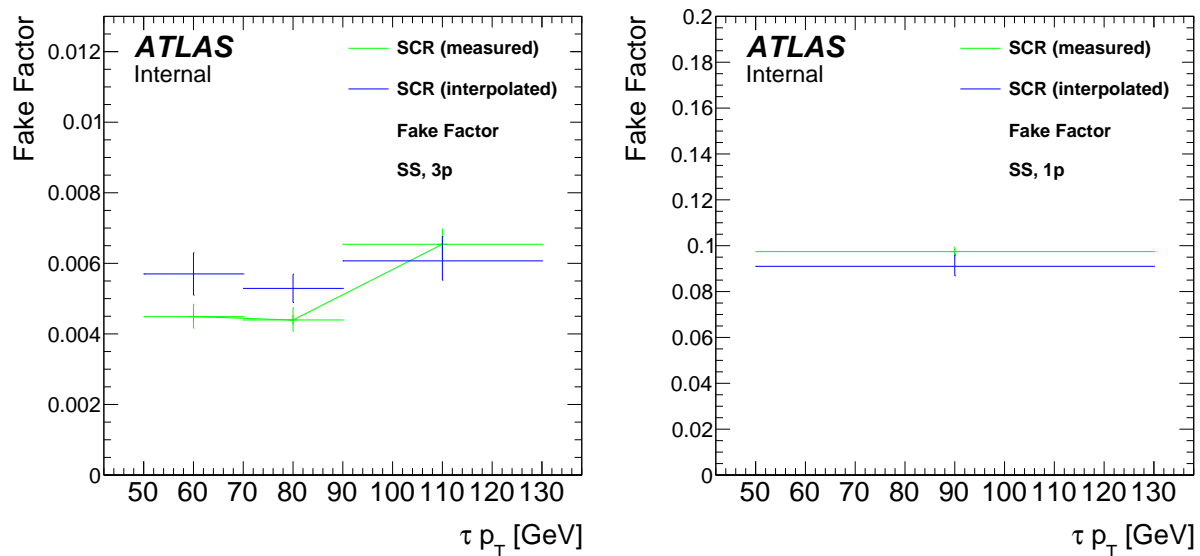
Figure 7.12: Measured and interpolated fake factors in same-sign SCR for the three-prong (left) and one-prong category (right).

It does, however, have a big impact in the opposite-sign region, and therefore on the background estimate in the signal region.

Again, according to Section 5.3, the analysis uses the fake factors that are evaluated in the dijet region to estimate the amount of falsely identified $\tau_{\text{had-vis}}$ candidates in the signal region. The template fits show, however, that the quark/gluon fractions in those two regions are not compatible. Therefore, the fake factors need to be scaled according to the interpolation method discussed in Section 7.2. From Figures 7.10 and 7.11, it is apparent that this correction is not negligible and has a significant impact on the background estimate of the QCD multijet background which makes up roughly 78% of the total background in the b-veto signal region.

8 Signal Studies

After investigating the background estimate quite intensively, the focus of this chapter lies on studying different hypothetical signals. To do this, Monte Carlo generated samples of heavy Higgs bosons produced in gluon-gluon fusion and b-associated production are used. In Fig. 8.1, the distribution of the final discriminant, the total transverse mass, is shown in the b-veto category. Apart from data and background yields, the distribution that a potential heavy Higgs boson would exhibit according to the hMSSM model is also displayed for two different assumed parameter combinations:

- $m_A = 500$ GeV and $\tan\beta = 20$

- $m_A = 1000$ GeV and $\tan\beta = 50$.

The same distributions in the b-tag category are displayed in Fig. 8.2. It is apparent that the distribution of a signal drops at the assumed mass of the heavy Higgs boson. This behaviour is expected, since the transverse mass peaks in the case that the two τ leptons are emitted back-to-back at almost the mass of the mother particle. For any other angle between the two τ leptons, the total transverse mass is lower, reaching zero in the case that both particles fly in the same direction. The influence of the choice of $\tan\beta$ is restricted to the normalisation of the distribution of a signal. Since $\tan\beta$ only affects the production cross section of a heavy Higgs boson and the branching ratio of the decay into down type fermions such as the τ lepton, a different value of $\tan\beta$ negligibly affects the shape of the signal.

In Table A.7 and Table A.8, a detailed cutflow table is shown for a signal from a heavy Higgs boson with different assumed masses produced in gluon-gluon-fusion and b-associated production, respectively. For all mass hypotheses, the numbers were derived assuming an integrated luminosity of 36.1 fb^{-1} and a conventional signal production cross section of 1 pb, which lies within the range of values predicted by the MSSM as it can be seen in Fig. 3.4.

Using these tables, it is easy to determine what fraction of initial signal events are left after
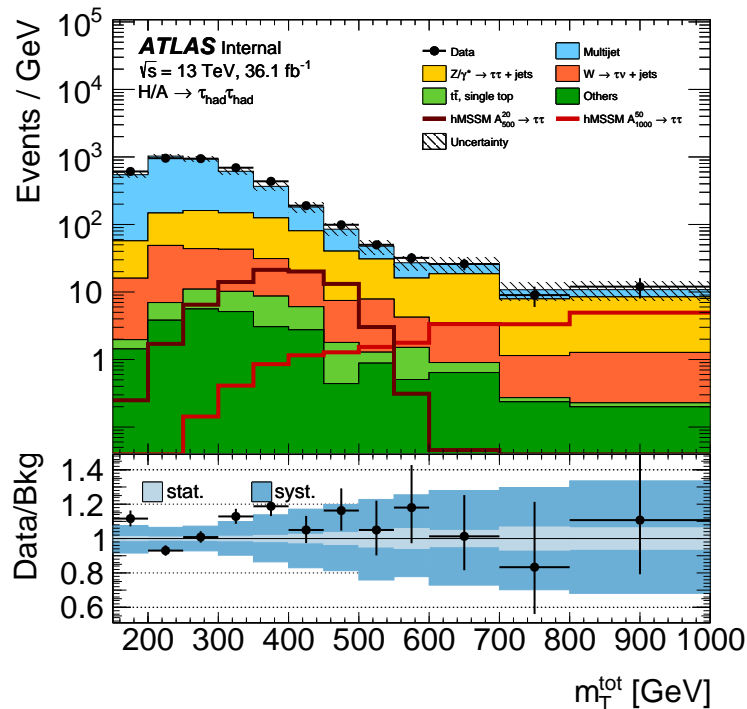
Figure 8.1: Total transverse mass distribution in the *b*-veto signal region. Two hypothetical signals in the hMSSM scenario for $(m_{A/H} = 500$ GeV, $\tan\beta=20)$ and $(m_{A/H} = 1000$ GeV, $\tan\beta=50)$ are also shown.

applying all selection criteria, which is known as the product of efficiency and acceptance:

$$\varepsilon \times \mathcal{A} = \frac{\text{event yield after all selections applied}}{\text{initial number of events}}, \tag{8.1}$$

where the initial number of events can simply be calculated as $\sigma \times \int \mathcal{L} \, \mathrm{d}t$. The acceptance, $\mathcal{A}$, is defined as the fraction of events that can be potentially detected purely in terms of the positions and directions of the particles related to the fiducial volume of the detector. The efficiency, ε, is the fraction of events actually being detected and passing the selection criteria, under the assumption that all particles pass the fiducial volume of the detector. In Fig. 8.3, $\varepsilon \times \mathcal{A}$ in the *b*-veto category is shown for different assumed masses of a heavy Higgs boson produced in gluon-gluon-fusion and *b*-associated production, separately. The same distributions in the *b*-tag category are shown in Fig. 8.4. Although the total yields depend on the assumed cross section - and thereby implicitly on the choice of $\tan\beta$, $\varepsilon \times \mathcal{A}$ only depends on the assumed mass of the heavy Higgs. This is the case because the effect simply cancels out in the fraction, since $\tan\beta$ does not have an impact on the kinematic distributions of the signal.

As expected, in the *b*-veto category, $\varepsilon \times \mathcal{A}$ is higher for a heavy Higgs produced in gluon-
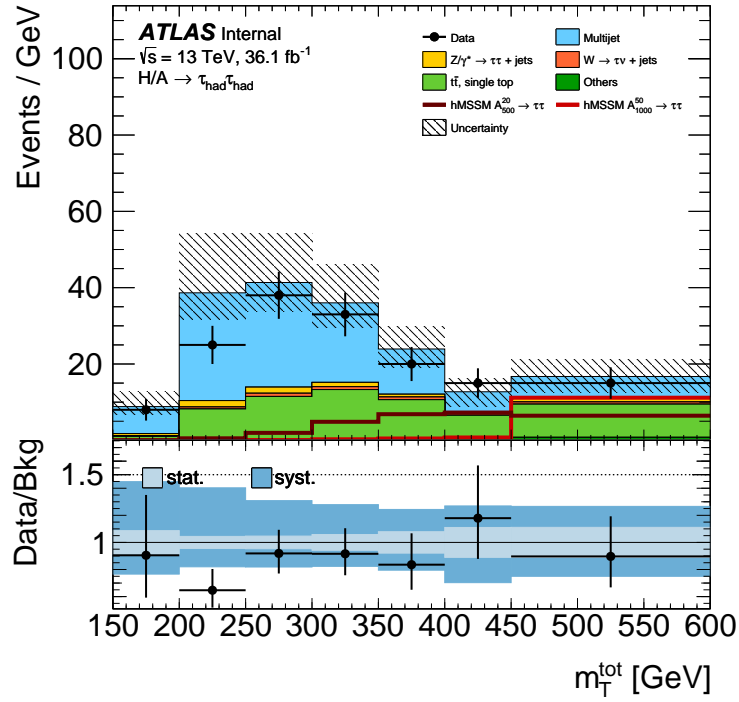
Figure 8.2: Total transverse mass distribution in the *b*-veto signal region. Two hypothetical signals in the hMSSM scenario for $(m_{A/H} = 500$ GeV, $\tan\beta=20)$ and $(m_{A/H} = 1000$ GeV, $\tan\beta=50)$ are also shown.

gluon-fusion than for the *b*-associated production. The opposite holds for the *b*-tag category, as it was foreseen by the analysis. Overall, $\varepsilon \times \mathcal{A}$ is higher in the *b*-veto category. Since the transverse momenta of the (sub-) leading $\tau_{\text{had-vis}}$ candidate is required to be greater than (65) 85 GeV, $\varepsilon \times \mathcal{A}$ is approximately zero at $m_A = 125$ GeV, then rises quickly and reaches its maximum around $m_A = 800$ GeV in the *b*-veto category and around $m_A = 1000$ GeV in the *b*-tag category. This suppresses any background contamination from the SM like Higgs boson with $m_h = 125$ GeV and makes the analysis sensitive to potential BSM Higgs bosons with very high masses.

The case where one τ lepton decays leptonically and one decays hadronically is considered in a separate analysis. This decay channel is more sensitive to slightly lower masses than the fully hadronic one. The combined results of both decay channels have been published recently [31].
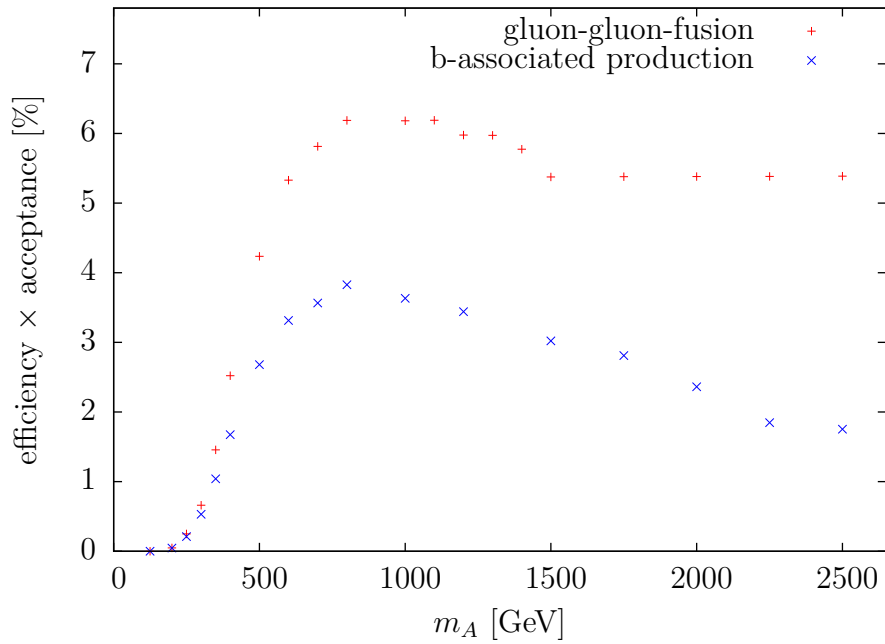
Figure 8.3: Efficiency × acceptance versus assumed m_A in the b-veto category for A/H produced in gluon-gluon-fusion and b-associated production.
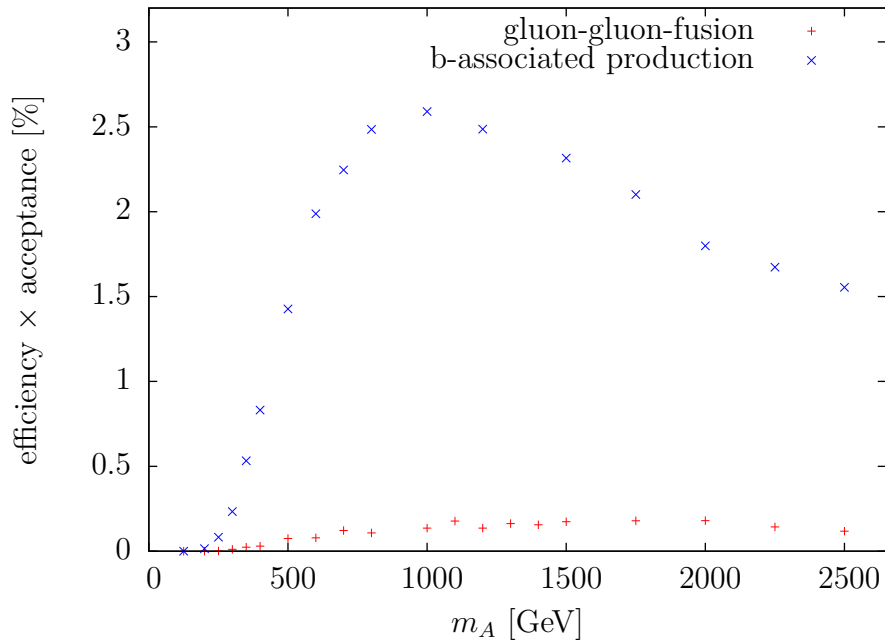
Figure 8.4: Efficiency × acceptance versus assumed m_A in the b-tag category for A/H produced in gluon-gluon-fusion and b-associated production.

9 Conclusion

Using 36.1 fb^{-1} of data taken at $\sqrt{s} = 13$ TeV with the ATLAS detector, a search for heavy Higgs bosons was conducted.

In this thesis, the fake rate technique used to estimate the background contribution from $W \to \tau\nu$ and top processes has been revisited and improved. The discrepancy between fake rates evaluated on Monte Carlo generated events and in data has been understood with the help of template fits that were used to estimate the quark/gluon ratio in a data sample. The subtraction of truth-matched τ leptons before evaluating the fake rates on data (Section 6.2) has been implemented into the existing analysis framework, improving the background estimation that was used for the latest results. The proposed correction of the fake rate evaluated on data in the W+jet region by the ratio of the fake rates evaluated on Monte Carlo generated events in the signal and W+jet region (Section 6.4) was deemed to be unnecessary due to a negligible effect compared to the uncertainties. However, it might prove useful for future analysis as the integrated luminosity is rising.

The fake factor technique used to estimate the background contribution from QCD multijet processes has also been revisited and improved. Here, the dependence of the fake factor on the quark/gluon ratio of a sample was investigated. The quark/gluon ratios in a data sample were estimated with the help of sophisticated template fits binned in the number of prongs and the transverse momentum of the $\tau_{\text{had-vis}}$ candidate. Evaluating the fake factors in two regions with known quark/gluon ratios allowed the interpolation of the fake factors to the signal region without the problem of a possible signal contamination (Section 7.2). The proposed correction of the fake factors according to the difference in quark/gluon ratios was found to be consistent in a cross check in the same-sign control region. It is expected to also improve the background estimate in the opposite-sign signal region significantly.

The signal studies gave interesting insight on $\varepsilon \times \mathcal{A}$ for heavy Higgs bosons with different assumed values of m_A.

The analysis team published their results in September 2017 [31], not finding any excess over the SM background. However, new limits were set and a large part of the $m_A - \tan\beta$ parameter space in the hMSSM was excluded at the 95% confidence level.

In the future, the ATLAS detector will deliver more data. Especially after the upgrade towards the High Luminosity LHC (HL-LHC), which is planned to be installed in 2025, the instantaneous luminosity will increase significantly [56]. The additional data will also be used for searches for heavy Higgs bosons. Perhaps, an excess over the SM background will be discovered, proving physics beyond the Standard Model. If not, bigger parts of the parameter space of the MSSM will be excluded. In any case, exciting times lie ahead.

A Appendix

A.1 Fake Factor Studies

Category	χ^2/ndf ($W \to \tau\nu$, top)		χ^2/ndf ($W \to \tau\nu$, $Z \to \tau\tau$)	
	Quarks	Gluons	Quarks	Gluons
Dijet, SS, 50-70 GeV, 3p	2.79	1.91	0.91	1.8
Dijet, SS, 70-90 GeV, 3p	2.11	1.42	0.63	3.45
Dijet, SS, 90-130 GeV, 3p	1.2	1.4	0.84	1.6
Dijet, SS, 50-130 GeV, 1p	2.32	5.9	0.58	1.56
SCR, SS, 50-70 GeV, 3p	0.9	1.46	0.62	1.29
SCR, SS, 70-90 GeV, 3p	1.13	1.94	0.89	1.69
SCR, SS, 90-130 GeV, 3p	1.3	0.99	1.15	1.03
SCR, SS, 50-130 GeV, 1p	2.84	2.49	1.3	1.43
Dijet, OS, 50-70 GeV, 3p	2.8	1.89	0.91	1.79
Dijet, OS, 70-90 GeV, 3p	2.1	1.43	0.64	3.46
Dijet, OS, 90-130 GeV, 3p	1.2	1.4	0.84	1.6
Dijet, OS, 50-130 GeV, 1p	2.34	5.89	0.59	1.54
SCR, OS, 50-70 GeV, 3p	2.17	0.97	1.61	0.98
SCR, OS, 70-90 GeV, 3p	3.24	1.63	1.75	2.11
SCR, OS, 90-130 GeV, 3p	2.35	1.22	1.48	1.74
SCR, OS, 50-130 GeV, 1p	1.4	1.50	0.77	1.66

Table A.1: Results of χ^2 tests between jet width templates from different production processes.

Category	Quarks [%]	Gluons [%]	Unc. due to weights
Dijet, SS, 50-70 GeV, 3p	(17.19 ± 2.37)	(82.87 ± 2.72)	$+0.08 - 0.09$
Dijet, SS, 70-90 GeV, 3p	(18.76 ± 2.64)	(81.23 ± 2.81)	$+0.23 - 0.02$
Dijet, SS, 90-130 GeV, 3p	(28.89 ± 2.63)	(71.17 ± 2.66)	$+4.62 - 0.0$
Dijet, SS, 50-130 GeV, 1p	(40.46 ± 3.17)	(59.45 ± 3.41)	$+15.62 - 0.0$
Dijet, OS, 50-70 GeV, 3p	(19.18 ± 2.4)	(80.86 ± 2.71)	$+0.1 - 0.1$
Dijet, OS, 70-90 GeV, 3p	(24.46 ± 2.48)	(75.54 ± 2.81)	$+0.41 - 0.03$
Dijet, OS, 90-130 GeV, 3p	(41.21 ± 2.53)	(58.81 ± 2.55)	$+0.0 - 4.55$
Dijet, OS, 50-130 GeV, 1p	(32.03 ± 0.3)	(67.83 ± 3.4)	$20.07 - 0.0$
Dijet, SS, 50-65 GeV, 3p	(13.29 ± 3.35)	(86.7 ± 3.59)	$+0.02 - 0.01$
Dijet, SS, 65-80 GeV, 3p	(10.92 ± 3.59)	(89.07 ± 3.82)	$+0.14 - 0.14$
Dijet, SS, 80-130 GeV, 3p	(33.67 ± 2.43)	(66.33 ± 2.47)	$+0.39 - 0.47$
Dijet, OS, 50-65 GeV, 3p	(19.37 ± 2.68)	(80.59 ± 3.07)	$+0.02 - 0.02$
Dijet, OS, 65-80 GeV, 3p	(18.62 ± 3.66)	(81.37 ± 3.86)	$+0.2 - 0.2$
Dijet, OS, 80-130 GeV, 3p	(39.04 ± 2.56)	(60.96 ± 2.59)	$+0.29 - 0.52$

Table A.2: Results of template fits in the dijet region. The values in the last column were estimated by varying the p_T weights of the templates within their uncertainties.

Category	Quarks [%]	Gluons [%]	Unc. due to weights
SCR, SS, 50-70 GeV, 3p	(39.37 ± 2.12)	(60.69 ± 2.24)	$+0.35 - 0.47$
SCR, SS, 70-90 GeV, 3p	(53.94 ± 2.06)	(46.09 ± 2.08)	$+0.00 - 0.26$
SCR, SS, 90-130 GeV, 3p	(53.34 ± 2.28)	(46.19 ± 2.23)	$+24.64 - 5.29$
SCR, SS, 50-130 GeV, 1p	(30.8 ± 3.0)	(68.81 ± 3.06)	$+25.02 - 0.0$
SCR, OS, 50-70 GeV, 3p	(53.0 ± 1.61)	(46.84 ± 1.66)	$+0.45 - 0.65$
SCR, OS, 70-90 GeV, 3p	(64.25 ± 1.33)	(35.5 ± 1.32)	$+0.1 - 0.2$
SCR, OS, 90-130 GeV, 3p	(71.83 ± 1.2)	(27.53 ± 1.13)	$+0.89 - 0.62$
SCR, OS, 50-130 GeV, 1p	(48.66 ± 2.65)	(50.24 ± 2.68)	$+14.65 - 17.85$
SCR, SS, 50-65 GeV, 3p	(43.25 ± 2.31)	(56.43 ± 2.4)	$+0.27 - 0.45$
SCR, SS, 65-80 GeV, 3p	(43.12 ± 2.72)	(55.85 ± 2.75)	$+0.12 - 0.14$
SCR, SS, 80-130 GeV, 3p	(45.37 ± 2.26)	(54.07 ± 2.28)	$+22.74 - 0.03$
SCR, OS, 50-65 GeV, 3p	(55.18 ± 1.73)	(44.8 ± 1.75)	$+0.49 - 0.0$
SCR, OS, 65-80 GeV, 3p	(53.29 ± 1.8)	(46.09 ± 1.83)	$+0.06 - 0.05$
SCR, OS, 80-130 GeV, 3p	(74.45 ± 0.87)	(25.42 ± 0.79)	$+0.05 - 0.16$

Table A.3: Results of template fits in the dijet region. The values in the last column were estimated by varying the p_T weights of the templates within their uncertainties.

Category	Quarks [%]	Gluons [%]	Unc. due to weights
W+jet, SS, 50-70 GeV, 3p.	(86.53 ± 0.51)	(13.47 ± 0.46)	$+0.09 - 0.08$
W+jet, SS, 70-90 GeV, 3p	(83.03 ± 17.43)	(17.43 ± 18.74)	$+0.17 - 0.0$
W+jet, SS, 90-130 GeV, 3p	(93.74 ± 0.87)	(6.23 ± 0.73)	$+0.73 - 0.$
W+jet, SS, 50-130 GeV, 1p	(83.63 ± 0.9)	(16.37 ± 0.83)	$+0.92 - 0.66$
W+jet, OS, 50-70 GeV, 3p	(95.11 ± 0.34)	(4.92 ± 0.28)	$+0.03 - 0.0$
W+jet, OS, 70-90 GeV, 3p	(97.56 ± 0.49)	(2.59 ± 0.38)	$+0.0 - 0.02$
W+jet, OS, 90-130 GeV, 3p	(94.0 ± 0.5)	(6.93 ± 0.39)	$+0.09 - 0.15$
W+jet, OS, 50-130 GeV, 1p	(93.81 ± 0.47)	(7.28 ± 0.37)	$+0.7 - 0.66$
W+jet, SS, 50-65 GeV, 3p	(85.41 ± 0.57)	(14.58 ± 0.51)	$+0.04 - 0.17$
W+jet, SS, 65-80 GeV, 3p	(81.43 ± 0.8)	(18.6 ± 0.72)	$+0.02 - 0.01$
W+jet, SS, 80-130 GeV, 3p	$(88.54 \pm 0.0.69)$	(11.46 ± 0.61)	$+0.41 - 0.33$
W+jet, OS, 50-65 GeV, 3p	(93.63 ± 0.34)	(6.37 ± 0.28)	$+0.06 - 0.0$
W+jet, OS, 65-80 GeV, 3p	(92.67 ± 0.45)	(7.33 ± 0.36)	$+0.0 - 0.02$
W+jet, OS, 80-130 GeV, 3p	(98.03 ± 0.47)	(2.68 ± 0.35)	$+0.26 - 0.25$

Table A.4: Results of template fits in the dijet region. The values in the last column were estimated by varying the p_T weights of the templates within their uncertainties.

Category	FF in Dijet Region	FF in W+jet Region	FF in SCR
SS, 50-70 GeV, 3p	(0.00412 ± 0.00086)	(0.00907 ± 0.00028)	$(0.00570^{+0.00060}_{-0.00060})$
SS, 70-90 GeV, 3p	(0.00426 ± 0.00101)	(0.00615 ± 0.00035)	$(0.00529^{+0.00040}_{-0.00040})$
SS, 90-130 GeV, 3p	(0.00541 ± 0.00096)	(0.00716 ± 0.00139)	$(0.00607^{+0.00069}_{-0.00055})$
SS, 50-130 GeV, 1p	(0.0944 ± 0.00317)	(0.10981 ± 0.00121)	$(0.09101^{+0.00494}_{-0.00413})$
OS, 50-70 GeV, 3p	(0.00493 ± 0.00099)	(0.01897 ± 0.00033)	$(0.01114^{+0.00073}_{-0.00074})$
OS, 70-90 GeV, 3p	(0.00479 ± 0.00107)	(0.01366 ± 0.00048)	$(0.00960^{+0.00055}_{-0.00055})$
OS, 90-130 GeV, 3p	(0.00696 ± 0.00109)	(0.01471 ± 0.00055)	$(0.01144^{+0.00046}_{-0.00044})$
OS, 50-130 GeV, 1p	(0.09281 ± 0.0027)	(0.22036 ± 0.0012)	$(0.12445^{+0.02223}_{-0.03393})$

Table A.5: Measured fake factors in dijet and W+jet region with corresponding interpolated fake factor in SCR for each category.

A.1.1 The Dependence of the Fake Factor on the Quark Fraction

The goal of this section is a more detailed derivation of the dependence of the fake factor on the quark fraction, in particular Eq. 7.7 and the corresponding error. Let p_q (p_g) be the probability of a quark (gluon) to pass the BDT-identification. Assuming the sample only consists of N_q quarks and N_g gluons with no other particles contributing $(N = N_q + N_g)$, the fake factor, F, can be expressed as

$$F = \frac{\#(\text{quarks passing}) + \#(\text{gluons passing})}{\#(\text{quarks failing}) + \#(\text{gluons failing})} = \frac{N_q p_q + N_g p_g}{N_q(1 - p_1) + N_g(1 - p_g)}. \qquad \text{(A.1)}$$

A Appendix

Defining $q = \frac{N_q}{N_q + N_g}$ to be the fraction of quarks in the sample, Eq. A.1 can be written as

$$F = \frac{q(p_q - p_g) + p_g}{q(p_g - p_q) - p_g + 1}.$$ (A.2)

Be $F_{1(2)}$ the fake factor measured in the first (second) region and $q_{1(2)}$ the corresponding quark fraction. Inserting these values into Eq. A.2 leads to a system with the following two equations:

$$\begin{aligned} p_g &= \frac{q_1 p_q F_1 - F_1 + q_1 p_q}{q_1 F_1 - F_1 + q_1 - 1} \\ &= \frac{q_1 p_q (F_1 + 1) - F_1}{(q_1 - 1)(F_1 + 1)} \end{aligned}$$ (A.3)

$$\begin{aligned} p_q &= \frac{p_g(q_2 F_2 - F_2 + q_2 - 1) + F_2}{q_2 F_2 + q_2} \\ &= \frac{p_g(q_2 - 1)(F_2 + 1) + F_2}{q_2(F_2 + 1)} \end{aligned}$$ (A.4)

Solving this, one finds

$$p_q = \frac{q_1(F_1 F_2 + F_2) - q_2(F_1 F_2 + F_1) + F_1 - F_2}{q_1(F_1 F_2 + F_1 + F_2 + 1) - q_2(F_1 F_2 + F_1 + F_2 + 1)}$$ (A.5)

$$p_g = \frac{q_1(F_1 F_2 + F_2) - q_2(F_1 F_2 + F_1)}{(q_1 - q_2)(F_1 + 1)(F_2 + 1)}.$$ (A.6)

Inserting Eq. A.5 and Eq. A.7 into Eq. A.2 then leads to the fake factor F_3 in any region with the quark fraction q_3 in dependence of the measured values $F_{1,2}$ and $q_{1,2}$:

$$F_3(q_1, q_2, q_3, F_1, F_2) = \frac{q_3(F_1 - F_2) + q_1(F_1 F_2 + F_2) - q_2(F_1 F_2 + F_1)}{q_3(F_2 - F_1) + q_1(F_1 + 1) - q_2(F_2 + 1)}.$$ (A.7)

The uncertainty of the interpolated fake factor in Eq. A.7 can be calculated using the Gaussian error propagation:

$$\sigma_{F_3} = \sqrt{\left(\frac{\partial F_3}{\partial q_1}\sigma_{q_1}\right)^2 + \left(\frac{\partial F_3}{\partial q_2}\sigma_{q_2}\right)^2 + \left(\frac{\partial F_3}{\partial q_3}\sigma_{q_3}\right)^2 + \left(\frac{\partial F_3}{\partial F_1}\sigma_{F_1}\right)^2 + \left(\frac{\partial F_3}{\partial F_2}\sigma_{F_2}\right)^2}.$$ (A.8)

The derivatives that appear in Eq. A.8 are listed below.

$$\frac{\partial F_3}{\partial q_1} = \frac{(F_1 + 1)(F_2 + 1)(F_2 - F_1)(q_3 - q_2)}{[q_3(F_2 - F_1) + q_1(F_1 + 1) - q_2(F_2 + 1)]^2} \tag{A.9}$$

$$\frac{\partial F_3}{\partial q_2} = \frac{(F_1 + 1)(F_2 + 1)(F_1 - F_2)(q_3 - q_1)}{[q_3(F_2 - F_1) + q_1(F_1 + 1) - q_2(F_2 + 1)]^2} \tag{A.10}$$

$$\frac{\partial F_3}{\partial q_3} = \frac{(F_1 + 1)(F_2 + 1)(F_2 - F_1)(q_2 - q_1)}{[q_3(F_2 - F_1) + q_1(F_1 + 1) - q_2(F_2 + 1)]^2} \tag{A.11}$$

$$\frac{\partial F_3}{\partial F_1} = \frac{(F_2 + 1)^2(q_1 - q_2)(q_3 - q_2)}{[q_3(F_2 - F_1) + q_1(F_1 + 1) - q_2(F_2 + 1)]^2} \tag{A.12}$$

$$\frac{\partial F_3}{\partial F_2} = \frac{(F_1 + 1)^2(q_2 - q_1)(q_3 - q_1)}{[q_3(F_2 - F_1) + q_1(F_1 + 1) - q_2(F_2 + 1)]^2} \tag{A.13}$$

Inserting these into Eq. A.7, one finally finds

$$\sigma_{F_3} = \{q_3(F_2 - F_1) + q_1(F_1 + 1) - q_2(F_2 + 1)\}^{-1} \tag{A.14}$$
$$\times \{(F_1 + 1)^2(F_2 + 1)^2(F_2 - F_1)^2[(q_3 - q_2)^2\sigma_{q_1}^2 + (q_3 - q_1)^2\sigma_{q_2}^2 + (q_2 - q_1)^2\sigma_{q_3}^2]$$
$$+ [q_1 - q_2]^2[(F_2 + 1)^4(q_3 - q_2)^2\sigma_{F_1}^2 + (F_1 + 1)^4(q_3 - q_1)^2\sigma_{F_2}^2]\}^{1/2}.$$

A.2 Cutflow Tables

BVETO

Cut	Data	stat.	Multijet	stat.	Ztautau	stat.	Wtaunu	stat.	Top	stat.	Others	stat.
MCWEIGHT	69916546.00	8361.61	0.00	0.00	311130.53	863.35	1779351.12	7812.19	1975410.12	1245.51	2968869.66	9560.68
MIN_TWO_TAUS	6210024.00	2491.99	0.00	0.00	121486.21	538.25	548525.87	4619.29	818570.20	885.87	607877.73	5147.25
MUONVETO	5942820.00	2437.79	0.00	0.00	110277.24	512.19	520010.21	4502.39	588054.30	777.60	462249.06	4475.17
ELEVETO	5782360.00	2404.65	0.00	0.00	105740.88	501.96	507405.87	4462.22	544608.94	765.10	173429.59	2860.45
TRIGGERMATCH	2871120.00	1694.44	0.00	0.00	39204.34	295.28	222461.73	2436.59	285903.60	558.78	79389.08	1766.74
LEADTAU_PASS_MEDIUM	681513.00	825.54	0.00	0.00	13546.74	163.33	32834.94	744.49	10974.61	52.87	2807.21	65.49
LEADTAU_PT	595567.00	771.73	0.00	0.00	12451.24	155.51	29314.75	568.64	10070.35	50.98	2474.76	55.66
SUBLEADTAU_PT	512763.00	716.07	0.00	0.00	10870.63	143.68	25235.71	536.22	8440.95	46.77	2095.84	49.00
BVETOED	487214.00	698.01	0.00	0.00	10525.40	140.85	24173.96	533.53	2537.09	24.79	2009.17	48.74
SUBLEADTAU_PASS_LOOSE	12891.00	113.54	0.00	0.00	4365.88	73.77	1714.12	39.22	199.34	5.43	236.01	7.66
OS	7954.00	89.19	0.00	0.00	4392.03	75.08	1350.04	35.96	160.63	5.28	190.68	7.03
ZPRIME WEIGHT	7954.00	89.19	5307.45	21.31	4392.03	75.08	1350.05	35.96	160.64	5.28	190.68	7.03
PILEUP WEIGHT	7954.00	89.19	5307.45	21.31	4351.88	82.12	1321.76	40.00	158.57	5.77	186.86	7.65
trigger SF	7954.00	89.19	5307.45	21.31	1419.04	35.52	368.45	10.56	51.74	2.62	58.82	2.91
delta phi > 2.7	4931.00	70.22	3755.18	18.12	690.14	8.52	229.00	7.09	31.13	2.29	29.95	2.43
sublead tau pT > 65 GeV	4059.00	63.71	3039.71	16.62	613.40	7.74	178.12	6.23	26.17	2.12	24.69	1.86

BTAG

Cut	Data	stat.	Multijet	stat.	Ztautau	stat.	Wtaunu	stat.	Top	stat.	Others	stat.
MCWEIGHT	69916546.00	8361.61	0.00	0.00	311130.53	863.35	1779351.12	7812.19	1975410.12	1245.51	2968869.66	9560.68
MIN_TWO_TAUS	6210024.00	2491.99	0.00	0.00	121486.21	538.25	548525.87	4619.29	818570.20	885.87	607877.73	5147.25
MUONVETO	5942820.00	2437.79	0.00	0.00	110277.24	512.19	520010.21	4502.39	588054.30	777.60	462249.06	4475.17
ELEVETO	5782360.00	2404.65	0.00	0.00	105740.88	501.96	507405.87	4462.22	544608.94	765.10	173429.59	2860.45
TRIGGERMATCH	2871120.00	1694.44	0.00	0.00	39204.34	295.28	222461.73	2436.59	285903.60	558.78	79389.08	1766.74
LEADTAU_PASS_MEDIUM	681513.00	825.54	0.00	0.00	13546.74	163.33	32834.94	744.49	10974.61	52.87	2807.21	65.49
LEADTAU_PT	595567.00	771.73	0.00	0.00	12451.24	155.51	29314.75	568.64	10070.35	50.98	2474.76	55.66
SUBLEADTAU_PT	512763.00	716.07	0.00	0.00	10870.63	143.68	25235.71	536.22	8440.95	46.77	2095.84	49.00
BTAGGED	25549.00	159.84	0.00	0.00	341.46	28.33	1065.80	49.13	5901.04	39.76	86.04	4.86
SUBLEADTAU_PASS_LOOSE	824.00	28.71	0.00	0.00	129.32	15.90	57.27	3.38	545.22	9.85	10.73	1.32
OS	521.00	22.83	0.00	0.00	126.27	15.99	38.72	2.78	463.37	9.69	8.18	1.14
ZPRIME WEIGHT	521.00	22.83	272.87	4.80	126.27	15.99	38.72	2.78	463.32	9.69	8.18	1.14
PILEUP WEIGHT	521.00	22.83	272.87	4.80	115.77	14.12	38.42	2.53	457.54	10.74	8.82	1.59
trigger SF	521.00	22.83	272.87	4.80	33.40	4.68	12.35	0.78	142.41	4.41	4.34	0.97
delta phi > 2.7	199.00	14.11	137.42	3.46	8.09	0.99	4.96	0.41	75.54	3.48	1.18	0.72
sublead tau pT > 65 GeV	154.00	12.41	106.03	3.11	7.49	0.96	4.02	0.37	59.76	3.07	0.96	0.71

Table A.6: Cutflow table of the background processes in the *b*-veto (top) and *b*-tag (bottom) category for an integrated luminosity of 36.1 fb⁻¹.

BVETO

Cut	ggH200	stat.	ggH500	stat.	ggH800	stat.	ggH1000	stat.	ggH1200	stat.	ggH1500	stat.	ggH2000	stat.	ggH2500	stat.
MCWEIGHT	4215.38	36.77	14445.30	82.19	17720.33	84.10	18833.61	86.14	19596.49	87.78	20296.91	80.03	20426.09	80.81	20279.58	81.12
MIN_TWO_TAUS	2296.74	26.95	6685.57	54.26	7774.76	55.03	7923.60	55.28	8119.65	56.02	8052.48	50.09	7571.00	48.20	7114.62	47.87
MUONVETO	2222.43	26.50	6413.96	52.88	7368.29	53.51	7481.85	53.66	7589.54	54.09	7423.59	48.04	6905.96	45.73	6397.88	45.35
ELEVETO	2123.05	25.87	5870.62	49.38	6323.92	49.40	6158.01	48.48	5929.81	47.60	5414.02	40.84	4662.62	36.67	4013.08	35.77
TRIGGERMATCH	738.66	15.22	4794.60	45.36	5388.86	45.60	5272.29	44.86	5100.54	44.14	4641.05	37.81	3979.48	33.82	3411.71	32.98
LEADTAU_PASS_MEDIUM	531.05	12.97	3749.21	40.16	4126.18	40.16	4003.74	39.35	3797.59	38.34	3409.05	32.61	2825.90	28.48	2339.00	27.48
LEADTAU_PT	477.29	12.30	3732.19	40.12	4122.64	40.14	3998.26	39.32	3795.25	38.32	3407.17	32.61	2825.57	28.48	2339.00	27.48
SUBLEADTAU_PT	397.49	11.22	3598.87	39.65	4039.51	39.73	3924.32	38.96	3730.54	37.99	3354.64	32.35	2778.12	28.23	2291.38	27.19
BVETOED	386.33	11.06	3524.62	39.14	3946.64	39.25	3822.05	38.41	3631.87	37.46	3236.47	31.74	2666.78	27.62	2207.09	26.66
SUBLEADTAU_PASS_LOOSE	269.82	9.13	2839.71	34.85	3226.50	35.06	3108.85	34.22	2926.58	33.22	2568.79	27.91	2075.64	23.78	1652.36	22.71
OS	266.57	9.08	2788.63	34.51	3153.92	34.67	3034.58	33.82	2845.20	32.77	2482.17	27.45	1980.12	23.18	1558.28	22.07
ZPRIME WEIGHT	266.57	9.08	2788.63	34.51	3153.92	34.67	3034.57	33.82	2845.21	32.77	2482.17	27.45	1980.12	23.18	1558.28	22.07
PILEUP WEIGHT	269.21	10.22	2789.16	39.23	3151.84	39.10	3016.12	37.86	2850.02	37.37	2473.14	31.14	1950.90	26.55	1564.52	25.68
trigger SF	47.89	2.18	1783.05	31.24	2492.05	31.84	2459.46	31.37	2354.83	31.31	2088.05	26.44	1664.97	22.71	1337.26	21.98
delta phi > 2.7	25.38	1.21	1615.40	29.83	2293.75	30.59	2281.30	30.28	2196.40	30.33	1961.05	25.57	1568.20	22.07	1270.29	21.43
sublead tau pT > 65 GeV	17.13	0.98	1528.61	29.35	2233.76	30.21	2231.24	29.97	2157.79	30.10	1940.46	25.46	1551.51	21.95	1263.84	21.37

BTAG

Cut	ggH200	stat.	ggH500	stat.	ggH800	stat.	ggH1000	stat.	ggH1200	stat.	ggH1500	stat.	ggH2000	stat.	ggH2500	stat.
MCWEIGHT	4215.38	36.77	14445.30	82.19	17720.33	84.10	18833.61	86.14	19596.49	87.78	20296.91	80.03	20426.09	80.81	20279.58	81.12
MIN_TWO_TAUS	2296.74	26.95	6685.57	54.26	7774.76	55.03	7923.60	55.28	8119.65	56.02	8052.48	50.09	7571.00	48.20	7114.62	47.87
MUONVETO	2222.43	26.50	6413.96	52.88	7368.29	53.51	7481.85	53.66	7589.54	54.09	7423.59	48.04	6905.96	45.73	6397.88	45.35
ELEVETO	2123.05	25.87	5870.62	49.38	6323.92	49.40	6158.01	48.48	5929.81	47.60	5414.02	40.84	4662.62	36.67	4013.08	35.77
TRIGGERMATCH	738.66	15.22	4794.60	45.36	5388.86	45.60	5272.29	44.86	5100.54	44.14	4641.05	37.81	3979.48	33.82	3411.71	32.98
LEADTAU_PASS_MEDIUM	531.05	12.97	3749.21	40.16	4126.18	40.16	4003.74	39.35	3797.59	38.34	3409.05	32.61	2825.90	28.48	2339.00	27.48
LEADTAU_PT	477.29	12.30	3732.19	40.12	4122.64	40.14	3998.26	39.32	3795.25	38.32	3407.17	32.61	2825.57	28.48	2339.00	27.48
SUBLEADTAU_PT	397.49	11.22	3598.87	39.65	4039.51	39.73	3924.32	38.96	3730.54	37.99	3354.64	32.35	2778.12	28.23	2291.38	27.19
BTAGGED	11.55	1.99	74.98	6.46	92.83	6.25	102.63	6.55	98.77	6.42	118.36	6.29	112.60	5.89	83.28	5.35
SUBLEADTAU_PASS_LOOSE	7.45	1.59	57.77	5.58	70.76	5.35	77.12	5.56	76.80	5.58	87.63	5.32	84.83	4.91	62.11	4.55
OS	7.44	1.59	56.10	5.51	68.56	5.27	75.18	5.50	73.18	5.46	83.31	5.20	82.37	4.79	60.59	4.49
ZPRIME WEIGHT	7.44	1.59	56.10	5.51	68.56	5.27	75.18	5.50	73.18	5.46	83.31	5.20	82.37	4.79	60.59	4.49
PILEUP WEIGHT	7.48	1.82	55.97	5.86	64.85	5.39	74.77	6.23	67.92	5.38	84.66	6.09	87.56	5.37	57.82	4.79
trigger SF	2.93	1.08	38.71	4.67	51.92	4.43	60.85	5.12	56.90	4.53	72.19	5.21	74.76	4.60	48.90	4.04
delta phi > 2.7	0.22	0.13	28.00	4.29	39.41	3.82	49.79	4.63	49.53	4.28	62.99	4.96	65.05	4.25	43.44	3.84
sublead tau pT > 65 GeV	0.03	0.03	27.08	4.26	38.89	3.81	49.01	4.61	49.19	4.27	62.73	4.96	64.57	4.25	42.65	3.80

Table A.7: Cutflow table of the gluon-gluon fusion signal yields for different mass scenarios in the b-veto (top) and b-tag category (bottom) for an integrated luminosity of 36.1 fb^{-1} and an assumed cross section of 1 pb.

BVETO

Cut	bbH200	stat.	bbH500	stat.	bbH800	stat.	bbH1000	stat.	bbH1200	stat.	bbH1500	stat.	bbH2000	stat.	bbH2500	stat.
MCWEIGHT	4629.97	41.11	15122.41	77.17	18532.57	94.43	19579.38	86.42	20253.41	76.17	20703.71	101.16	20441.91	242.19	20542.53	236.88
MIN_TWO_TAUS	2637.09	30.66	7350.06	53.07	8540.14	63.77	8743.55	57.88	8833.96	43.96	8650.92	65.23	8070.73	151.19	7577.37	144.24
MUONVETO	2409.67	29.51	6501.80	49.98	7381.75	59.28	7506.71	53.52	7459.45	38.64	7263.98	59.50	6633.47	136.98	6280.36	130.22
ELEVETO	2306.13	28.83	5943.01	47.77	6348.64	54.88	6185.90	48.51	5859.94	30.59	5334.89	50.74	4416.27	111.76	3906.33	103.11
TRIGGERMATCH	864.34	17.27	4839.67	42.89	5420.37	50.21	5231.51	44.48	4957.64	28.03	4540.31	46.51	3721.85	102.11	3267.81	93.63
LEADTAU_PASS_MEDIUM	592.73	14.63	3797.07	38.29	4259.71	44.63	4037.82	39.30	3798.92	24.38	3376.33	40.41	2746.51	87.12	2298.22	78.34
LEADTAU_PT	523.72	13.79	3780.43	38.21	4254.67	44.59	4034.68	39.29	3797.88	24.38	3376.38	40.41	2746.45	87.11	2297.43	78.33
SUBLEADTAU_PT	436.54	12.76	3634.48	37.49	4150.48	44.06	3961.99	38.88	3731.41	24.05	3319.21	39.98	2698.20	86.06	2258.00	77.41
BVETOED	292.82	10.65	2248.37	29.69	2402.83	33.83	2238.54	29.47	2097.84	18.12	1849.79	29.90	1503.76	64.25	1206.85	57.77
SUBLEADTAU_PASS_LOOSE	208.29	8.77	1784.23	26.03	1918.27	29.60	1783.17	25.74	1634.33	15.11	1437.08	25.54	1091.30	53.14	834.53	46.26
OS	206.57	8.72	1759.66	25.82	1876.90	29.28	1738.28	25.42	1589.63	14.90	1378.90	25.09	1021.25	51.83	785.30	44.81
ZPRIME WEIGHT	206.57	8.72	1759.74	25.82	1876.92	29.28	1738.24	25.42	1589.62	14.90	1378.88	25.09	1021.25	51.83	785.30	44.81
PILEUP WEIGHT	211.13	9.92	1739.97	29.40	1869.71	32.92	1712.82	28.69	1587.32	16.86	1372.65	28.71	1056.12	60.03	760.48	49.05
trigger SF	30.50	1.53	1114.09	20.60	1420.01	27.03	1332.40	24.06	1167.04	14.69	1091.73	24.24	900.16	51.46	649.73	42.02
delta phi > 2.7	23.85	1.30	1023.63	19.96	1336.36	26.33	1256.71	23.44	1101.29	13.96	1056.11	23.89	863.21	50.22	636.34	40.92
sublead tau pT > 65 GeV	16.74	1.05	967.09	19.45	1311.18	26.02	1241.94	23.26	1090.44	13.87	1050.44	23.77	852.68	50.03	632.45	40.78

BTAG

Cut	bbH200	stat.	bbH500	stat.	bbH800	stat.	bbH1000	stat.	bbH1200	stat.	bbH1500	stat.	bbH2000	stat.	bbH2500	stat.
MCWEIGHT	4629.97	41.11	15122.41	77.17	18532.57	94.43	19579.38	86.42	20253.41	76.17	20703.71	101.16	20441.91	242.19	20542.53	236.88
MIN_TWO_TAUS	2637.09	30.66	7350.06	53.07	8540.14	63.77	8743.55	57.88	8833.96	43.96	8650.92	65.23	8070.73	151.19	7577.37	144.24
MUONVETO	2409.67	29.51	6501.80	49.98	7381.75	59.28	7506.71	53.52	7459.45	38.64	7263.98	59.50	6633.47	136.98	6280.36	130.22
ELEVETO	2306.13	28.83	5943.01	47.77	6348.64	54.88	6185.90	48.51	5859.94	30.59	5334.89	50.74	4416.27	111.76	3906.33	103.11
TRIGGERMATCH	864.34	17.27	4839.67	42.89	5420.37	50.21	5231.51	44.48	4957.64	28.03	4540.31	46.51	3721.85	102.11	3267.81	93.63
LEADTAU_PASS_MEDIUM	592.73	14.63	3797.07	38.29	4259.71	44.63	4037.82	39.30	3798.92	24.38	3376.33	40.41	2746.51	87.12	2298.22	78.34
LEADTAU_PT	523.72	13.79	3780.43	38.21	4254.67	44.59	4034.68	39.29	3797.88	24.38	3376.38	40.41	2746.45	87.11	2297.43	78.33
SUBLEADTAU_PT	436.54	12.76	3634.48	37.49	4150.48	44.06	3961.99	38.88	3731.41	24.05	3319.21	39.98	2698.20	86.06	2258.00	77.41
BTAGGED	143.99	7.04	1389.08	22.97	1750.22	28.32	1730.17	25.46	1634.76	15.87	1470.29	26.65	1198.40	57.58	1054.73	51.80
SUBLEADTAU_PASS_LOOSE	95.56	5.69	1077.19	19.85	1383.75	24.52	1358.07	24.40	1279.01	13.20	1123.94	22.64	907.22	47.70	760.46	41.75
OS	94.20	5.66	1063.87	19.69	1358.97	24.27	1334.65	21.98	1241.56	13.01	1092.55	22.23	856.04	46.54	715.19	40.38
ZPRIME WEIGHT	94.20	5.66	1063.88	19.69	1353.96	24.27	1334.65	21.72	1241.56	13.00	1092.55	22.23	856.04	46.54	715.19	40.38
PILEUP WEIGHT	94.25	6.28	1046.96	22.39	1347.95	27.15	1279.01	24.40	1233.87	14.69	1100.64	25.55	834.70	53.45	698.07	45.18
trigger SF	15.88	1.22	694.70	15.93	1106.46	22.29	1037.44	20.48	936.76	12.46	856.04	22.23	708.45	45.75	599.87	38.75
delta phi > 2.7	8.54	0.74	539.33	14.38	918.12	20.75	907.33	19.19	842.76	11.76	770.64	20.70	654.43	44.04	562.45	37.21
sublead tau pT > 65 GeV	5.49	0.55	515.27	14.02	897.12	20.50	897.12	19.04	835.91	11.69	762.33	20.60	649.44	43.89	561.05	37.12

Table A.8: Cutflow table of the *b*-associated production signal yields for different mass scenarios in the *b*-veto (top) and *b*-tag category (bottom) for an integrated luminosity of 36.1 fb^{-1} and an assumed cross section of 1 pb.

A.3 MC Files

```
mc15_13TeV.301000.PowhegPythia8EvtGen_AZNLOCTEQ6L1_DYee_120M180.merge.DAOD_HIGG4D4.e3649_s2576_s2132_r7772_r7676_p2823
mc15_13TeV.301001.PowhegPythia8EvtGen_AZNLOCTEQ6L1_DYee_180M250.merge.DAOD_HIGG4D4.e3649_s2576_s2132_r7772_r7676_p2823
mc15_13TeV.301002.PowhegPythia8EvtGen_AZNLOCTEQ6L1_DYee_250M400.merge.DAOD_HIGG4D4.e3649_s2576_s2132_r7772_r7676_p2823
mc15_13TeV.301003.PowhegPythia8EvtGen_AZNLOCTEQ6L1_DYee_400M600.merge.DAOD_HIGG4D4.e3649_s2576_s2132_r7772_r7676_p2823
mc15_13TeV.301004.PowhegPythia8EvtGen_AZNLOCTEQ6L1_DYee_600M800.merge.DAOD_HIGG4D4.e3649_s2576_s2132_r7772_r7676_p2823
mc15_13TeV.301005.PowhegPythia8EvtGen_AZNLOCTEQ6L1_DYee_800M1000.merge.DAOD_HIGG4D4.e3649_s2576_s2132_r7772_r7676_p2823
mc15_13TeV.301006.PowhegPythia8EvtGen_AZNLOCTEQ6L1_DYee_1000M1250.merge.DAOD_HIGG4D4.e3649_s2576_s2132_r7772_r7676_p2823
mc15_13TeV.301007.PowhegPythia8EvtGen_AZNLOCTEQ6L1_DYee_1250M1500.merge.DAOD_HIGG4D4.e3649_s2576_s2132_r7772_r7676_p2823
mc15_13TeV.301008.PowhegPythia8EvtGen_AZNLOCTEQ6L1_DYee_1500M1750.merge.DAOD_HIGG4D4.e3649_s2576_s2132_r7772_r7676_p2823
mc15_13TeV.301009.PowhegPythia8EvtGen_AZNLOCTEQ6L1_DYee_1750M2000.merge.DAOD_HIGG4D4.e3649_s2576_s2132_r7772_r7676_p2823
mc15_13TeV.301010.PowhegPythia8EvtGen_AZNLOCTEQ6L1_DYee_2000M2250.merge.DAOD_HIGG4D4.e3649_s2576_s2132_r7772_r7676_p2823
mc15_13TeV.301011.PowhegPythia8EvtGen_AZNLOCTEQ6L1_DYee_2250M2500.merge.DAOD_HIGG4D4.e3649_s2576_s2132_r7772_r7676_p2823
mc15_13TeV.301012.PowhegPythia8EvtGen_AZNLOCTEQ6L1_DYee_2500M2750.merge.DAOD_HIGG4D4.e3649_s2576_s2132_r7772_r7676_p2823
mc15_13TeV.301013.PowhegPythia8EvtGen_AZNLOCTEQ6L1_DYee_2750M3000.merge.DAOD_HIGG4D4.e3649_s2576_s2132_r7772_r7676_p2823
mc15_13TeV.301014.PowhegPythia8EvtGen_AZNLOCTEQ6L1_DYee_3000M3500.merge.DAOD_HIGG4D4.e3649_s2576_s2132_r7772_r7676_p2823
mc15_13TeV.301015.PowhegPythia8EvtGen_AZNLOCTEQ6L1_DYee_3500M4000.merge.DAOD_HIGG4D4.e3649_s2576_s2132_r7772_r7676_p2823
mc15_13TeV.301016.PowhegPythia8EvtGen_AZNLOCTEQ6L1_DYee_4000M4500.merge.DAOD_HIGG4D4.e3649_s2576_s2132_r7772_r7676_p2823
mc15_13TeV.301017.PowhegPythia8EvtGen_AZNLOCTEQ6L1_DYee_4500M5000.merge.DAOD_HIGG4D4.e3649_s2576_s2132_r7772_r7676_p2823
mc15_13TeV.301018.PowhegPythia8EvtGen_AZNLOCTEQ6L1_DYee_5000M.merge.DAOD_HIGG4D4.e3649_s2576_s2132_r7772_r7676_p2823
mc15_13TeV.301020.PowhegPythia8EvtGen_AZNLOCTEQ6L1_DYmumu_120M180.merge.DAOD_HIGG4D4.e3649_s2576_s2132_r7772_r7676_p2823
mc15_13TeV.301021.PowhegPythia8EvtGen_AZNLOCTEQ6L1_DYmumu_180M250.merge.DAOD_HIGG4D4.e3649_s2576_s2132_r7772_r7676_p2823
mc15_13TeV.301022.PowhegPythia8EvtGen_AZNLOCTEQ6L1_DYmumu_250M400.merge.DAOD_HIGG4D4.e3649_s2576_s2132_r7772_r7676_p2823
mc15_13TeV.301023.PowhegPythia8EvtGen_AZNLOCTEQ6L1_DYmumu_400M600.merge.DAOD_HIGG4D4.e3649_s2576_s2132_r7772_r7676_p2823
mc15_13TeV.301024.PowhegPythia8EvtGen_AZNLOCTEQ6L1_DYmumu_600M800.merge.DAOD_HIGG4D4.e3649_s2576_s2132_r7772_r7676_p2823
mc15_13TeV.301025.PowhegPythia8EvtGen_AZNLOCTEQ6L1_DYmumu_800M1000.merge.DAOD_HIGG4D4.e3649_s2576_s2132_r7772_r7676_p2823
mc15_13TeV.301026.PowhegPythia8EvtGen_AZNLOCTEQ6L1_DYmumu_1000M1250.merge.DAOD_HIGG4D4.e3649_s2576_s2132_r7772_r7676_p2823
mc15_13TeV.301027.PowhegPythia8EvtGen_AZNLOCTEQ6L1_DYmumu_1250M1500.merge.DAOD_HIGG4D4.e3649_s2576_s2132_r7772_r7676_p2823
mc15_13TeV.301028.PowhegPythia8EvtGen_AZNLOCTEQ6L1_DYmumu_1500M1750.merge.DAOD_HIGG4D4.e3649_s2576_s2132_r7772_r7676_p2823
mc15_13TeV.301029.PowhegPythia8EvtGen_AZNLOCTEQ6L1_DYmumu_1750M2000.merge.DAOD_HIGG4D4.e3649_s2576_s2132_r7772_r7676_p2823
mc15_13TeV.301030.PowhegPythia8EvtGen_AZNLOCTEQ6L1_DYmumu_2000M2250.merge.DAOD_HIGG4D4.e3649_s2576_s2132_r7772_r7676_p2823
mc15_13TeV.301031.PowhegPythia8EvtGen_AZNLOCTEQ6L1_DYmumu_2250M2500.merge.DAOD_HIGG4D4.e3649_s2576_s2132_r7772_r7676_p2823
mc15_13TeV.301032.PowhegPythia8EvtGen_AZNLOCTEQ6L1_DYmumu_2500M2750.merge.DAOD_HIGG4D4.e3649_s2576_s2132_r7772_r7676_p2823
mc15_13TeV.301033.PowhegPythia8EvtGen_AZNLOCTEQ6L1_DYmumu_2750M3000.merge.DAOD_HIGG4D4.e3649_s2576_s2132_r7772_r7676_p2823
mc15_13TeV.301034.PowhegPythia8EvtGen_AZNLOCTEQ6L1_DYmumu_3000M3500.merge.DAOD_HIGG4D4.e3649_s2576_s2132_r7772_r7676_p2823
mc15_13TeV.301035.PowhegPythia8EvtGen_AZNLOCTEQ6L1_DYmumu_3500M4000.merge.DAOD_HIGG4D4.e3649_s2576_s2132_r7772_r7676_p2823
mc15_13TeV.301036.PowhegPythia8EvtGen_AZNLOCTEQ6L1_DYmumu_4000M4500.merge.DAOD_HIGG4D4.e3649_s2576_s2132_r7772_r7676_p2823
mc15_13TeV.301037.PowhegPythia8EvtGen_AZNLOCTEQ6L1_DYmumu_4500M5000.merge.DAOD_HIGG4D4.e3649_s2576_s2132_r7772_r7676_p2823
mc15_13TeV.301038.PowhegPythia8EvtGen_AZNLOCTEQ6L1_DYmumu_5000M.merge.DAOD_HIGG4D4.e3649_s2576_s2132_r7772_r7676_p2823
mc15_13TeV.301040.PowhegPythia8EvtGen_AZNLOCTEQ6L1_DYtautau_120M180.merge.DAOD_HIGG4D4.e3649_s2576_s2132_r7772_r7676_p2823
mc15_13TeV.301041.PowhegPythia8EvtGen_AZNLOCTEQ6L1_DYtautau_180M250.merge.DAOD_HIGG4D4.e3649_s2576_s2132_r7772_r7676_p2823
mc15_13TeV.301042.PowhegPythia8EvtGen_AZNLOCTEQ6L1_DYtautau_250M400.merge.DAOD_HIGG4D4.e3649_s2576_s2132_r7772_r7676_p2823
mc15_13TeV.301043.PowhegPythia8EvtGen_AZNLOCTEQ6L1_DYtautau_400M600.merge.DAOD_HIGG4D4.e3649_s2576_s2132_r7772_r7676_p2823
mc15_13TeV.301044.PowhegPythia8EvtGen_AZNLOCTEQ6L1_DYtautau_600M800.merge.DAOD_HIGG4D4.e3649_s2576_s2132_r7772_r7676_p2823
mc15_13TeV.301045.PowhegPythia8EvtGen_AZNLOCTEQ6L1_DYtautau_800M1000.merge.DAOD_HIGG4D4.e3649_s2576_s2132_r7772_r7676_p2823
mc15_13TeV.301046.PowhegPythia8EvtGen_AZNLOCTEQ6L1_DYtautau_1000M1250.merge.DAOD_HIGG4D4.e3649_s2576_s2132_r7772_r7676_p2823
mc15_13TeV.301047.PowhegPythia8EvtGen_AZNLOCTEQ6L1_DYtautau_1250M1500.merge.DAOD_HIGG4D4.e3649_s2576_s2132_r7772_r7676_p2823
mc15_13TeV.301048.PowhegPythia8EvtGen_AZNLOCTEQ6L1_DYtautau_1500M1750.merge.DAOD_HIGG4D4.e3649_s2576_s2132_r7772_r7676_p2823
mc15_13TeV.301049.PowhegPythia8EvtGen_AZNLOCTEQ6L1_DYtautau_1750M2000.merge.DAOD_HIGG4D4.e3649_s2576_s2132_r7772_r7676_p2823
mc15_13TeV.301050.PowhegPythia8EvtGen_AZNLOCTEQ6L1_DYtautau_2000M2250.merge.DAOD_HIGG4D4.e3649_s2576_s2132_r7772_r7676_p2823
mc15_13TeV.301051.PowhegPythia8EvtGen_AZNLOCTEQ6L1_DYtautau_2250M2500.merge.DAOD_HIGG4D4.e3649_s2576_s2132_r7772_r7676_p2823
mc15_13TeV.301052.PowhegPythia8EvtGen_AZNLOCTEQ6L1_DYtautau_2500M2750.merge.DAOD_HIGG4D4.e3649_s2576_s2132_r7772_r7676_p2823
mc15_13TeV.301053.PowhegPythia8EvtGen_AZNLOCTEQ6L1_DYtautau_2750M3000.merge.DAOD_HIGG4D4.e3649_s2576_s2132_r7772_r7676_p2823
mc15_13TeV.301054.PowhegPythia8EvtGen_AZNLOCTEQ6L1_DYtautau_3000M3500.merge.DAOD_HIGG4D4.e3649_s2576_s2132_r7772_r7676_p2823
mc15_13TeV.301055.PowhegPythia8EvtGen_AZNLOCTEQ6L1_DYtautau_3500M4000.merge.DAOD_HIGG4D4.e3649_s2576_s2132_r7772_r7676_p2823
mc15_13TeV.301056.PowhegPythia8EvtGen_AZNLOCTEQ6L1_DYtautau_4000M4500.merge.DAOD_HIGG4D4.e3649_s2576_s2132_r7772_r7676_p2823
mc15_13TeV.301057.PowhegPythia8EvtGen_AZNLOCTEQ6L1_DYtautau_4500M5000.merge.DAOD_HIGG4D4.e3649_s2576_s2132_r7772_r7676_p2823
mc15_13TeV.301058.PowhegPythia8EvtGen_AZNLOCTEQ6L1_DYtautau_5000M.merge.DAOD_HIGG4D4.e3649_s2576_s2132_r7772_r7676_p2823
mc15_13TeV.303437.Pythia8EvtGen_A14NNPDF23LO_DYtautau_120M180.merge.DAOD_HIGG4D4.e4213_s2608_s2183_r7772_r7676_p2823
mc15_13TeV.303438.Pythia8EvtGen_A14NNPDF23LO_DYtautau_180M250.merge.DAOD_HIGG4D4.e4213_s2608_s2183_r7772_r7676_p2823
mc15_13TeV.303439.Pythia8EvtGen_A14NNPDF23LO_DYtautau_250M400.merge.DAOD_HIGG4D4.e4213_s2608_s2183_r7772_r7676_p2823
mc15_13TeV.303440.Pythia8EvtGen_A14NNPDF23LO_DYtautau_400M600.merge.DAOD_HIGG4D4.e4213_s2608_s2183_r7772_r7676_p2823
mc15_13TeV.303441.Pythia8EvtGen_A14NNPDF23LO_DYtautau_600M800.merge.DAOD_HIGG4D4.e4213_s2608_s2183_r7772_r7676_p2823
mc15_13TeV.303442.Pythia8EvtGen_A14NNPDF23LO_DYtautau_800M1000.merge.DAOD_HIGG4D4.e4213_s2608_s2183_r7772_r7676_p2823
mc15_13TeV.303443.Pythia8EvtGen_A14NNPDF23LO_DYtautau_1000M1250.merge.DAOD_HIGG4D4.e4213_s2608_s2183_r7772_r7676_p2823
mc15_13TeV.303444.Pythia8EvtGen_A14NNPDF23LO_DYtautau_1250M1500.merge.DAOD_HIGG4D4.e4213_s2608_s2183_r7772_r7676_p2823
mc15_13TeV.303445.Pythia8EvtGen_A14NNPDF23LO_DYtautau_1500M1750.merge.DAOD_HIGG4D4.e4213_s2608_s2183_r7772_r7676_p2823
mc15_13TeV.303446.Pythia8EvtGen_A14NNPDF23LO_DYtautau_1750M2000.merge.DAOD_HIGG4D4.e4213_s2608_s2183_r7772_r7676_p2823
mc15_13TeV.303447.Pythia8EvtGen_A14NNPDF23LO_DYtautau_2000M2250.merge.DAOD_HIGG4D4.e4213_s2608_s2183_r7772_r7676_p2823
mc15_13TeV.303448.Pythia8EvtGen_A14NNPDF23LO_DYtautau_2250M2500.merge.DAOD_HIGG4D4.e4213_s2608_s2183_r7772_r7676_p2823
mc15_13TeV.303449.Pythia8EvtGen_A14NNPDF23LO_DYtautau_2500M2750.merge.DAOD_HIGG4D4.e4213_s2608_s2183_r7772_r7676_p2823
mc15_13TeV.303450.Pythia8EvtGen_A14NNPDF23LO_DYtautau_2750M3000.merge.DAOD_HIGG4D4.e4213_s2608_s2183_r7772_r7676_p2823
mc15_13TeV.303451.Pythia8EvtGen_A14NNPDF23LO_DYtautau_3000M3500.merge.DAOD_HIGG4D4.e4213_s2608_s2183_r7772_r7676_p2823
```

mc15_13TeV.303452.Pythia8EvtGen_A14NNPDF23LO_DYtautau_3500M4000.merge.DAOD_HIGG4D4.e4213_s2608_s2183_r7772_r7676_p2823
mc15_13TeV.303453.Pythia8EvtGen_A14NNPDF23LO_DYtautau_4000M4500.merge.DAOD_HIGG4D4.e4213_s2608_s2183_r7772_r7676_p2823
mc15_13TeV.303454.Pythia8EvtGen_A14NNPDF23LO_DYtautau_4500M5000.merge.DAOD_HIGG4D4.e4213_s2608_s2183_r7772_r7676_p2823
mc15_13TeV.303455.Pythia8EvtGen_A14NNPDF23LO_DYtautau_5000M.merge.DAOD_HIGG4D4.e4213_s2608_s2183_r7772_r7676_p2823
mc15_13TeV.305785.Pythia8EvtGen_A14NNPDF23LO_DYtautau_70M120.merge.DAOD_HIGG4D4.e5200_s2726_r7772_r7676_p2823
mc15_13TeV.341858.aMcAtNloPythia8EvtGen_A14NNPDF23LO_bbH200_yb2_tautaulh.merge.DAOD_HIGG4D4.e4482_a766_a821_r7676_p2823
mc15_13TeV.341860.aMcAtNloPythia8EvtGen_A14NNPDF23LO_bbH300_yb2_tautaulh.merge.DAOD_HIGG4D4.e4482_a766_a821_r7676_p2823
mc15_13TeV.341861.aMcAtNloPythia8EvtGen_A14NNPDF23LO_bbH350_yb2_tautaulh.merge.DAOD_HIGG4D4.e4482_a766_a821_r7676_p2823
mc15_13TeV.341862.aMcAtNloPythia8EvtGen_A14NNPDF23LO_bbH400_yb2_tautaulh.merge.DAOD_HIGG4D4.e4298_a766_a821_r7676_p2823
mc15_13TeV.341863.aMcAtNloPythia8EvtGen_A14NNPDF23LO_bbH500_yb2_tautaulh.merge.DAOD_HIGG4D4.e4482_a766_a821_r7676_p2823
mc15_13TeV.341864.aMcAtNloPythia8EvtGen_A14NNPDF23LO_bbH600_yb2_tautaulh.merge.DAOD_HIGG4D4.e4482_a766_a821_r7676_p2823
mc15_13TeV.341865.aMcAtNloPythia8EvtGen_A14NNPDF23LO_bbH700_yb2_tautaulh.merge.DAOD_HIGG4D4.e4482_a766_a821_r7676_p2823
mc15_13TeV.341866.aMcAtNloPythia8EvtGen_A14NNPDF23LO_bbH800_yb2_tautaulh.merge.DAOD_HIGG4D4.e4482_a766_a821_r7676_p2823
mc15_13TeV.341868.aMcAtNloPythia8EvtGen_A14NNPDF23LO_bbH1000_yb2_tautaulh.merge.DAOD_HIGG4D4.e4298_a766_a821_r7676_p2823
mc15_13TeV.341870.aMcAtNloPythia8EvtGen_A14NNPDF23LO_bbH1200_yb2_tautaulh.merge.DAOD_HIGG4D4.e4482_a766_a821_r7676_p2823
mc15_13TeV.341875.aMcAtNloPythia8EvtGen_A14NNPDF23LO_bbH200_yb2_tautauhh.merge.DAOD_HIGG4D4.e4482_a766_a821_r7676_p2823
mc15_13TeV.341877.aMcAtNloPythia8EvtGen_A14NNPDF23LO_bbH300_yb2_tautauhh.merge.DAOD_HIGG4D4.e4482_a766_a821_r7676_p2823
mc15_13TeV.341878.aMcAtNloPythia8EvtGen_A14NNPDF23LO_bbH350_yb2_tautauhh.merge.DAOD_HIGG4D4.e4482_a766_a821_r7676_p2823
mc15_13TeV.341879.aMcAtNloPythia8EvtGen_A14NNPDF23LO_bbH400_yb2_tautauhh.merge.DAOD_HIGG4D4.e4298_a766_a821_r7676_p2823
mc15_13TeV.341880.aMcAtNloPythia8EvtGen_A14NNPDF23LO_bbH500_yb2_tautauhh.merge.DAOD_HIGG4D4.e4482_a766_a821_r7676_p2823
mc15_13TeV.341881.aMcAtNloPythia8EvtGen_A14NNPDF23LO_bbH600_yb2_tautauhh.merge.DAOD_HIGG4D4.e4482_a766_a821_r7676_p2823
mc15_13TeV.341882.aMcAtNloPythia8EvtGen_A14NNPDF23LO_bbH700_yb2_tautauhh.merge.DAOD_HIGG4D4.e4482_a766_a821_r7676_p2823
mc15_13TeV.341883.aMcAtNloPythia8EvtGen_A14NNPDF23LO_bbH800_yb2_tautauhh.merge.DAOD_HIGG4D4.e4482_a766_a821_r7676_p2823
mc15_13TeV.341885.aMcAtNloPythia8EvtGen_A14NNPDF23LO_bbH1000_yb2_tautauhh.merge.DAOD_HIGG4D4.e4298_a766_a821_r7676_p2823
mc15_13TeV.341917.aMcAtNloPythia8EvtGen_A14NNPDF23LO_bbH1200_yb2_tautauhh.merge.DAOD_HIGG4D4.e4482_a766_a821_r7676_p2823
mc15_13TeV.342305.PowhegPythia8EvtGen_CT10_AZNLOCTEQ6L1_ggH200W1_tautaulh.merge.DAOD_HIGG4D4.e4284_s2608_s2183_r7772_r7676_p2823
mc15_13TeV.342306.PowhegPythia8EvtGen_CT10_AZNLOCTEQ6L1_ggH200W1_tautauhh.merge.DAOD_HIGG4D4.e4284_s2608_s2183_r7772_r7676_p2823
mc15_13TeV.342310.PowhegPythia8EvtGen_CT10_AZNLOCTEQ6L1_ggH300W2_tautaulh.merge.DAOD_HIGG4D4.e4284_s2608_s2183_r7772_r7676_p2823
mc15_13TeV.342311.PowhegPythia8EvtGen_CT10_AZNLOCTEQ6L1_ggH300W2_tautauhh.merge.DAOD_HIGG4D4.e4284_s2608_s2183_r7772_r7676_p2823
mc15_13TeV.342312.PowhegPythia8EvtGen_CT10_AZNLOCTEQ6L1_ggH350W3_tautaulh.merge.DAOD_HIGG4D4.e4284_s2608_s2183_r7772_r7676_p2823
mc15_13TeV.342313.PowhegPythia8EvtGen_CT10_AZNLOCTEQ6L1_ggH350W3_tautauhh.merge.DAOD_HIGG4D4.e4284_s2608_s2183_r7772_r7676_p2823
mc15_13TeV.342314.PowhegPythia8EvtGen_CT10_AZNLOCTEQ6L1_ggH400W5_tautaulh.merge.DAOD_HIGG4D4.e4284_s2608_s2183_r7772_r7676_p2823
mc15_13TeV.342315.PowhegPythia8EvtGen_CT10_AZNLOCTEQ6L1_ggH400W5_tautauhh.merge.DAOD_HIGG4D4.e4284_s2608_s2183_r7772_r7676_p2823
mc15_13TeV.342316.PowhegPythia8EvtGen_CT10_AZNLOCTEQ6L1_ggH500W5_tautaulh.merge.DAOD_HIGG4D4.e4284_s2608_s2183_r7772_r7676_p2823
mc15_13TeV.342317.PowhegPythia8EvtGen_CT10_AZNLOCTEQ6L1_ggH500W5_tautauhh.merge.DAOD_HIGG4D4.e4284_s2608_s2183_r7772_r7676_p2823
mc15_13TeV.342318.PowhegPythia8EvtGen_CT10_AZNLOCTEQ6L1_ggH600W10_tautaulh.merge.DAOD_HIGG4D4.e4284_s2608_s2183_r7772_r7676_p2823
mc15_13TeV.342319.PowhegPythia8EvtGen_CT10_AZNLOCTEQ6L1_ggH600W10_tautauhh.merge.DAOD_HIGG4D4.e4284_s2608_s2183_r7772_r7676_p2823
mc15_13TeV.342320.PowhegPythia8EvtGen_CT10_AZNLOCTEQ6L1_ggH700W20_tautaulh.merge.DAOD_HIGG4D4.e4284_s2608_s2183_r7772_r7676_p2823
mc15_13TeV.342321.PowhegPythia8EvtGen_CT10_AZNLOCTEQ6L1_ggH700W20_tautaulh.merge.DAOD_HIGG4D4.e4284_s2608_s2183_r7772_r7676_p2823
mc15_13TeV.342322.PowhegPythia8EvtGen_CT10_AZNLOCTEQ6L1_ggH800W20_tautaulh.merge.DAOD_HIGG4D4.e4284_s2608_s2183_r7772_r7676_p2823
mc15_13TeV.342323.PowhegPythia8EvtGen_CT10_AZNLOCTEQ6L1_ggH800W20_tautauhh.merge.DAOD_HIGG4D4.e4284_s2608_s2183_r7772_r7676_p2823
mc15_13TeV.342326.PowhegPythia8EvtGen_CT10_AZNLOCTEQ6L1_ggH1000W30_tautaulh.merge.DAOD_HIGG4D4.e4284_s2608_s2183_r7772_r7676_p2823
mc15_13TeV.342327.PowhegPythia8EvtGen_CT10_AZNLOCTEQ6L1_ggH1000W30_tautauhh.merge.DAOD_HIGG4D4.e4284_s2608_s2183_r7772_r7676_p2823
mc15_13TeV.342330.PowhegPythia8EvtGen_CT10_AZNLOCTEQ6L1_ggH1200W40_tautaulh.merge.DAOD_HIGG4D4.e4284_s2608_s2183_r7772_r7676_p2823
mc15_13TeV.342331.PowhegPythia8EvtGen_CT10_AZNLOCTEQ6L1_ggH1200W40_tautauhh.merge.DAOD_HIGG4D4.e4284_s2608_s2183_r7772_r7676_p2823
mc15_13TeV.361021.Pythia8EvtGen_A14NNPDF23LO_jetjet_JZ1W.merge.DAOD_HIGG4D4.e3569_s2576_s2132_r7725_r7676_p2823
mc15_13TeV.361022.Pythia8EvtGen_A14NNPDF23LO_jetjet_JZ2W.merge.DAOD_HIGG4D4.e3668_s2576_s2132_r7725_r7676_p2823
mc15_13TeV.361023.Pythia8EvtGen_A14NNPDF23LO_jetjet_JZ3W.merge.DAOD_HIGG4D4.e3668_s2576_s2132_r7725_r7676_p2823
mc15_13TeV.361024.Pythia8EvtGen_A14NNPDF23LO_jetjet_JZ4W.merge.DAOD_HIGG4D4.e3668_s2576_s2132_r7725_r7676_p2823
mc15_13TeV.361025.Pythia8EvtGen_A14NNPDF23LO_jetjet_JZ5W.merge.DAOD_HIGG4D4.e3668_s2576_s2132_r7725_r7676_p2823
mc15_13TeV.361026.Pythia8EvtGen_A14NNPDF23LO_jetjet_JZ6W.merge.DAOD_HIGG4D4.e3569_s2608_s2183_r7725_r7676_p2823
mc15_13TeV.361027.Pythia8EvtGen_A14NNPDF23LO_jetjet_JZ7W.merge.DAOD_HIGG4D4.e3668_s2608_s2183_r7725_r7676_p2823
mc15_13TeV.361028.Pythia8EvtGen_A14NNPDF23LO_jetjet_JZ8W.merge.DAOD_HIGG4D4.e3569_s2576_s2132_r7772_r7676_p2823
mc15_13TeV.361029.Pythia8EvtGen_A14NNPDF23LO_jetjet_JZ9W.merge.DAOD_HIGG4D4.e3569_s2576_s2132_r7772_r7676_p2823
mc15_13TeV.361030.Pythia8EvtGen_A14NNPDF23LO_jetjet_JZ10W.merge.DAOD_HIGG4D4.e3569_s2576_s2132_r7772_r7676_p2823
mc15_13TeV.361031.Pythia8EvtGen_A14NNPDF23LO_jetjet_JZ11W.merge.DAOD_HIGG4D4.e3569_s2608_s2183_r7772_r7676_p2823
mc15_13TeV.361032.Pythia8EvtGen_A14NNPDF23LO_jetjet_JZ12W.merge.DAOD_HIGG4D4.e3668_s2608_s2183_r7772_r7676_p2823
mc15_13TeV.361063.Sherpa_CT10_llll.merge.DAOD_HIGG4D4.e3836_s2608_s2183_r7725_r7676_p2823
mc15_13TeV.361064.Sherpa_CT10_lllvSFMinus.merge.DAOD_HIGG4D4.e3836_s2608_s2183_r7725_r7676_p2823
mc15_13TeV.361065.Sherpa_CT10_lllvOFMinus.merge.DAOD_HIGG4D4.e3836_s2608_s2183_r7725_r7676_p2823
mc15_13TeV.361066.Sherpa_CT10_lllvSFPlus.merge.DAOD_HIGG4D4.e3836_s2608_s2183_r7725_r7676_p2823
mc15_13TeV.361067.Sherpa_CT10_lllvOFPlus.merge.DAOD_HIGG4D4.e3836_s2608_s2183_r7725_r7676_p2823
mc15_13TeV.361068.Sherpa_CT10_llvv.merge.DAOD_HIGG4D4.e3836_s2608_s2183_r7725_r7676_p2823
mc15_13TeV.361091.Sherpa_CT10_WplvWmqq_SHv21_improved.merge.DAOD_HIGG4D4.e4607_s2726_r7725_r7676_p2823
mc15_13TeV.361092.Sherpa_CT10_WpqqWmlv_SHv21_improved.merge.DAOD_HIGG4D4.e4607_s2726_r7725_r7676_p2823
mc15_13TeV.361093.Sherpa_CT10_WlvZqq_SHv21_improved.merge.DAOD_HIGG4D4.e4607_s2726_r7725_r7676_p2823
mc15_13TeV.361094.Sherpa_CT10_WqqZll_SHv21_improved.merge.DAOD_HIGG4D4.e4607_s2726_r7725_r7676_p2823
mc15_13TeV.361095.Sherpa_CT10_WqqZvv_SHv21_improved.merge.DAOD_HIGG4D4.e4607_s2726_r7772_r7676_p2823
mc15_13TeV.361096.Sherpa_CT10_ZqqZll_SHv21_improved.merge.DAOD_HIGG4D4.e4607_s2726_r7725_r7676_p2823
mc15_13TeV.361097.Sherpa_CT10_ZqqZvv_SHv21_improved.merge.DAOD_HIGG4D4.e4607_s2726_r7772_r7676_p2823
mc15_13TeV.361106.PowhegPythia8EvtGen_AZNLOCTEQ6L1_Zee.merge.DAOD_HIGG4D4.e3601_s2576_s2132_r7725_r7676_p2823
mc15_13TeV.361107.PowhegPythia8EvtGen_AZNLOCTEQ6L1_Zmumu.merge.DAOD_HIGG4D4.e3601_s2576_s2132_r7725_r7676_p2823
mc15_13TeV.361108.PowhegPythia8EvtGen_AZNLOCTEQ6L1_Ztautau.merge.DAOD_HIGG4D4.e3601_s2726_r7725_r7676_p2823
mc15_13TeV.363331.Sherpa_NNPDF30NNLO_Wtaunu_Pt0_70_CVetoBVeto.merge.DAOD_HIGG4D4.e4709_s2726_r7725_r7676_p2823

mc15__13TeV.363332.Sherpa__NNPDF30NNLO__Wtaunu__Pt0__70__CFilterBVeto.merge.DAOD__HIGG4D4.e4709__s2726__r7725__r7676__p2823
mc15__13TeV.363333.Sherpa__NNPDF30NNLO__Wtaunu__Pt0__70__BFilter.merge.DAOD__HIGG4D4.e4709__s2726__r7725__r7676__p2823
mc15__13TeV.363334.Sherpa__NNPDF30NNLO__Wtaunu__Pt70__140__CVetoBVeto.merge.DAOD__HIGG4D4.e4709__s2726__r7725__r7676__p2823
mc15__13TeV.363335.Sherpa__NNPDF30NNLO__Wtaunu__Pt70__140__CFilterBVeto.merge.DAOD__HIGG4D4.e4709__s2726__r7725__r7676__p2823
mc15__13TeV.363336.Sherpa__NNPDF30NNLO__Wtaunu__Pt70__140__BFilter.merge.DAOD__HIGG4D4.e4779__s2726__r7725__r7676__p2823
mc15__13TeV.363337.Sherpa__NNPDF30NNLO__Wtaunu__Pt140__280__CVetoBVeto.merge.DAOD__HIGG4D4.e4709__s2726__r7725__r7676__p2823
mc15__13TeV.363338.Sherpa__NNPDF30NNLO__Wtaunu__Pt140__280__CFilterBVeto.merge.DAOD__HIGG4D4.e4709__s2726__r7725__r7676__p2823
mc15__13TeV.363339.Sherpa__NNPDF30NNLO__Wtaunu__Pt140__280__BFilter.merge.DAOD__HIGG4D4.e4709__s2726__r7725__r7676__p2823
mc15__13TeV.363340.Sherpa__NNPDF30NNLO__Wtaunu__Pt280__500__CVetoBVeto.merge.DAOD__HIGG4D4.e4709__s2726__r7725__r7676__p2823
mc15__13TeV.363341.Sherpa__NNPDF30NNLO__Wtaunu__Pt280__500__CFilterBVeto.merge.DAOD__HIGG4D4.e4779__s2726__r7725__r7676__p2823
mc15__13TeV.363342.Sherpa__NNPDF30NNLO__Wtaunu__Pt280__500__BFilter.merge.DAOD__HIGG4D4.e4779__s2726__r7725__r7676__p2823
mc15__13TeV.363343.Sherpa__NNPDF30NNLO__Wtaunu__Pt500__700__CVetoBVeto.merge.DAOD__HIGG4D4.e4709__s2726__r7725__r7676__p2823
mc15__13TeV.363344.Sherpa__NNPDF30NNLO__Wtaunu__Pt500__700__CFilterBVeto.merge.DAOD__HIGG4D4.e4709__s2726__r7725__r7676__p2823
mc15__13TeV.363345.Sherpa__NNPDF30NNLO__Wtaunu__Pt500__700__BFilter.merge.DAOD__HIGG4D4.e4779__s2726__r7725__r7676__p2823
mc15__13TeV.363346.Sherpa__NNPDF30NNLO__Wtaunu__Pt700__1000__CVetoBVeto.merge.DAOD__HIGG4D4.e4709__s2726__r7725__r7676__p2823
mc15__13TeV.363347.Sherpa__NNPDF30NNLO__Wtaunu__Pt700__1000__CFilterBVeto.merge.DAOD__HIGG4D4.e4709__s2726__r7725__r7676__p2823
mc15__13TeV.363348.Sherpa__NNPDF30NNLO__Wtaunu__Pt700__1000__BFilter.merge.DAOD__HIGG4D4.e4779__s2726__r7725__r7676__p2823
mc15__13TeV.363349.Sherpa__NNPDF30NNLO__Wtaunu__Pt1000__2000__CVetoBVeto.merge.DAOD__HIGG4D4.e4709__s2726__r7725__r7676__p2823
mc15__13TeV.363350.Sherpa__NNPDF30NNLO__Wtaunu__Pt1000__2000__CFilterBVeto.merge.DAOD__HIGG4D4.e4709__s2726__r7725__r7676__p2823
mc15__13TeV.363351.Sherpa__NNPDF30NNLO__Wtaunu__Pt1000__2000__BFilter.merge.DAOD__HIGG4D4.e4779__s2726__r7725__r7676__p2823
mc15__13TeV.363352.Sherpa__NNPDF30NNLO__Wtaunu__Pt2000__E__CMS__CVetoBVeto.merge.DAOD__HIGG4D4.e4709__s2726__r7725__r7676__p2823
mc15__13TeV.363353.Sherpa__NNPDF30NNLO__Wtaunu__Pt2000__E__CMS__CFilterBVeto.merge.DAOD__HIGG4D4.e4709__s2726__r7725__r7676__p2823
mc15__13TeV.363354.Sherpa__NNPDF30NNLO__Wtaunu__Pt2000__E__CMS__BFilter.merge.DAOD__HIGG4D4.e4709__s2726__r7725__r7676__p2823
mc15__13TeV.363436.Sherpa__NNPDF30NNLO__Wmunu__Pt0__70__CVetoBVeto.merge.DAOD__HIGG4D4.e4715__s2726__r7725__r7676__p2823
mc15__13TeV.363437.Sherpa__NNPDF30NNLO__Wmunu__Pt0__70__CFilterBVeto.merge.DAOD__HIGG4D4.e4715__s2726__r7725__r7676__p2823
mc15__13TeV.363438.Sherpa__NNPDF30NNLO__Wmunu__Pt0__70__BFilter.merge.DAOD__HIGG4D4.e4715__s2726__r7725__r7676__p2823
mc15__13TeV.363439.Sherpa__NNPDF30NNLO__Wmunu__Pt70__140__CVetoBVeto.merge.DAOD__HIGG4D4.e4715__s2726__r7725__r7676__p2823
mc15__13TeV.363440.Sherpa__NNPDF30NNLO__Wmunu__Pt70__140__CFilterBVeto.merge.DAOD__HIGG4D4.e4715__s2726__r7725__r7676__p2823
mc15__13TeV.363441.Sherpa__NNPDF30NNLO__Wmunu__Pt70__140__BFilter.merge.DAOD__HIGG4D4.e4771__s2726__r7725__r7676__p2823
mc15__13TeV.363442.Sherpa__NNPDF30NNLO__Wmunu__Pt140__280__CVetoBVeto.merge.DAOD__HIGG4D4.e4715__s2726__r7725__r7676__p2823
mc15__13TeV.363443.Sherpa__NNPDF30NNLO__Wmunu__Pt140__280__CFilterBVeto.merge.DAOD__HIGG4D4.e4715__s2726__r7725__r7676__p2823
mc15__13TeV.363444.Sherpa__NNPDF30NNLO__Wmunu__Pt140__280__BFilter.merge.DAOD__HIGG4D4.e4715__s2726__r7725__r7676__p2823
mc15__13TeV.363445.Sherpa__NNPDF30NNLO__Wmunu__Pt280__500__CVetoBVeto.merge.DAOD__HIGG4D4.e4715__s2726__r7725__r7676__p2823
mc15__13TeV.363446.Sherpa__NNPDF30NNLO__Wmunu__Pt280__500__CFilterBVeto.merge.DAOD__HIGG4D4.e4715__s2726__r7725__r7676__p2823
mc15__13TeV.363447.Sherpa__NNPDF30NNLO__Wmunu__Pt280__500__BFilter.merge.DAOD__HIGG4D4.e4715__s2726__r7725__r7676__p2823
mc15__13TeV.363448.Sherpa__NNPDF30NNLO__Wmunu__Pt500__700__CVetoBVeto.merge.DAOD__HIGG4D4.e4715__s2726__r7725__r7676__p2823
mc15__13TeV.363449.Sherpa__NNPDF30NNLO__Wmunu__Pt500__700__CFilterBVeto.merge.DAOD__HIGG4D4.e4715__s2726__r7725__r7676__p2823
mc15__13TeV.363450.Sherpa__NNPDF30NNLO__Wmunu__Pt500__700__BFilter.merge.DAOD__HIGG4D4.e4715__s2726__r7725__r7676__p2823
mc15__13TeV.363451.Sherpa__NNPDF30NNLO__Wmunu__Pt700__1000__CVetoBVeto.merge.DAOD__HIGG4D4.e4715__s2726__r7725__r7676__p2823
mc15__13TeV.363452.Sherpa__NNPDF30NNLO__Wmunu__Pt700__1000__CFilterBVeto.merge.DAOD__HIGG4D4.e4715__s2726__r7725__r7676__p2823
mc15__13TeV.363453.Sherpa__NNPDF30NNLO__Wmunu__Pt700__1000__BFilter.merge.DAOD__HIGG4D4.e4715__s2726__r7725__r7676__p2823
mc15__13TeV.363454.Sherpa__NNPDF30NNLO__Wmunu__Pt1000__2000__CVetoBVeto.merge.DAOD__HIGG4D4.e4715__s2726__r7725__r7676__p2823
mc15__13TeV.363455.Sherpa__NNPDF30NNLO__Wmunu__Pt1000__2000__CFilterBVeto.merge.DAOD__HIGG4D4.e4715__s2726__r7725__r7676__p2823
mc15__13TeV.363456.Sherpa__NNPDF30NNLO__Wmunu__Pt1000__2000__BFilter.merge.DAOD__HIGG4D4.e4715__s2726__r7725__r7676__p2823
mc15__13TeV.363457.Sherpa__NNPDF30NNLO__Wmunu__Pt2000__E__CMS__CVetoBVeto.merge.DAOD__HIGG4D4.e4715__s2726__r7725__r7676__p2823
mc15__13TeV.363458.Sherpa__NNPDF30NNLO__Wmunu__Pt2000__E__CMS__CFilterBVeto.merge.DAOD__HIGG4D4.e4715__s2726__r7725__r7676__p2823
mc15__13TeV.363459.Sherpa__NNPDF30NNLO__Wmunu__Pt2000__E__CMS__BFilter.merge.DAOD__HIGG4D4.e4715__s2726__r7725__r7676__p2823
mc15__13TeV.363460.Sherpa__NNPDF30NNLO__Wenu__Pt0__70__CVetoBVeto.merge.DAOD__HIGG4D4.e4715__s2726__r7725__r7676__p2823
mc15__13TeV.363461.Sherpa__NNPDF30NNLO__Wenu__Pt0__70__CFilterBVeto.merge.DAOD__HIGG4D4.e4715__s2726__r7725__r7676__p2823
mc15__13TeV.363462.Sherpa__NNPDF30NNLO__Wenu__Pt0__70__BFilter.merge.DAOD__HIGG4D4.e4715__s2726__r7725__r7676__p2823
mc15__13TeV.363463.Sherpa__NNPDF30NNLO__Wenu__Pt70__140__CVetoBVeto.merge.DAOD__HIGG4D4.e4715__s2726__r7725__r7676__p2823
mc15__13TeV.363464.Sherpa__NNPDF30NNLO__Wenu__Pt70__140__CFilterBVeto.merge.DAOD__HIGG4D4.e4715__s2726__r7725__r7676__p2823
mc15__13TeV.363465.Sherpa__NNPDF30NNLO__Wenu__Pt70__140__BFilter.merge.DAOD__HIGG4D4.e4715__s2726__r7725__r7676__p2823
mc15__13TeV.363466.Sherpa__NNPDF30NNLO__Wenu__Pt140__280__CVetoBVeto.merge.DAOD__HIGG4D4.e4715__s2726__r7725__r7676__p2823
mc15__13TeV.363467.Sherpa__NNPDF30NNLO__Wenu__Pt140__280__CFilterBVeto.merge.DAOD__HIGG4D4.e4715__s2726__r7725__r7676__p2823
mc15__13TeV.363468.Sherpa__NNPDF30NNLO__Wenu__Pt140__280__BFilter.merge.DAOD__HIGG4D4.e4715__s2726__r7725__r7676__p2823
mc15__13TeV.363469.Sherpa__NNPDF30NNLO__Wenu__Pt280__500__CVetoBVeto.merge.DAOD__HIGG4D4.e4715__s2726__r7725__r7676__p2823
mc15__13TeV.363470.Sherpa__NNPDF30NNLO__Wenu__Pt280__500__CFilterBVeto.merge.DAOD__HIGG4D4.e4715__s2726__r7725__r7676__p2823
mc15__13TeV.363471.Sherpa__NNPDF30NNLO__Wenu__Pt280__500__BFilter.merge.DAOD__HIGG4D4.e4715__s2726__r7725__r7676__p2823
mc15__13TeV.363472.Sherpa__NNPDF30NNLO__Wenu__Pt500__700__CVetoBVeto.merge.DAOD__HIGG4D4.e4715__s2726__r7725__r7676__p2823
mc15__13TeV.363473.Sherpa__NNPDF30NNLO__Wenu__Pt500__700__CFilterBVeto.merge.DAOD__HIGG4D4.e4715__s2726__r7725__r7676__p2823
mc15__13TeV.363474.Sherpa__NNPDF30NNLO__Wenu__Pt500__700__BFilter.merge.DAOD__HIGG4D4.e4771__s2726__r7725__r7676__p2823
mc15__13TeV.363475.Sherpa__NNPDF30NNLO__Wenu__Pt700__1000__CVetoBVeto.merge.DAOD__HIGG4D4.e4715__s2726__r7725__r7676__p2823
mc15__13TeV.363476.Sherpa__NNPDF30NNLO__Wenu__Pt700__1000__CFilterBVeto.merge.DAOD__HIGG4D4.e4715__s2726__r7725__r7676__p2823
mc15__13TeV.363477.Sherpa__NNPDF30NNLO__Wenu__Pt700__1000__BFilter.merge.DAOD__HIGG4D4.e4715__s2726__r7725__r7676__p2823
mc15__13TeV.363478.Sherpa__NNPDF30NNLO__Wenu__Pt1000__2000__CVetoBVeto.merge.DAOD__HIGG4D4.e4715__s2726__r7725__r7676__p2823
mc15__13TeV.363479.Sherpa__NNPDF30NNLO__Wenu__Pt1000__2000__CFilterBVeto.merge.DAOD__HIGG4D4.e4715__s2726__r7725__r7676__p2823
mc15__13TeV.363480.Sherpa__NNPDF30NNLO__Wenu__Pt1000__2000__BFilter.merge.DAOD__HIGG4D4.e4715__s2726__r7725__r7676__p2823
mc15__13TeV.363481.Sherpa__NNPDF30NNLO__Wenu__Pt2000__E__CMS__CVetoBVeto.merge.DAOD__HIGG4D4.e4715__s2726__r7725__r7676__p2823
mc15__13TeV.363482.Sherpa__NNPDF30NNLO__Wenu__Pt2000__E__CMS__CFilterBVeto.merge.DAOD__HIGG4D4.e4715__s2726__r7772__r7676__p2823
mc15__13TeV.363483.Sherpa__NNPDF30NNLO__Wenu__Pt2000__E__CMS__BFilter.merge.DAOD__HIGG4D4.e4715__s2726__r7725__r7676__p2823
mc15__13TeV.410000.PowhegPythiaEvtGen__P2012__ttbar__hdamp172p5__nonallhad.merge.DAOD__HIGG4D4.e3698__s2608__s2183__r7725__r7676__p2823
mc15__13TeV.410001.PowhegPythiaEvtGen__P2012radHi__ttbar__hdamp345__down__nonallhad.merge.DAOD__HIGG4D4.e3783__s2608__r7725__r7676__p2823
mc15__13TeV.410002.PowhegPythiaEvtGen__P2012radLo__ttbar__hdamp172__up__nonallhad.merge.DAOD__HIGG4D4.e3783__s2608__r7725__r7676__p2823

A Appendix

mc15__13TeV.410003.aMcAtNloHerwigppEvtGen__ttbar__nonallhad.merge.DAOD__HIGG4D4.e4441__s2726__r6869__r6282__p2608
mc15__13TeV.410004.PowhegHerwigppEvtGen__UEEE5__ttbar__hdamp172p5__nonallhad.merge.DAOD__HIGG4D4.e3836__a766__a822__r7676__p2823
mc15__13TeV.410007.PowhegPythiaEvtGen__P2012__ttbar__hdamp172p5__allhad.merge.DAOD__HIGG4D4.e4135__s2608__s2183__r7725__r7676__p2823
mc15__13TeV.410008.aMcAtNloHerwigppEvtGen__ttbar__allhad.merge.DAOD__HIGG4D4.e3964__a766__a818__r7676__p2823
mc15__13TeV.410011.PowhegPythiaEvtGen__P2012__singletop__tchan__lept__top.merge.DAOD__HIGG4D4.e3824__s2608__s2183__r7725__r7676__p2823
mc15__13TeV.410012.PowhegPythiaEvtGen__P2012__singletop__tchan__lept__antitop.merge.DAOD__HIGG4D4.e3824__s2608__s2183__r7725__r7676__p2823
mc15__13TeV.410013.PowhegPythiaEvtGen__P2012__Wt__inclusive__top.merge.DAOD__HIGG4D4.e3753__s2608__s2183__r7725__r7676__p2823
mc15__13TeV.410014.PowhegPythiaEvtGen__P2012__Wt__inclusive__antitop.merge.DAOD__HIGG4D4.e3753__s2608__s2183__r7725__r7676__p2823
mc15__13TeV.410025.PowhegPythiaEvtGen__P2012__SingleTopSchan__noAllHad__top.merge.DAOD__HIGG4D4.e3998__s2608__s2183__r7725__r7676__p2823
mc15__13TeV.410026.PowhegPythiaEvtGen__P2012__SingleTopSchan__noAllHad__antitop.merge.DAOD__HIGG4D4.e3998__s2608__s2183__r7725__r7676__p2823
mc15__13TeV.410500.PowhegPythia8EvtGen__A14__ttbar__hdamp172p5__nonallhad.merge.DAOD__HIGG4D4.e4797__s2726__r7725__r7676__p2823

Bibliography

[1] G. Aad, et al. (ATLAS), *Observation of a new particle in the search for the Standard Model Higgs boson with the ATLAS detector at the LHC*, Phys. Lett. **B716**, 1 (2012), `1207.7214`

[2] G. Aad, et al. (ATLAS, CMS), *Combined Measurement of the Higgs Boson Mass in pp Collisions at $\sqrt{s} = 7$ and 8 TeV with the ATLAS and CMS Experiments*, Phys. Rev. Lett. **114**, 191803 (2015), `1503.07589`

[3] C. Collaboration (CMS), *Measurements of the Higgs boson production and decay rates and constraints on its couplings from a combined ATLAS and CMS analysis of the LHC pp collision data at sqrt s = 7 and 8 TeV* (2015)

[4] S. L. Glashow, *Partial-symmetries of weak interactions*, Nuclear Physics **22(4)**, 579 (1961), URL `http://www.sciencedirect.com/science/article/pii/0029558261904692`

[5] A. Salam, *Weak and Electromagnetic Interactions*, Conf. Proc. **C680519**, 367 (1968)

[6] S. Weinberg, *A Model of Leptons*, Phys. Rev. Lett. **19**, 1264 (1967)

[7] The ATLAS Collaboration (ATLAS), *Summary plots from the ATLAS Standard Model physics group*, `https://atlas.web.cern.ch/Atlas/GROUPS/PHYSICS/CombinedSummaryPlots/SM/` (2017)

[8] C. Patrignani, et al. (Particle Data Group), *Review of Particle Physics*, Chin. Phys. **C40(10)**, 100001 (2016)

[9] P. W. Higgs, *Broken Symmetries and the Masses of Gauge Bosons*, Phys. Rev. Lett. **13**, 508 (1964)

[10] W. Bietenholz, *The Higgs Particle: what is it, and why did it lead to a Nobel Prize in Physics?*, Boletin de la Sociedad Mexicana de Fisica **26**, 3 (2012), `1304.2423`

Bibliography

[11] F. Zwicky, *On the Masses of Nebulae and of Clusters of Nebulae*, The Astrophysical Journal **86**, 217 (1937)

[12] A. H. G. Peter, *Dark Matter: A Brief Review*, ArXiv e-prints (2012), `1201.3942`

[13] V. Faraoni, *Three new roads to the Planck scale* (2017), `1705.09749`

[14] S. P. Martin, *A Supersymmetry primer* (1997), [Adv. Ser. Direct. High Energy Phys.18,1(1998)], `hep-ph/9709356`

[15] R. Haag, J. T. Lopuszanski, M. Sohnius, *All Possible Generators of Supersymmetries of the s Matrix*, Nucl. Phys. **B88**, 257 (1975)

[16] M. Carena, S. Heinemeyer, O. StÃ¥l, C. E. M. Wagner, G. Weiglein, *MSSM Higgs Boson Searches at the LHC: Benchmark Scenarios after the Discovery of a Higgs-like Particle*, Eur. Phys. J. **C73(9)**, 2552 (2013), `1302.7033`

[17] O. Stal, *Prospects for Higgs boson scenarios beyond the Standard ModelProspects for Higgs boson scenarios beyond the standard model*, Int. J. Mod. Phys. Conf. Ser. **31**, 1460289 (2014), `1402.6732`

[18] A. Djouadi, L. Maiani, G. Moreau, A. Polosa, J. Quevillon, V. Riquer, *The post-Higgs MSSM scenario: Habemus MSSM?*, Eur. Phys. J. **C73**, 2650 (2013), `1307.5205`

[19] The ATLAS Collaboration (ATLAS), *Search for Minimal Supersymmetric Standard Model Higgs Bosons H/A in the $\tau\tau$ final state in up to 13.3 fb^{-1} of pp collisions at $\sqrt{s}$= 13 TeV with the ATLAS Detector* (2016)

[20] A. Djouadi, L. Maiani, A. Polosa, J. Quevillon, V. Riquer, *Fully covering the MSSM Higgs sector at the LHC*, JHEP **06**, 168 (2015), `1502.05653`

[21] A. Hoecker, *Physics at the LHC Run-2 and Beyond*, in *2016 European School of High-Energy Physics (ESHEP 2016) Skeikampen, Norway, June 15-28, 2016* (2016), `1611.07864`, URL `https://inspirehep.net/record/1499881/files/arXiv:1611.07864.pdf`

[22] L. Evans, P. Bryant, *LHC Machine*, JINST **3**, S08001 (2008)

[23] The ATLAS Collaboration (ATLAS), *Luminosity Public Results Run 2*, `https://twiki.cern.ch/twiki/bin/view/AtlasPublic/LuminosityPublicResultsRun2` (2017)

[24] G. Aad, et al. (ATLAS), *The ATLAS Experiment at the CERN Large Hadron Collider*, JINST **3**, S08003 (2008)

[25] M. Schott, M. Dunford, *Review of single vector boson production in pp collisions at $\sqrt{s} = 7$ TeV*, Eur. Phys. J. **C74**, 2916 (2014), `1405.1160`

[26] B. Lemmer, *Measurement of Spin Correlations in $t\bar{t}$ Events from pp Collisions at $\sqrt{s}$ = 7 TeV in the Lepton + Jets Final State with the ATLAS Detector*, Ph.D. thesis, Gottingen U., II. Phys. Inst. (2014), `1410.1791`, URL `https://inspirehep.net/record/1320773/files/arXiv:1410.1791.pdf`

[27] A. La Rosa, *The ATLAS Insertable B-Layer: from construction to operation*, JINST **11(12)**, C12036 (2016), `1610.01994`

[28] M. Barczyk, et al., *Online monitoring software framework in the ATLAS experiment*, eConf **C0303241**, THGT003 (2003), `hep-ex/0305096`

[29] M. Aaboud, et al. (ATLAS), *Performance of the ATLAS Trigger System in 2015*, Eur. Phys. J. **C77(5)**, 317 (2017), `1611.09661`

[30] A. R. MartÃnez (ATLAS), *The Run-2 ATLAS Trigger System*, J. Phys. Conf. Ser. **762(1)**, 012003 (2016)

[31] M. Aaboud, et al. (ATLAS), *Search for additional heavy neutral Higgs and gauge bosons in the ditau final state produced in 36 fb^{-1} of pp collisions at $\sqrt{s}$ = 13 TeV with the ATLAS detector* (2017), `1709.07242`

[32] G. Aad, et al. (ATLAS), *Electron and photon energy calibration with the ATLAS detector using LHC Run 1 data*, Eur. Phys. J. **C74(10)**, 3071 (2014), `1407.5063`

[33] G. Aad, et al. (ATLAS), *Muon reconstruction performance of the ATLAS detector in protonâproton collision data at $\sqrt{s}$ =13 TeV*, Eur. Phys. J. **C76(5)**, 292 (2016), `1603.05598`

[34] G. Aad, et al. (ATLAS), *Topological cell clustering in the ATLAS calorimeters and its performance in LHC Run 1* (2016), `1603.02934`

[35] M. Cacciari, G. P. Salam, G. Soyez, *The Anti-k(t) jet clustering algorithm*, JHEP **04**, 063 (2008), `0802.1189`

[36] ATLAS JetEtMiss Group (ATLAS), *JVT Calibration*, `https://twiki.cern.ch/twiki/bin/viewauth/AtlasProtected/JVTCalibration` (2017)

Bibliography

[37] *Tagging and suppression of pileup jets with the ATLAS detector*, Technical Report ATLAS-CONF-2014-018, CERN, Geneva (2014), URL `http://cds.cern.ch/record/1700870`

[38] ATLAS Flavour Tagging Group (ATLAS), *ATLAS Flavour Tagging group recommendation*, `https://twiki.cern.ch/twiki/bin/view/AtlasProtected/BTagCalib2015` (2017)

[39] *Reconstruction, Energy Calibration, and Identification of Hadronically Decaying Tau Leptons in the ATLAS Experiment for Run-2 of the LHC*, Technical Report ATL-PHYS-PUB-2015-045, CERN, Geneva (2015), URL `http://cds.cern.ch/record/2064383`

[40] *Performance of missing transverse momentum reconstruction for the ATLAS detector in the first proton-proton collisions at at $\sqrt{s}= 13$ TeV*, Technical Report ATL-PHYS-PUB-2015-027, CERN, Geneva (2015), URL `http://cds.cern.ch/record/2037904`

[41] G. Aad, et al. (ATLAS), *The ATLAS Simulation Infrastructure*, Eur. Phys. J. **C70**, 823 (2010), `1005.4568`

[42] T. Gleisberg, S. Hoeche, F. Krauss, M. Schonherr, S. Schumann, F. Siegert, J. Winter, *Event generation with SHERPA 1.1*, JHEP **02**, 007 (2009), `0811.4622`

[43] S. Alioli, P. Nason, C. Oleari, E. Re, *NLO Higgs boson production via gluon fusion matched with shower in POWHEG*, JHEP **04**, 002 (2009), `0812.0578`

[44] T. Sjostrand, S. Mrenna, P. Z. Skands, *PYTHIA 6.4 Physics and Manual*, JHEP **05**, 026 (2006), `hep-ph/0603175`

[45] A. Schälicke, T. Gleisberg, S. Hoeche, S. Schumann, J. Winter, F. Krauss, , G. Soff, *Event Generator for Particle Production in High-Energy Collisions*, Prog. Part. Nucl. Phys. **53**, 329 (2004), `hep-ph/0311270`

[46] J. Alwall, R. Frederix, S. Frixione, V. Hirschi, F. Maltoni, O. Mattelaer, H. S. Shao, T. Stelzer, P. Torrielli, M. Zaro, *The automated computation of tree-level and next-to-leading order differential cross sections, and their matching to parton shower simulations*, JHEP **07**, 079 (2014), `1405.0301`

[47] M. Wiesemann, R. Frederix, S. Frixione, V. Hirschi, F. Maltoni, P. Torrielli, *Higgs production in association with bottom quarks*, JHEP **02**, 132 (2015), `1409.5301`

[48] T. Sjöstrand, S. Ask, J. R. Christiansen, R. Corke, N. Desai, P. Ilten, S. Mrenna, S. Prestel, C. O. Rasmussen, P. Z. Skands, *An Introduction to PYTHIA 8.2*, Comput. Phys. Commun. **191**, 159 (2015), `1410.3012`

[49] W. Lukas, *Fast Simulation for ATLAS: Atlfast-II and ISF* (2012), URL `http://cdsweb.cern.ch/record/1458503/files/ATL-SOFT-PROC-2012-065.pdf`

[50] S. Agostinelli, et al. (Geant4), *GEANT4: A Simulation Toolkit*, Nucl. Instrum. Methods A **506**, 250 (2003)

[51] L. Hauswald, L. Zhang, W. Davey, D. Duschinger, L. Fiorini, G. N. Hamity, H. Liu, A. Jelinskas, K. Koeneke, W. Mader, A. McCarn, M. Morinaga, V. E. Muckhoff, B. Murray, N. Rompotis, P. H. Sales De Bruin, T. A. Schwarz, A. Straessner, J. Tanaka, T. Vickey, E. Drechsler, Z. Zinonos, T. G. Zorbas, A. Bailey, L. O. Gerlach, M. Janus, *Search for Neutral MSSM Higgs Bosons H/A and Z′ decaying to $\tau_h\tau_h$ produced in 13 TeV proton-proton collisions with the data collected by the ATLAS Detector in full 2015 and 2016* (**ATL-COM-PHYS-2016-1459**) (2016), URL `https://cds.cern.ch/record/2223255`

[52] T. Dreyer, *Measurement of the Fake Rate for Hadronic Tau Lepton Decays using the ATLAS Experiment* (2016)

[53] ROOT, *TFractionFitter Class Reference* (2017), URL `https://root.cern.ch/doc/master/classTFractionFitter.html`

[54] L. Garren, I. Knowles, T. Sjöstrand, T. Trippe, *Monte carlo particle numbering scheme*, The European Physical Journal C-Particles and Fields **15(1-4)**, 205 (2000)

[55] ROOT, *TH1 Class Reference* (2017), URL `https://root.cern.ch/doc/v606/classTH1.html`

[56] G. Apollinari, O. Brüning, T. Nakamoto, L. Rossi, *High Luminosity Large Hadron Collider HL-LHC*, CERN Yellow Report **(5)**, 1 (2015), `1705.08830`

Erklärung nach §17(9) der Prüfungsordnung für den Bachelor-Studiengang Physik und den Master-Studiengang Physik an der Universität Göttingen:

Hiermit erkläre ich, dass ich diese Abschlussarbeit selbständig verfasst habe, keine anderen als die angegebenen Quellen und Hilfsmittel benutzt habe und alle Stellen, die wörtlich oder sinngemäß aus veröffentlichten Schriften entnommen wurden, als solche kenntlich gemacht habe.

Darüberhinaus erkläre ich, dass diese Abschlussarbeit nicht, auch nicht auszugsweise, im Rahmen einer nichtbestandenen Prüfung an dieser oder einer anderen Hochschule eingereicht wurde.

Göttingen, den 28. Februar 2018

(Lino Gerlach)